SPECTRUM SENSING FOR WIRELESS BROADCAST COMMUNICATION SYSTEMS

by

HOU-SHIN CHEN

A Dissertation submitted to the

Graduate School-New Brunswick

Rutgers, The State University of New Jersey

in partial fulfillment of the requirements

for the degree of

Doctor of Philosophy

Graduate Program in Electrical and Computer Engineering

written under the direction of

Professor David G. Daut

and approved by

____

____

____

____

____

New Brunswick, New Jersey

May, 2008

ABSTRACT OF THE DISSERTATION

Spectrum Sensing for Wireless Broadcast Communication Systems

by Hou-Shin Chen

Dissertation Director: Professor David G. Daut

Spectrum sensing is the methodology used to determine the existence of a specific signal type in very low signal to noise power ratio (SNR) environments. Spectrum sensing is one of the core technologies for the application of Cognitive Radio (CR). An IEEE 802.22 Working Group has developed a Standard to implement CR in the wireless services spectrum. The spectrum, however, has already been allocated to the TV Broadcast Service which delivers ATSC Digital TV (DTV) signals. Cognitive Radio systems are intended to co-exist within the spectrum licensed to TV channels and operate on a non-interfering basis. At present, there are three TV broadcast Standards worldwide, namely the ATSC DTV Standard [1], ETSI DVB-T Standard [2], and the NSPRC DMB-T Standard [3]. The transmitted signals defined by these three Standards possess different characteristics. Thus, in order to apply CR in the DTV bands, different spectrum sensing techniques are needed for these three broadcast Standards. In this thesis, the focus is on the development of suitable spectrum sensing algorithms for the DTV signals defined by these three Standards. In addition, wireless microphone devices use frequency bands that are located within the allocated DTV bands. Cognitive Radio systems should transmit and receive using spectrum that is idle. Hence, in this thesis, spectrum sensing algorithms are also designed to detect the presence of wireless microphone signals. When developing an algorithm to perform spectrum sensing for a specific signal, we make use of particular characteristics embedded in the transmitted signals to design effective detector structures that can discriminate between the presence or absence of licensed information bearing signals. One useful method employed in this thesis is to utilize the cyclostationary property that is present in most of the transmitted data signals to perform spectrum sensing. Additionally, the probability of false alarm and probability of misdetection performance metrics for signal detectors employing different spectrum sensing algorithms are analyzed. The spectrum sensor operating characteristic curves for the different detectors are demonstrated by the use of computer simulations. Simulation results indicate that the spectrum sensing algorithms developed in this thesis can efficiently detect the presence of primary licensed signals when the SNR is as low as -20 dB. Finally, selected spectrum sensing algorithms are implemented using an FPGA-based hardware platform. The hardware implementation of the spectrum sensors verified their performance, as well as demonstrated their practicality due to the low complexity of the algorithms.

Table of Contents

List of Tables

List of Figures

Chapter 1

Introduction

1.1 Background Review

Today, more and more electronic devices are becoming wireless, while the Federal Communications Commission's (FCC) frequency allocation chart is already crowded. However, recent studies show that most of the assigned spectrum is under-utilized. In fact, a fairly recent FCC research report [4] reveals that, in some locations or at some times of day, 70 percent of the allocated spectrum may be sitting idle, even though it is officially spoken for. Therefore, it is possible to utilize the idle spectrum and not affect the primary licensed communication systems. As a consequence, Cognitive Radio [5] was proposed to implement negotiated, or opportunistic, spectrum sharing. Under the charter of an IEEE 802 Standards Committee, a Working Group named IEEE 802.22 was established to develop a standard for a Cognitive Radio-based PHY/MAC/air_interface for use by license-exempt devices on a non-interfering basis in spectrum that has already been allocated to the DTV Broadcast Service. The IEEE 802.22 Working Group is also called the WRAN group since it is essentially developing an air interface for a Wireless Regional Area Network (WRAN) with a range as large as 30 miles. To implement Cognitive Radio without interference within the licensed signal, it is important to be able to detect the existence of licensed signals in very low SNR environments. To this end, the IEEE 802.22 WRAN group established a sensing tiger team to take responsibility for investigating spectrum sensing methodologies. The requirements of the spectrum sensing ability specified by the sensing tiger team is that the misdetection probability (P_{MD}) should not exceed 0.1 subject to a 0.1 probability of false alarm (P_{FA}) when the SNR is -20.8 dB. For spectrum sensing, a power detector, or energy detector, is often used to determine the presence of signals without the use of any prior knowledge of signals. However, for power detectors to work well, the SNR should not be very low [6]. When the SNR is very low, accurate noise power levels and large data sample sizes are needed. But, as is well known, the noise power can be affected by several factors, for example, by temperature and system calibration. Therefore, we are often not able to know the exact noise power level. The lack of knowledge about the noise power is called the noise uncertainty [7]. As shown in [7], noise uncertainty can be as large as ± 1 dB. When the noise uncertainty equals 1 dB, a power detector fails if the SNR is less than -3.3 dB even when a very long sensing time is used. Matched filtering is optimal in a Neyman-Pearson (NP) sense for signal detection in communication systems [8]. However, due to the lack of channel knowledge, its performance is reduced, and its detection performance highly depends on the channel condition. We will discuss the matched filter based detector in Chapter 2. Recently, an eigenvalue based spectrum sensing algorithm was proposed to the tiger team [9]. It makes use of the property that the eigenvalues of the AWGN noise sample covariance matrix are approximately the same when the collected samples are large enough. However, the main disadvantage of the eigenvalue based method is that it cannot distinguish between interference signals and the licensed signals. Therefore, compared to those detectors that determine whether the received signal is purely AWGN noise or not, signature-based spectrum sensing algorithms have an advantage in that, when the signals other than noise are detected, it is almost certain that they are licensed signals. Another possible way to perform spectrum sensing is to utilize a signal's cyclostationary property because of its noise rejection ability. It is known that ideally, the stationary Gaussian process has a zero-valued cyclic spectrum, or spectrum correlation density function (SCD) [17], at a non-zero cyclic frequency. Therefore, we can detect the desired signal by computing its cyclic spectrum provided that the signal is cyclostationary and that its cyclic spectrum is not identically zero at some non-zero cyclic frequency.

1.2 Contributions of this Dissertation

DTV signals use a wide range of wireless spectrum. The spectrum is divided into many non-overlapping bands and each band corresponds to one TV channel. There are hundreds of TV channels and not all of them are used. Hence, it is very likely to find some idle channels within the various DTV bands. Consequently, the DTV spectrum is an appropriate candidate for sharing with CR systems. There are three DTV broadcast standards worldwide. They are ATSC DTV Standard [1], ETSI DVB-T Standard [2], and NSPRC DMB-T Standard [3]. The IEEE 802.22 WRAN Standard is applicable to CR that will be used in North American area wherein ATSC DTV signals are broadcast. It can be expected that standards which are defined to apply CR in those areas which adopt DVB-T and DMB-T standards will be developed soon. Thus, in this study, spectrum sensing algorithms are developed for the DTV signals defined by these three Standards. The major contributions of this dissertation span several major areas. First, the development of spectrum sensing algorithms for the three DTV broadcast Standards will enable CR to operate in the licensed DTV bands. In addition to spectrum sensing algorithms for DTV signals, the development of spectrum sensing algorithms for wireless microphone signals is undertaken so as to prevent interference to the wireless microphone devices when CR systems are operating nearby. Second, analytical aspects of this study include the development and evaluation of performance metrics, to the extent possible, for various spectrum sensing algorithms. In particular, the false alarm probability and misdetection probability are evaluated for selected algorithms. The third major area of contribution is the development, and execution, of computer simulations to obtain overall performance evaluation of various spectrum sensing algorithms. The simulation results provide a useful means of comparison between the various algorithms. The fourth major area of contribution is the hardware verification of selected algorithms that have significant practical value. Through FPGA implementation of selected spectrum sensing algorithms, and the use of real-world test data, evaluation of the performances of the developed algorithms are obtained. Furthermore, the practical utility of the spectral sensing algorithms is demonstrated.

Chapter 2

Spectrum Sensing for ATSC DTV Systems

Spectrum sensing for the presence of ATSC DTV signals in VHF/UHF TV bands under very low SNR environments is one of the core technologies in IEEE 802.22 WRAN. In order to implement CR without interference to the licensed signal, the sensing tiger team of the IEEE 802.22 Working Group specified the requirements of the spectrum sensing of ATSC DTV signals. In particular, the probability of misdetection should not exceed 0.1 subject to a 0.1 of probability of false alarm when the SNR is -20.8 dB. There are multiple signatures embedded in the ATSC DTV signals and these signatures can be utilized to perform spectrum sensing. Compared with the power detector [6] [7] and eigenvalue-based sensing algorithms [9]. Signature-based spectrum sensing algorithms have an advantage in that when the signals other than noise are detected, we are almost sure that they are signals we want to detect. Thus, in this chapter, several signature based spectrum sensing algorithms are presented. Furthermore, we make use of the noise rejection property of the cyclostationarity which exists in most transmitted data signals to perform spectrum sensing. The sensing algorithms are based on measurement of the cyclic spectrum of the received signals. The statistics of the cyclic spectrum of the stationary white Gaussian process are fully analyzed for three measurement methods of the cyclic spectrum mentioned in this chapter. The false alarm probability for detectors employing different algorithms is also analytically derived. The operating characteristic curves for different spectrum sensors are determined from computer simulations using an ATSC A/74 DTV signal captures database as a testbed. The spectrum sensing algorithms described in this chapter have also been made available in the literature [10] [11].

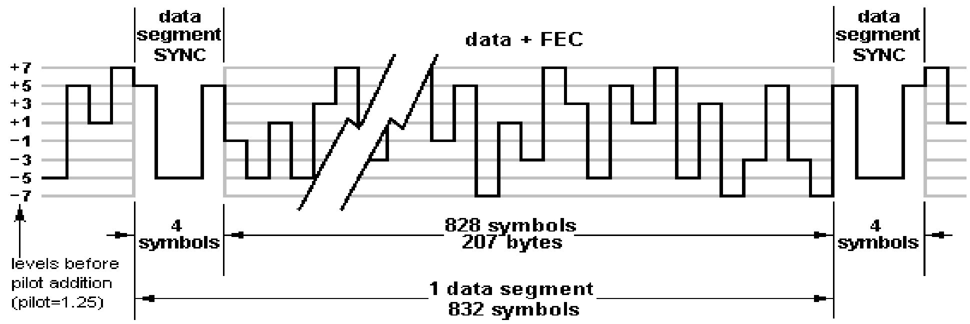

Figure 2.1: ATSC DTV data signal segment.

2.1 Signature Based Spectrum Sensing Algorithms

First, we shall briefly describe the structure of ATSC DTV signals [1]. DTV data are modulated using 8-Vestigial Sideband (8-VSB). In addition to the eight-level digital data stream, a two-level (binary) four-symbol data segment sync (Segment Sync) is inserted at the beginning of each data segment. A complete segment consists of 832 symbols: four symbols for the data segment sync and 828 data symbols. The data segment sync pattern is a 1001 pattern, as described in Fig. 2.1. Multiple data segments (313 segments) comprise a data field. The first data segment in a data field is called the data field sync segment (Field Sync). The structure of the data field sync segment is shown in Fig. 2.2.

2.1.1 Signature Based Spectrum Sensing Simulation Model

Since we desire to utilize signatures embedded in the data transmission to perform spectrum sensing, we have to compute the baseband complex envelope of the received signal $\hat{r}[n]$. Figure 2.3 illustrates the spectrum sensing simulation model of the signature-based

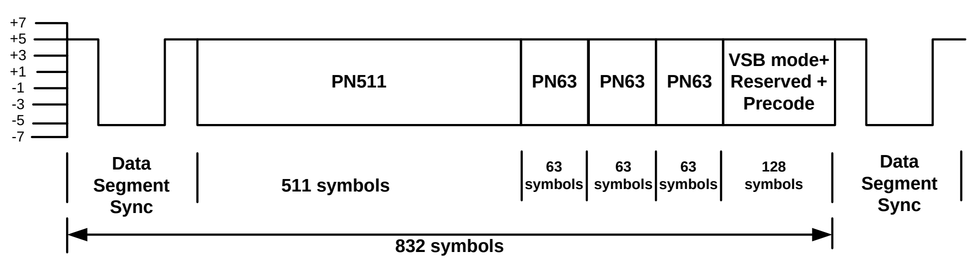

Figure 2.2: ATSC DTV signal field sync segment.

sensing algorithms. This model describes a procedure which computes the baseband signal (complex envelope). The real-valued DTV signal capture data $r[n]$ are obtained by sampling DTV channels at a rate of $f_s = 21.524476$ MHz and then down converted to a low central frequency $f_{IF} = 5.38$ MHz [13] [14]. The carrier frequency parameter f_c in Fig. 2.3 is 2.69 MHz. Then, $\hat{r}[n]$ is scaled in amplitude to produce $x[n]$ which has the desired signal power

$$x[n] = \frac{\hat{r}[n]}{\alpha} \tag{2.1}$$

where α is the power scaling factor, and

$$\alpha = 10^{(P_{Desired} - P_S)/20}. \tag{2.2}$$

The parameters $P_{Desired}$ and P_S are the desired signal power and the signal power of $\hat{r}[n]$ in units of dBm, respectively. Finally, we add a *filtered* complex additive white Gaussian noise (AWGN) $w[n]$ to $x[n]$ to form the needed experimental data $y[n]$, hence

$$y[n] = x[n] + w[n]. \tag{2.3}$$

We will further assume that $w[n]$ is zero-mean and the noise power spectral density (PSD) is $N_0 = -174 + 11 = -163$ dBm/Hz where -174 is thermal noise power spectral density under normal temperature conditions and 11 is noise figure of the receiver [15]. Therefore, the noise power is $N_0 B$ = -163dBm/Hz·6MHz = -95.2185 dBm. Filtering of the noise is accomplished by the lowpass filter employed in Fig. 2.3.

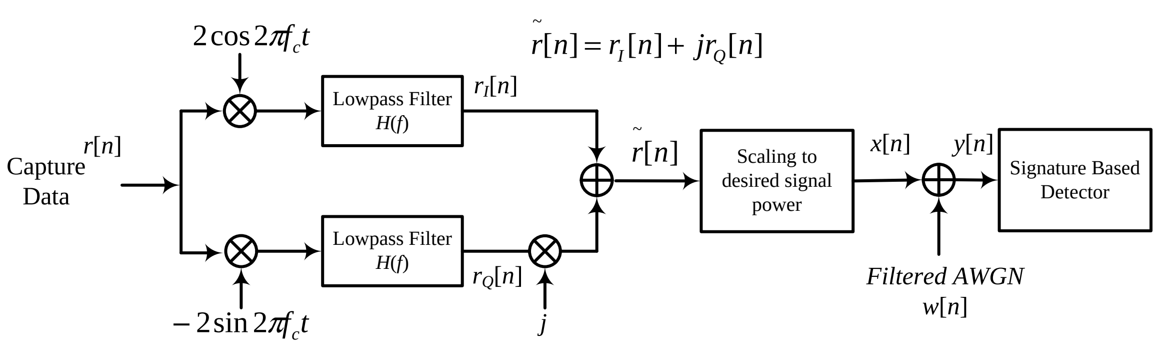

Figure 2.3: Spectrum sensing simulation model of the Signature Based Detector.

2.1.2 Field Sync Based Algorithms

Field Sync Correlation Detector (FSCD)

As mentioned before, a Field Sync occurs regularly every 24.2 ms. Hence, it is intuitive to implement a correlation detector (matched filter) to perform spectrum sensing using the Field Sync. Let $q[n]$ denote the 832 symbols in Fig. 2.2. Because the second PN63 sequence is inverted every other field and the last 128 symbols are unknown, we will simply zero-out these two parts of $q[n]$. Furthermore, the capture data $r[n]$ has a double symbol rate as does $y[n]$. Thus, $q[n]$ is 2X upsampled to form the sequence $p[n]$ which has a double symbol rate. Define the test statistic T_{fscd} as

$$T_{fscd} = \max_{0 \le i \le W_{fscd}-1} \left| \sum_{n=0}^{L-1} p[n] y^*[i+n] \right| \tag{2.4}$$

where $L = 1664$ is the length of $p[n]$ and $W_{fscd} = 520892$ is the number of samples of $y[n]$ that appear in 24.2 ms.

VSB Modulated Pilot Sequence

In the previous section, we use a binary pilot sequence $p[n]$ and correlate it with the received signal. However, the received pilot sequence is, of course, not binary. Thus, we should use a sequence that, to the best of our knowledge, matches the received pilot sequence. According to [1], the transmitted signal is a Vestigial Sideband (VSB) modulated signal. Therefore, instead of simply 2X upsampling $q[n]$ to form the pilot sequence $p[n]$, we shall add a lowpass interpolation filter and a VSB modulator so that the sequence $s[n]$ shown in Fig. 2.4 best matches the transmitted Field Sync sequence. It has been shown through simulations, that with this modification, the detection performance can be improved by 2 to 3 dB in terms of SNR for most of the DTV capture data cases considered.

Probability of False Alarm for FSCD

We now provide an explicit calculation of the false alarm rate. For hypothesis H_0, which corresponds to the presence of noise only, i.e., $y[n] = w[n]$, denote

$$T_i = \sum_{n=0}^{L-1} p[n]w^*[i+n] \tag{2.5}$$

which is the result of the complex correlations before taking the absolute value in (2.4). For convenience, we normalize $p[n]$ such that

$$\sum_{n=0}^{L-1} |p[n]|^2 = 1. \tag{2.6}$$

Because the linear combination of joint Gaussian random variables is still Gaussian distributed, T_i is a complex Gaussian random variable. Therefore, the quantity $|T_i|$ is Rayleigh distributed according to

$$f_{|T_i|}(t : H_0) = \begin{cases} \frac{2t}{\sigma^2} e^{-\frac{t^2}{\sigma^2}}, & t \geq 0 \\ 0, & t < 0 \end{cases} \tag{2.7}$$

where σ^2 is noise variance and $\sigma^2 = N_0 B f_s$. According to (2.4), the test statistic T_{fscd} is the maximum of $|T_i|$ over a sample-size window of W_{fscd}. Because the random variables $\{T_i\}_{i=0}^{W_{fscd}-1}$ are identical but not necessarily independently distributed, it is difficult to find the exact probability distribution of T_{fscd}. However, assuming that the random variables $\{T_i\}_{i=0}^{W_{fscd}-1}$ are independent gives a good approximation of the probability distribution of T_{fscd}. By making the assumption that the $\{T_i\}_{i=0}^{W_{fscd}-1}$ are independent, from [16], we find that the cumulative probability distribution of T_{fscd} is

$$F_{T_{fscd}}(t : H_0) = \left(\int_0^t \frac{2u}{\sigma^2} e^{-\frac{u^2}{\sigma^2}} du \right)^{W_{fscd}}. \tag{2.8}$$

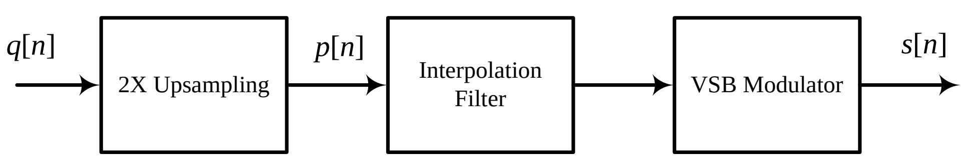

Figure 2.4: Procedure for generating a VSB modulated sequence in the context of a 2X symbol rate.

Then, for a particular value for the probability of false alarm (P_{FA}), the corresponding threshold γ_{fscd} can be found by

$$P_{FA} = 1 - F_{T_{fscd}}(\gamma_{fscd} : H_0). \tag{2.9}$$

Finally, after some straightforward calculation, we have

$$\gamma_{fscd} = \mu_{fscd} \left(\sigma^2 \ln \frac{1}{1 - (1 - P_{FA})^{1/W_{fscd}}} \right)^{1/2} \tag{2.10}$$

where μ_{fscd} is an heuristic adjusting factor added artificially to account for the approximation mentioned above. Note that when a VSB modulated sequence ($s[n]$) is used, the calculation of the probability of false alarm is the same as that when a binary sequence ($p[n]$) is used. Thus, we still use (2.10) to compute the threshold when a VSB modulated sequence is used. However, the value of μ_{fscd} needs to be re-adjusted. According to simulation results, when the binary sequence $p[n]$ is used, $\mu_{fscd} = 1$ gives a very accurate value for the desired probability of false alarm which means that the T_i are very close to being independent in this situation.

2.1.3 Segment Sync Based Algorithms

Segment Sync Autocorrelation Detector (SSAD)

In Section 2.1.2, we made use of the Field Sync to perform spectrum sensing. There are two disadvantages to using the Field Sync. One is that the results of the correlation between received signals and the pilot sequence are severely affected by frequency offset and multipath fading channel impairments. The other is that the pilot sequence is very sparse in the transmission of the ATSC DTV signal. There is only one Field Sync every 24.2 ms, so that we have to observe a received signal up to $W_{fscd} = 520892$ samples and perform a correlation 520892 times. Thus, the complexity is high for the Field Sync correlation detector. As a result, instead of using the Field Sync, we can utilize the data segment sync as shown in Fig. 2.1 to perform spectrum sensing. There is a data segment sync consisting of 4 symbols at the beginning of every ATSC DTV signal data segment. Because the time difference between two consecutive Segment Sync components is only 0.077 ms (832 symbols) which is very short, it is reasonable to assume that they encounter the same channel effects including timing offset, frequency offset, and multipath fading. Consequently, we use the autocorrelation of the two consecutive Segment Sync elements as our basic approach to perform spectrum sensing. Furthermore, using data segment sync to perform spectrum sensing has the advantage that we only need to observe a window of $W_{ssad} = 1664$ samples which is much smaller the correlation times when compared to that used by the Field Sync method. Figure 2.5 shows the block diagram of the Segment Sync Autocorrelation Detector. Define the test statistic T_{ssad} as

$$T_{ssad} = \max_{0 \le m \le W_{ssad}-1} |T_m| \tag{2.11}$$

where

$$T_m = \frac{1}{N_D} \sum_{n=0}^{N_D-1} \frac{1}{8} \sum_{k=0}^{7} y[m+k+nL] y^*[m+k+(n+1)L]. \tag{2.12}$$

The parameter N_D is the number of collected Segment Sync elements used to perform autocorrelation. The Segment Sync has 4 symbols but an 8 sample autocorrelation is performed because the sequence $y[n]$ is at double the symbol rate.

Probability of False Alarm of SSAD

For hypothesis H_0, the decision statistic of the SSAD method is given by

$$T_m = \frac{1}{N_D} \sum_{n=0}^{N_D-1} \frac{1}{8} \sum_{k=0}^{7} w[m+k+nL] w^*[m+k+(n+1)L]. \tag{2.13}$$

According to the Central Limit Theorem, when N_D is large, T_m will approach a circularly symmetric complex Gaussian distribution, that is

$$\lim_{N_D \to \infty} T_m \to CN(0, \frac{\sigma^4}{8N_D}). \tag{2.14}$$

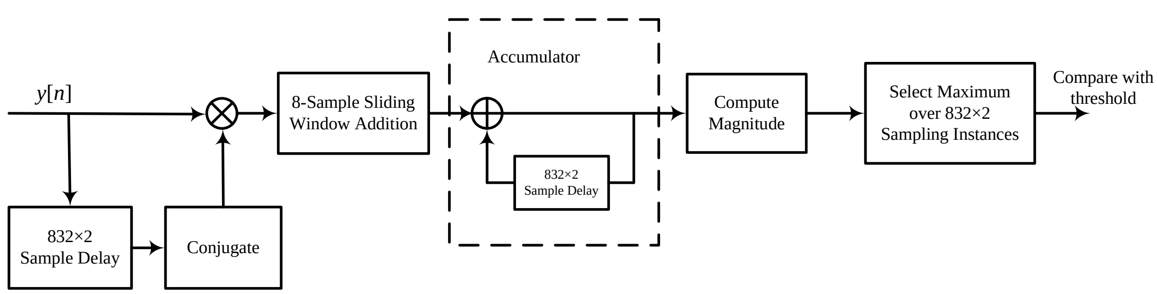

Figure 2.5: Segment-Sync Autocorrelation Detector.

Because $\{T_m\}_{m=0}^{W_{ssad}-1}$ are identical but not independently distributed, it is difficult to determine the probability distribution of T_{ssad}. We will follow the same philosophy that was used in calculating the probability of false alarm for the FSCD. We suppose that $\{T_m\}_{m=0}^{W_{ssad}-1}$ are independent in order to obtain a reference threshold for a corresponding probability of false alarm. Following the same procedure as (2.8)(2.9)(2.10), we have

$$\gamma_{ssad} = \mu_{ssad} \left(\frac{\sigma^4}{8N_D} \ln \frac{1}{1-(1-P_{FA})^{1/W_{ssad}}} \right)^{1/2}. \tag{2.15}$$

Maximum Combining Segment Sync Autocorrelation Detector (MCSSAD)

When we accumulate a large number of data segment sync elements, i.e., when the sensing time is long, timing drift effects will restrict the improvement of the performance that comes from a longer sensing time. In order to alleviate the timing drift effect, we can slice the total sensing time into several time slots and then apply a SSAD detector to each time slot. Then, finally, we use the average of the maximum absolute value of autocorrelation of each time slot as our detection statistic. We call this detector the Maximum Combining Segment Sync Autocorrelation Detector (MCSSAD). The threshold is still determined by (2.15) by adjusting the value of μ_{ssad}.

2.2 Cyclostationarity Based Spectrum Sensing Algorithms

2.2.1 Review of Cyclostationary Properties

In this section, we present a brief summary of some useful equations relevant to cyclostationarity. Details of cyclostationary properties can be found in [17] [19]. The cyclic auto-correlation function of a stochastic process $x(t)$ for a given cyclic frequency α can be defined as follows

$$R_x^\alpha(\tau) = \lim_{\Delta t \to \infty} \frac{1}{\Delta t} \int_{-\Delta t/2}^{\Delta t/2} x(t+\tau/2)x^*(t-\tau/2)e^{-j2\pi\alpha t} dt \tag{2.16}$$

or

$$R_x^\alpha(\tau) = \lim_{\Delta t \to \infty} \frac{1}{\Delta t} \int_{-\Delta t/2}^{\Delta t/2} u(t+\tau/2)v^*(t-\tau/2) dt \tag{2.17}$$

where $u(t) = x(t)e^{-j\pi\alpha t}$ and $v(t) = x(t)e^{+j\pi\alpha t}$ are frequency shifted versions of $x(t)$ so that $R_x^\alpha(\tau)$ can be understood as the cross-correlation of $u(t)$ and $v(t)$. The cyclic spectrum of $x(t)$ for a given cyclic frequency α is defined as

$$S_x^\alpha(f) = \int_{-\infty}^{\infty} R_x^\alpha(\tau)e^{-j2\pi\alpha\tau}d\tau = S_{uv}(f) \tag{2.18}$$

where the second equality comes from (2.17). Thus, the cyclic spectrum $S_x^\alpha(f)$ can also be understood as the cross-spectral density of frequency shifted signals $u(t)$ and $v(t)$. In light of this interpretation, the cyclic spectrum is also called a Spectral Correlation Density (SCD) function. In this thesis, we will use the terms cyclic spectrum and SCD interchangeably.

2.2.2 Measurement of Spectral Correlation

It can be shown that the cyclic spectrum is obtainable from the following limit operations applied to *temporally* smoothed products of spectral components described by the expression

$$\begin{aligned} S_x^\alpha(f) &= \lim_{\Delta f \to 0} \lim_{\Delta t \to \infty} \frac{1}{\Delta t} \int_{-\Delta t/2}^{\Delta t/2} \Delta f X_{1/\Delta f}(t, f + \alpha/2) \\ &\quad \cdot X_{1/\Delta f}^*(t, f - \alpha/2) dt \end{aligned} \tag{2.19}$$

where $X_{1/\Delta f}(t, \nu)$ is the short-term Fourier transform of $x(t)$ with center frequency ν and approximate bandwidth Δf

$$X_{1/\Delta f}(t, \nu) \triangleq \int_{t-1/2\Delta f}^{t+1/2\Delta f} x(\lambda)e^{-j2\pi\nu\lambda}d\lambda. \tag{2.20}$$

It also can be shown that $S_x^\alpha(f)$ is given by the limit of *spectrally* smoothed products of spectral components

$$\begin{aligned} S_x^\alpha(f) &= \lim_{\Delta f \to 0} \lim_{\Delta t \to \infty} \frac{1}{\Delta f} \int_{f-\Delta f/2}^{f+\Delta f/2} \frac{1}{\Delta t} X_{\Delta t}(t, \nu + \alpha/2) \\ &\quad \cdot X_{\Delta t}^*(t, \nu - \alpha/2) d\nu \end{aligned} \tag{2.21}$$

where $X_{\Delta t}(t, f)$ is defined by (2.20) with $1/\Delta f$ being replaced by Δt. Equations (2.19) and (2.21) are described in [18]. In this thesis, we present a third method which is also based on *spectrally* smoothed products of spectral components. Let $x(t, \mu)$ denote the frequency down-converted signal which has carrier frequency μ. Then, the cyclic spectrum is given by

$$\begin{aligned} S_x^\alpha(f) \quad &= \quad \lim_{\Delta f \to 0} \lim_{\Delta t \to \infty} \frac{1}{\Delta f} \int_{f-\Delta f/2}^{f+\Delta f/2} \frac{1}{\Delta t} X_{\Delta t}(t, \mu, f+\alpha/2) \\ &\quad \cdot X_{\Delta t}^*(t, \mu, f-\alpha/2) d\mu \end{aligned} \tag{2.22}$$

where

$$X_{\Delta t}(t, \mu, \nu) \triangleq \int_{t-\Delta t/2}^{t+\Delta t/2} x(\lambda, \mu) e^{-j2\pi\nu\lambda} d\lambda. \tag{2.23}$$

Note that (2.21) and (2.22) represent basically the same approach for the measurement of spectral correlation. The cyclic spectrum is obtained by *spectrally* smoothed products of spectral components. The difference will be easily seen in their digital implementations.

2.2.3 Digital Implementation

The digital implementation of (2.19), (2.21) and (2.22) is based on use of the fast Fourier transform (FFT) algorithm for computation of a discrete-time/discrete-frequency counterpart of the sliding-window complex Fourier transform of (2.20) and (2.23). Note that in digital implementation, the frequency variable f and cyclic frequency variable α should be a multiple of F_s. The parameter $F_s = 1/NT_s$ is the frequency sampling increment and T_s is the time-sampling increment. Let $f = lF_s$ and $\alpha = 2DF_s$, the discrete-frequency smoothing method of (2.21) is given by

$$\begin{aligned} S_x^\alpha[l] \quad &= \quad \frac{1}{(N-1)T_s} \frac{1}{M} \sum_{\nu=-(M-1)/2}^{(M-1)/2} X[l+D+\nu] \\ &\quad \cdot X^*[l-D+\nu] \end{aligned} \tag{2.24}$$

where

$$X[\nu] = \sum_{k=0}^{N-1} x[k] e^{-j2\pi\nu k/N} \tag{2.25}$$

which is the DFT of the sampled signal $x[k] = x(kT_s)$, and M is the smoothing factor. The parameter N is the number of time samples used in DFT. The frequency smoothing method of (2.22) is given by

$$\begin{aligned} S_x^{\alpha}[l] &= \frac{1}{(N-1)T_s}\frac{1}{M}\sum_{\mu=-(M-1)/2}^{(M-1)/2} X[l+D,\mu] \\ &\cdot X^*[l-D,\mu] \end{aligned} \tag{2.26}$$

where

$$X[\nu,\mu] = \sum_{k=0}^{N-1} x[k,\mu]e^{-j2\pi\nu k/N} \tag{2.27}$$

and $x[k,\mu] = x(kT_s, f_{IF} + \mu \cdot \delta f)$ is frequency down-converted signal having carrier frequency $f_{IF} + \mu \cdot \delta f$. The parameter f_{IF} is an intermediate frequency. Unless otherwise noted, here $x(t)$ is the frequency down-converted signal which has central frequency f_{IF}. Now, we can see the difference between (2.21) and (2.22) in their digital implementations. For (2.21), spectral smoothing is performed over nearby subcarriers of the DFT output given by (2.15), and therefore, it is called a discrete-frequency smoothing method. As for (2.22), spectral smoothing is performed over the same subcarrier of the DFT output of down-converted signals which have slightly different carrier frequencies given by (2.27). Therefore, by controlling the parameter δf, we can obtain more precise frequency resolution without increasing the DFT size. The discrete-time average method is given by

$$S_x^{\alpha}[l] = \frac{1}{(N-1)T_s}\frac{1}{KM}\sum_{u=0}^{KM-1} X_u[l+D] \cdot X_u^*[l-D] \tag{2.28}$$

where

$$X_u[\nu] = \sum_{k=0}^{N-1} x_u[k]e^{-j2\pi\nu k/N} \tag{2.29}$$

which is the DFT of the sliding sampled signal $x_u[k] = x(\frac{u(N-1)T_s}{K} + kT_s)$. The parameter K is the block overlapping factor. When K is 1, all data segments are non-overlapping. For more detail about the measurement of a cyclic spectrum, the reader is referred to [18].

2.2.4 Statistical Analysis of the Measured AWGN SCD

Probability Distribution Function of the Computed AWGN SCD Using Equation (2.24)

Upon substituting $x(t)$ with $w(t)$ which is a white Gaussian process, we obtain the SCD of an additive white Gaussian noise (AWGN). The corresponding short-term Fourier transform of AWGN is denoted as $W[\nu]$, $W[\nu, \mu]$ and $W_u[\nu]$ in (2.25), (2.27) and (2.29). We know that $w[k]$ are independently and identically distributed (i.i.d.) Gaussian random variables with zero-mean and variance σ^2. It can be easily shown that $W[\nu]$, $\nu = 0, 1, \ldots, N-1$ are circularly symmetric i.i.d. complex Gaussian random variables with zero-mean and variance $N\sigma^2$. In (2.24), the random variable $W[l + D + \nu]W^*[l - D + \nu]$ has zero-mean, while its real and imaginary parts are uncorrelated and have the same variance $N^2\sigma^4/2$. Then, by the Central Limit Theorem, for sufficiently large M

$$\lim_{M\to\infty} S_w^\alpha[l] \to CN(0, \frac{N^2}{(N-1)^2 T_s^2}\frac{\sigma^4}{M}) \tag{2.30}$$

where $CN(\mu, \sigma^2)$ represents the circularly symmetric complex Gaussian distribution with mean μ and variance σ^2. We can easily determine that the random vectors $\mathbf{S}_w^\alpha = [S_w^\alpha[0], \ldots S_w^\alpha[N-1]]$ are jointly circular symmetric complex Gaussian with zero-mean and possess the covariance matrix

$$Cov(\mathbf{S}_w^\alpha) = E[\mathbf{S}_w^\alpha \mathbf{S}_w^{\alpha\,H}] = \mathbf{T}^S \tag{2.31}$$

where $\mathbf{T}^S$ is a Toeplitz matrix having the entries

$$T_{mn}^S = \begin{cases} \frac{M-|m-n|}{M^2}\frac{N^2\sigma^4}{(N-1)^2T_s^2} & |m-n| < M \\ 0 & |m-n| \geq M. \end{cases} \tag{2.32}$$

Probability Distribution Function of the Computed AWGN SCD Using Equation (2.26)

In (2.26), the random variables $X[l, \mu]$ for different μ are not necessarily independent. However, they are almost independent for sufficiently large difference in frequency index

μ or subcarrier index l. Therefore, we assume, for ease of analysis, that they are independent. The resulting distribution yields a good approximation. As a result, it can be easily shown that the distribution of $S_w^\alpha[l]$ is given by (2.30) for sufficiently large M. Furthermore, by appropriately choosing δf, random variables, $S_w^\alpha[l]$'s, are nearly independent.

Probability Distribution Function of the Computed AWGN SCD Using Equation (2.28)

First, we should note that, for the random variables corresponding to the same frequency subcarrier, $W_u[\nu]$ and $W_r[\nu]$ are not independent for $|u-r|<K$ because they are Fourier transformed by overlapping samples of a white Gaussian process. However, for the random variables taken from different frequency of $W_u[\nu]$ and $W_r[\omega]$ are always independent. Let $Z_u^D[l] = W_u[l+D]W_u^*[l-D]$, note again that the complex random variable $Z_u^D[l]$ has zero-mean, variance $N\sigma^2$, and most important of all, its real part and imaginary part are uncorrelated. Define the random vector $\mathbf{Z}^D[l] = [Z_0^D[l], Z_1^D[l], \ldots, Z_{KM-1}^D[l]]$, then $\mathbf{Z}^D[l]$ is zero-mean with covariance matrix

$$Cov(\mathbf{Z}^D[l]) = E[\mathbf{Z}^D[l]\mathbf{Z}^D[l]^H] = \mathbf{T}^Z \tag{2.33}$$

where $\mathbf{T}^Z$ is a Toeplitz matrix having the entries

$$T_{mn}^Z = \begin{cases} (1-\frac{|m-n|}{K})^2 N^2\sigma^4 e(m,n) & |m-n|<K \\ 0 & |m-n|\geq K \end{cases} \tag{2.34}$$

with $e(m,n) = e^{-j4\pi D(m-n)/K}$. We can write (2.28) as

$$S_w^\alpha[l] = \frac{1}{(N-1)T_s}\frac{1}{KM}\sum_{u=0}^{KM-1} Z_u^D[l] \tag{2.35}$$

and the variance of $S_w^\alpha[l]$ is

$$\begin{aligned} Var(S_w^\alpha[l]) &= \frac{1}{(N-1)^2T_s^2}\frac{1}{(KM)^2}\sum_m\sum_n T_{mn}^Z \\ &= \frac{1}{(KM)^2}\frac{N^2\sigma^4}{(N-1)^2T_s^2} \\ &\cdot(KM + \sum_{i=1}^{K-1}(KM-i)(1-\frac{i}{K})\cdot 2cos(4i\pi D/K)) \end{aligned} \tag{2.36}$$

Then, by the Central Limit Theorem, for the case of dependent random variables, we have that

$$\lim_{KM\to\infty} \frac{S_w^\alpha[l]}{\sqrt{VAR(S_w^\alpha[l])}} \to CN(0,1). \tag{2.37}$$

Fortunately, the random variables associated with different carriers of $S_w^\alpha[l]$ are independent. Hence, the random vector $\mathbf{S}_w^\alpha = [S_w^\alpha[0], \ldots S_w^\alpha[N-1]]$ obtained by using the discrete-time average method consists of i.i.d. circularly symmetric complex Gaussian random variables having zero-mean and variance given by (2.36).

2.2.5 Discussion

1. Computing the SCD using the discrete-frequency smoothing method, (2.24), usually needs a large FFT size which increases overall complexity. We can see from (2.32) that the random variables of the measured SCD corresponding to AWGN noise are dependent. This is an unwanted property and contradictory to the true SCD of AWGN. The inherent dependence of the SCD is also an undesired property in the detection of a signal. For example, we may use the maximum of the moving average amplitude of the measured SCD as our decision statistic. The dependence of the random variables of SCD means that large values of the moving average could occur with high probability for AWGN noise. On the other hand, the random variables of the measured SCD of AWGN noise obtained by using the other two methods are independent or nearly independent.

2. The variance of the measured SCD corresponding to AWGN using discrete-time average method, (2.28), is given by (2.36). We can see that if the ratio of D/K is $1/2$ or integers, then the *cosine* term becomes 1. As a consequence, the variance of the SCD is approximately the same as the variance of the power spectrum density which means the SCD of AWGN is not approaching zero. This is the cycle leakage effect described in [18] and is revealed here in (2.36). Therefore, we have to increase the block-overlap parameter K to avoid the undesired cycle leakage effect. However, increasing K results in larger complexity.

3. The computed SCD corresponding to AWGN using (2.26) possesses the best property that the random variables of different frequency subcarriers are almost independent, and there is no cycle leakage effect. However, when using (2.26) to compute SCD, the down conversion operation must be applied many times which results in a large complexity.

In the application of signal detection or spectrum sensing in the presence of AWGN noise, based on the discussion above, we find that the SCD corresponding to AWGN measured by the three different methods has some drawbacks. The features of cyclic spectrum of the transmitted signal are also different among each of these three methods. Therefore, we should choose one of the three methods that offers the best tradeoff between desired features and unwanted properties.

2.2.6 Cyclostationary Signal Model

Let $x(t)$ be the transmitted continuous time signal, that encounters a linear time-invariant channel denoted by $h(t)$. Then, the channel output is corrupted by an AWGN noise $w(t)$. The received signal $y(t)$ is therefore given by

$$y(t) = x(t) \otimes h(t) + w(t) \tag{2.38}$$

where $w(t)$ is a a white Gaussian process with zero-mean and its cyclic auto-correlation function is given as

$$R_w^\alpha(\tau) = \begin{cases} \sigma^2\delta(\tau), & \alpha = 0 \\ 0, & \alpha \neq 0. \end{cases} \tag{2.39}$$

In [17], stationary signals are divided into two categories. Those stationary signals with $R_x^\alpha(\tau) \neq 0$ for some $\alpha \neq 0$ are called *cyclostationary* and those stationary signals with $R_x^\alpha(\tau) = 0$ for all $\alpha \neq 0$ are referred to as *purely stationary*. Thus, AWGN is a purely stationary signal. It is shown in [17] that when a signal $x(t)$ undergoes an LTI transformation ($z(t) = x(t) \otimes h(t)$), the input SCD and output SCD are related according to

$$S_z^\alpha(f) = H(f + \alpha/2)H^*(f - \alpha/2)S_x^\alpha(f). \tag{2.40}$$

Here the function $H(f)$ is the frequency response of the channel impulse response. This relationship can be easily understood by considering the SCD as being the cross-spectrum of the spectral components of $x(t)$ at frequencies $f \pm \alpha/2$ and these two spectral components are scaled by $H(f \pm \alpha/2)$ after passing through an LTI channel. Finally, since in (2.38) $z(t) = x(t) \otimes h(t)$ and $w(t)$ are independent, the cyclic spectrum of the received signal $y(t)$ is

$$\begin{aligned} S_y^\alpha(f) &= S_z^\alpha(f) + S_w^\alpha(f) \\ &= \begin{cases} S_z(f) + S_w(f) & \alpha = 0 \\ S_z^\alpha(f) & \alpha \neq 0 \end{cases} \end{aligned} \tag{2.41}$$

and therefore, we have

$$S_y^\alpha(f) = H(f + \alpha/2)H^*(f - \alpha/2)S_x^\alpha(f), \quad \alpha \neq 0. \tag{2.42}$$

The importance of (2.41) is that cyclostationary properties provide a way to separate cyclostationary signals from random noise which is purely stationary. As long as the SCD of the received signal is not identically zero, we can perform spectrum sensing by measuring the cyclic spectrum of the received signal.

2.2.7 Application to IEEE 802.22 WRAN

According to [1], ATSC DTV signals are vestigial sideband (VSB) modulated. Before VSB modulation, a constant of 1.25 volts is added to the 8-level pulse amplitude modulated (8-PAM) signal. Therefore, there is a strong pilot tone in the power spectrum density (PSD) of the ATSC DTV signal. Let $z(t)$ be this pilot tone signal which is a sinusoidal signal in the time domain, and further assume that this strong pilot tone is located at frequency f_0 , i.e.,

$$z(t) = \sqrt{2P} \cos(2\pi f_0 t + \theta) \otimes h(t) \tag{2.43}$$

where P and θ are the power and the initial phase of the sinusoidal function, respectively. Here, the function $h(t)$ is the channel impulse response. The received signal must contain the signal

$$y(t) = z(t)e^{j2\pi f_\Delta t} + w(t) \tag{2.44}$$

where $w(t)$ is stationary additive white Gaussian noise and f_Δ is the amount of frequency offset in units of Hz. The cyclic spectrum of the received signal must contain the cyclic spectrum of $y(t)$ which is given by (2.41) and (2.42) where

$$S_y^\alpha(f) = \frac{P}{2}[\delta(f - f_0 - f_\Delta) + \delta(f + f_0 + f_\Delta)]|H(f)|^2 + \sigma^2 \tag{2.45}$$

for $\alpha = 0$ and

$$S_y^\alpha(f) = \frac{P}{2}\delta(f)H(f - f_0 - f_\Delta)H^*(f + f_0 + f_\Delta) \tag{2.46}$$

for $\alpha = \pm 2(f_0 + f_\Delta)$.

Figure 2.6 illustrates the overall procedure of the cyclostationary feature detector. Following [15], the capture data is filtered by a 6 MHz bandpass filer and then scaled so that the signal $x[n]$ has a preset, desired signal power. Then a 6 MHz bandpass noise is added to form the experimental data $y[n]$. Note that the bandpass noise process is still purely stationary. Because we would like to detect the pilot tone in the cyclic spectrum, we can filter out those frequency components other than the pilot tone. Therefore, we apply a narrow bandpass filter to obtain a small band which contains the pilot tone and then perform a D times decimation to reduce the sampling rate in order to reduce the computational complexity. Finally, we compute the cyclostationary feature and make the decision regarding the presence of a signal based on this feature. We will use the frequency average method, (2.26), to compute the SCD of the received signal because it is the best method to compute SCD which contains pilot tones. According to (2.46), the pilot tone appears in zero frequency of the cyclic spectrum. Thus, we compute the zero frequency component of cyclic spectra for several cyclic frequencies and use their maximum value as the decision statistic for the detector

$$T = \max_\alpha |S_y^\alpha[0]|. \tag{2.47}$$

2.2.8 Probability of False Alarm

Hypothesis H_0 corresponds to the presence of noise only, i.e., $y[n] = w[n]$. The random variables $S_w^\alpha[0]$ obtained by using the frequency average method, (2.26), are nearly

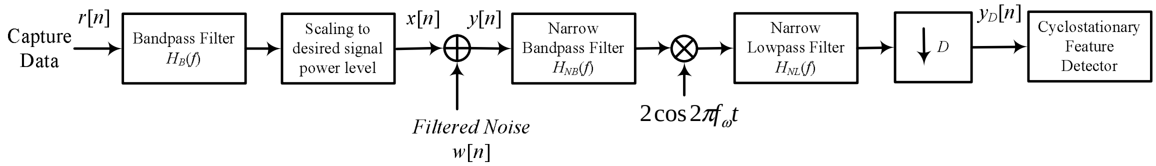

Figure 2.6: System implementation of the Cyclostationary Feature Detector.

i.i.d. circularly symmetric complex Gaussian random variables having zero-mean and variance given by (2.30). Denote the variance obtained by (2.30) as σ_S^2, It can be easily shown that the cumulative distribution function of T is given by

$$F_T(t : H_0) = \left(\int_0^t \frac{2u}{\sigma_S^2} e^{-\frac{u^2}{\sigma_S^2}} du \right)^L \tag{2.48}$$

where L is the number of observed cyclic frequencies. Then, for a particular value of false alarm probability (P_{FA}), the corresponding threshold γ can be found from

$$P_{FA} = 1 - F_T(\gamma : H_0). \tag{2.49}$$

Finally, after some straightforward calculation, we have

$$\gamma = \rho \left(\sigma_S^2 \ln \frac{1}{1 - (1 - P_{FA})^{1/L}} \right)^{1/2}. \tag{2.50}$$

where ρ is an heuristic adjusting factor added artificially to account for the approximation mentioned in Section 2.2.4.

2.2.9 Simulation Results

We use the ATSC A/74 DTV signal captures which are real field captured data to test our spectrum sensing algorithms. The file names of the ATSC DTV signal captures and their corresponding symbols used in the figures illustrating simulation performance results are listed in Table 2.1.

The FSCD Based Algorithms

Figures 2.7 and 2.8 illustrate the operating characteristic curves for the FSCD using a binary sequence ($p[n]$) and a VSB modulated sequence ($s[n]$). We can see that for different capture data, the detection performance is different due to different channel

Symbol	ATSC DTV Capture Date File Name
A	WAS_3_27_06022000_REF
B	WAS_311_36_06052000_REF
C	WAS_06_34_06092000_REF
D	WAS_311_48_06052000_REF
E	WAS_51_35_05242000_REF
F	WAS_68_36_05232000_REF
G	WAS_86_48_07122000_REF
H	WAS_311_35_06052000_REF
I	WAS_47_48_06132000_opt
J	WAS_32_48_06012000_OPT
K	WAS_49_34_06142000_opt
L	WAS_49_39_06142000_opt
Ave	Average

Table 2.1: ATSC DTV Capture Data file names and their corresponding symbols used in the performance figures.

conditions. Generally speaking, the detector using a VSB modulated sequence has better performance than that obtained when using a binary sequence. A total of 12 reference capture data cases were simulated as recommended by [13] [14]. For most cases of DTV capture data, using a VSB modulated sequence, a performance gain of 2 to 3 dB was realized.

The SSAD Based Algorithms

Figure 2.9 illustrates the detection performance of (MC)SSAD when 400 Segment Sync elements are used. When 400 Segment Sync elements are sliced into 8 time slots and the MCSSAD applied, a performance gain of 2.5 dB is realized. There are various restrictions placed on the sensing time according to different reasons given to the tiger team in the development of their spectrum sensing proposals. According to these limitations in sensing time, we evaluate the detection performance of the (MC)SSAD as shown in Fig. 2.10. For the 4.06 ms case, the sensing time is short so that the SSAD detector is applied in that sensing time. For the 9.25 ms case, we slice 9.25 ms into two time slots and then apply the MCSSAD method. As can be seen in Fig. 2.10, for (MC)SSAD, a longer sensing time results better performance.

The Cyclostationarity Based Algorithm

In Fig. 2.6, the real-valued DTV signal capture data $r[n]$ are obtained by sampling DTV channels at a rate of 21.524476 MHz, which is 2X over-sampled and then down converted to have a carrier frequency equal to 5.38 MHz [13] [14]. Because the pilot tone of the capture data is located around 2.69 MHz, the parameter f_ω in Fig. 2.6 is (2.69-f_{IF}) MHz. The bandpass filter used to filter the pilot tone has a bandwidth of 40 kHz and f_{IF} is 17 kHz. The decimation factor is 200 and the decimation filter is a 50 kHz low-pass filter. The size of FFT is 2048. The parameter M in (2.26) is 5 and f_Δ is set to be half of the subcarrier spacing divided by M. The file names of the ATSC DTV signal captures and their corresponding legend symbols used in the simulation figures are listed in Table 2.1. Figures 2.11 and 2.12 show the spectrum sensing performance for $P_{FA} = 0.1$ and $P_{FA} = 0.01$. Both of these simulations use 19.03 ms as the sensing time. We can see from Figs. 2.11 and 2.12 that for average detection performance to achieve P_{MD}=0.1, when P_{FA}=0.1, the needed SNR is -25 dB and when P_{FA}=0.01, the needed SNR is -24.3 dB. It means that the proposed algorithm is not sensitive to a change in the P_{FA} (threshold). This is a desired and important feature of the proposed algorithm. Figure 2.13 shows the spectrum sensing performance for $P_{FA} = 0.1$, and the noise uncertainty equals 1 dB. A 1 dB noise uncertainty means that instead of knowing the exact value of the noise PSD, it has a range of $\pm$ 1 dB. For a more detailed discussion about noise uncertainty, interested readers are referred to [7]. We use the worst case scenario, i.e, the PSD of noise is -95.2185 dBm at room temperature, and we assume that the PSD of noise is -94.2185 dBm to calculate the decision threshold. We can see that with 1 dB of noise uncertainty, for average detection performance to achieve P_{MD}=0.1, when P_{FA}=0.1, the needed SNR is -23 dB which reveals that the proposed spectrum sensing algorithm is not sensitive to the noise uncertainty.

2.3 Conclusions

In this chapter, we introduced several signature-based spectrum sensing algorithms for ATSC DTV signals. From the simulation results, we can see that only the cyclostationarity-based algorithm can easily achieve the spectrum sensing requirements specified by the sensing tiger team of the IEEE 802.22 WG. The reason is that both Segment Sync and Field Sync are not strong features. For the Segment Sync, there are only four symbols for every 832 symbols. For the Field Sync, there is only one Field Sync segment for every 313 segments. Both Segment Sync and Field Sync are very sparse and therefore, it is difficult for algorithms based on these two features to work in the required extremely low SNR environments. The cyclostationary properties can be viewed as a signature of a signal as well. The cyclostationarity-based sensing algorithm described in this chapter relies on the strong pilot tone embedded in the spectrum of the ATSC DTV signals. The pilot tone is a dominant feature so that the sensing algorithms based on it works well in extremely low SNR environments. Furthermore, the noise rejection property of the cyclostationarity-based algorithm permits the performance of spectrum sensing over a shorter sensing time and at a lower complexity.

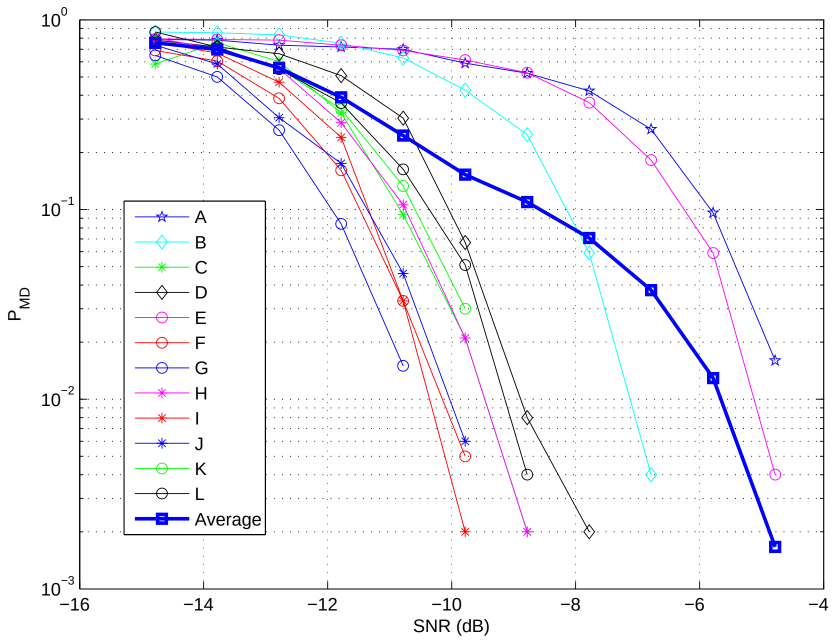

Figure 2.7: Detection performance of the FSCD method using a Binary Sequence.

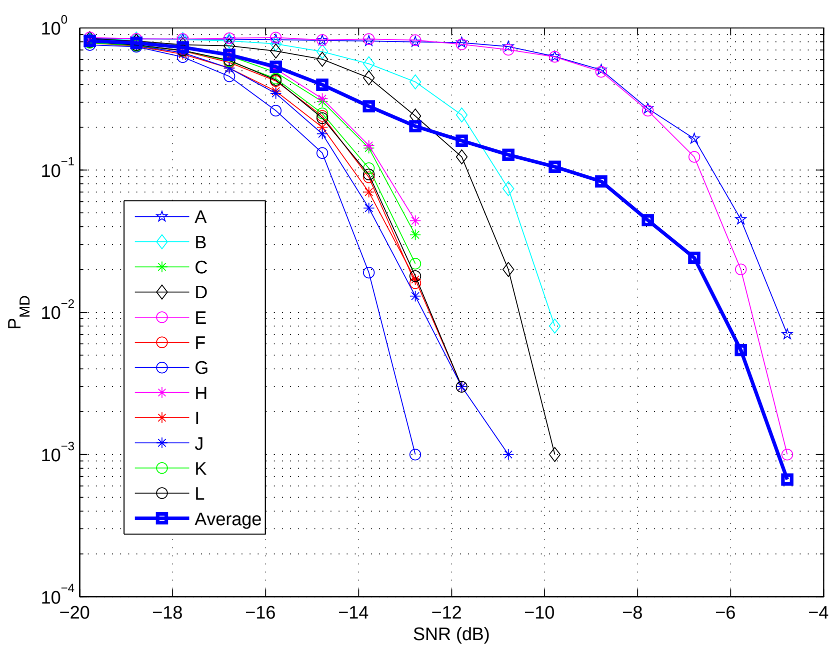

Figure 2.8: Detection performance of the FSCD method using a VSB Modulated Sequence.

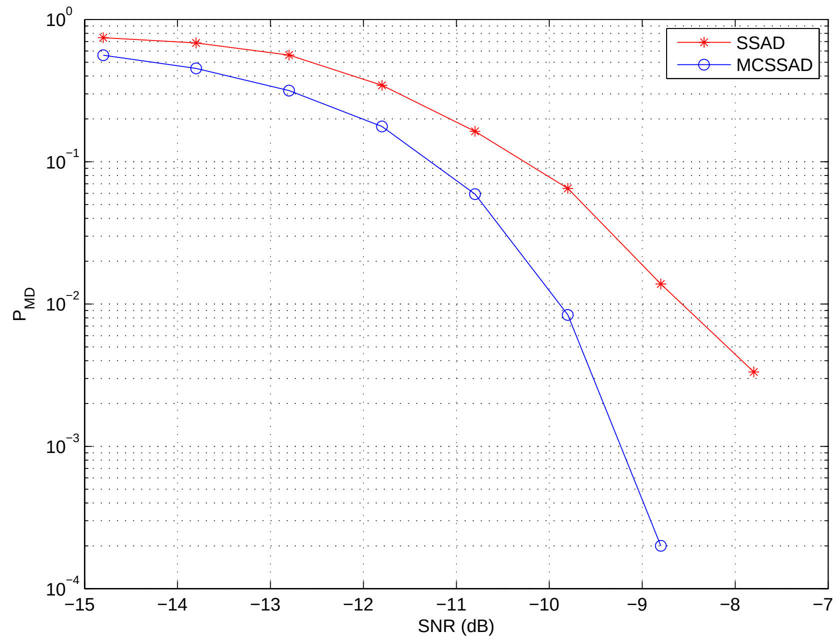

Figure 2.9: Comparison of the detection performance of the SSAD method ($N_D = 400(31ms)$) and the MCSSAD method (averaged over 12 referenced capture data ensembles).

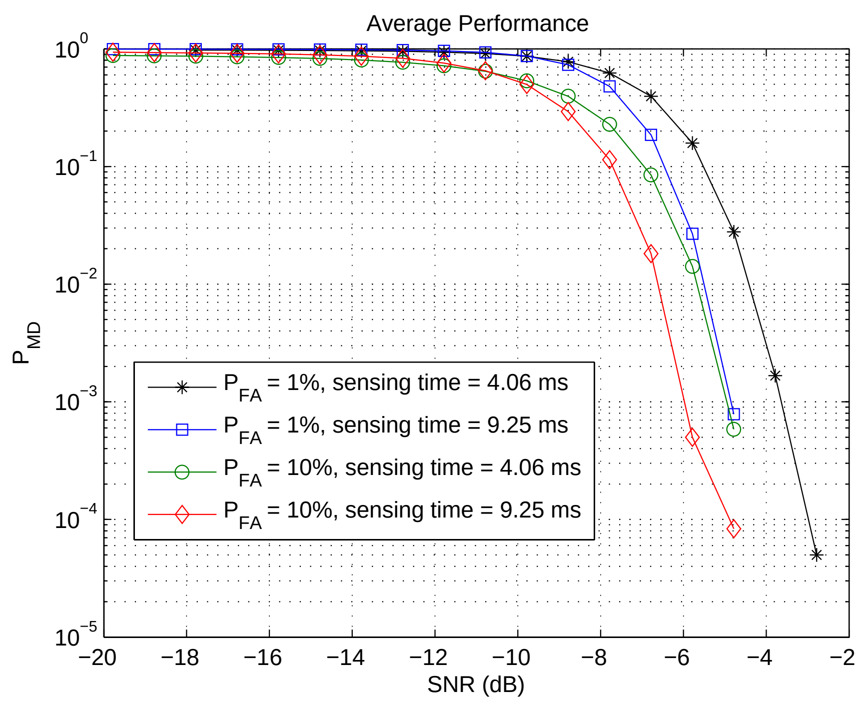

Figure 2.10: Comparison of the detection performance of the SSAD method for different N_D (averaged over 12 referenced capture data ensembles).

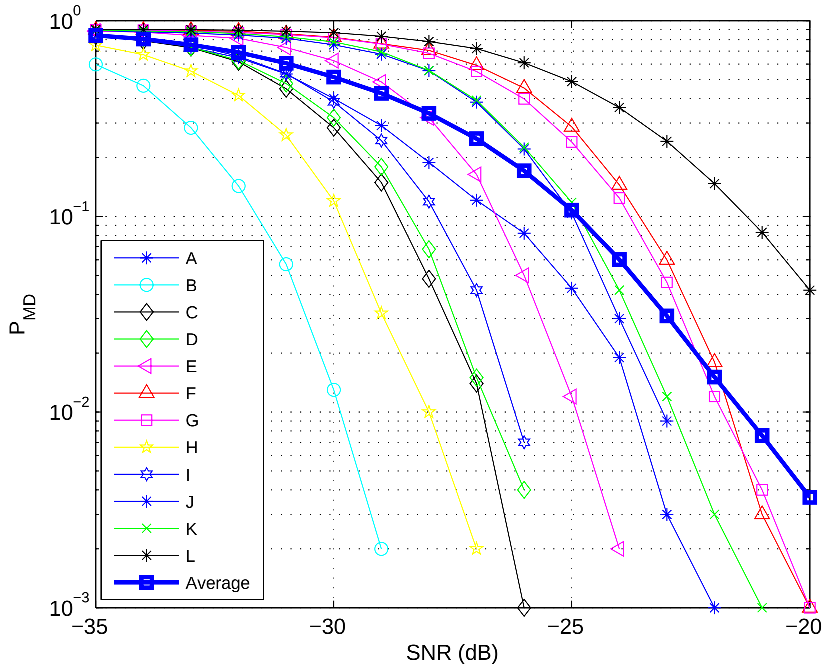

Figure 2.11: Spectrum sensing performance of the Cyclostationary Feature Detector, $P_{FA} = 0.1$ and sensing time=19.03 ms.

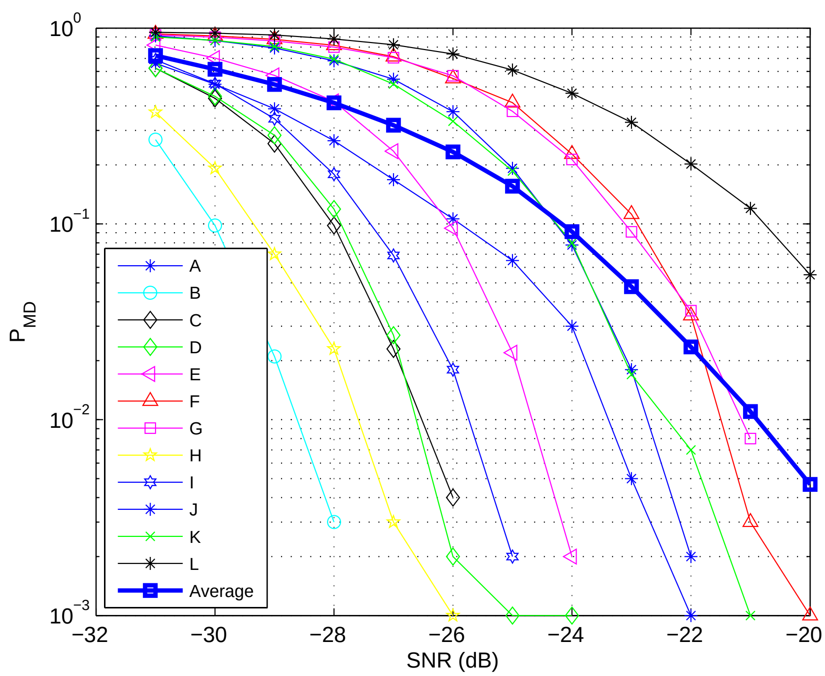

Figure 2.12: Spectrum sensing performance of the Cyclostationary Feature Detector, $P_{FA} = 0.01$ and sensing time=19.03 ms.

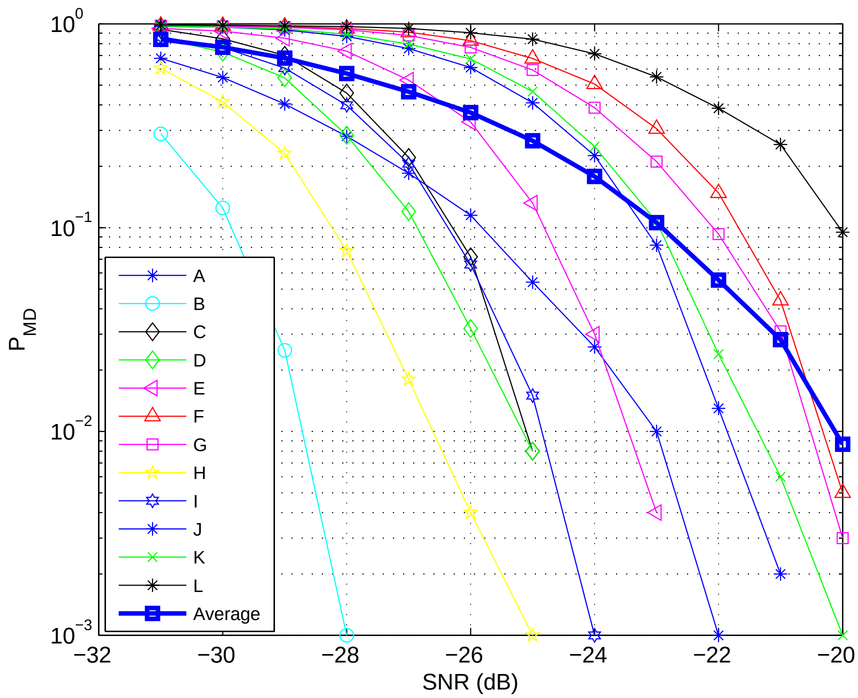

Figure 2.13: Spectrum sensing performance of the Cyclostationary Feature Detector, $P_{FA} = 0.1$, noise uncertainty $=$ 1 dB and sensing time=19.03 ms.

Chapter 3

Spectrum Sensing for ETSI DVB-T Systems

The DTV signal used in North America is that of the ATSC DTV signal [1]. Therefore, the main task in spectrum sensing for IEEE 802.22 WRAN is to detect the existence of the ATSC DTV signal within the DTV bands. Nowadays, OFDM techniques are adopted by many existing or progressing wireless communication standards [2] [25] [26]. Thus, a robust spectrum sensing algorithm for OFDM modulated signals is highly desired to implement CR when the primary signal uses OFDM modulation. Motivated by this demand, a Time-Domain Symbol Cross-Correlation based spectrum sensing algorithm (TDSC method) is presented in this chapter. The algorithm makes use of the property that the mean of the TDSC of two OFDM symbols is not zero if the same frequency-domain pilot tones are embedded in them. The statistical behavior of the proposed spectrum sensor is explicitly analyzed and a theoretical lower bound on the misdetection probability is derived in this chapter. An intuitive spectrum sensing method which utilizes the Cyclic Prefix nature of the OFDM modulated signals (CP method) is also described in this chapter as a reference detection scheme for comparison. Finally, we use the DVB-T Standard [2] as an example of an application model to illustrate the proposed spectrum sensing algorithm. The spectrum sensing algorithms described in this chapter have also been made available in the literature [27]. The spectrum sensing algorithm for OFDM signals that exploits their cyclostationary property has also been reported in [28].

3.1 Statistical Development of the Cross-Correlation Function of Two OFDM Symbols

Under the assumption that L, the length of the Cyclic Prefix (CP), is longer than the length of the time-invariant channel, the n^{th} sample of the l^{th} OFDM symbol can be modeled as

$$x_l[n] = e^{j(2\pi f_\Delta n/N + \theta_l)} \cdot \frac{1}{N} \sum_{k=0}^{N-1} H[k] X_l[k] e^{j2\pi kn/N} + w_l[n] \tag{3.1}$$

where f_Δ is the carrier frequency offset normalized to the subcarrier spacing. The phase $\theta_l = 2\pi f_\Delta lM/N + \theta_0$ is the initial phase of the l^{th} OFDM symbol where $M = N + L$ is the length of an OFDM symbol. The parameter N is the number of subcarriers, and $X_l[k]$ which is taken from a finite complex alphabet constellation denotes the data symbols at the k^{th} subcarrier of the l^{th} OFDM symbol. Moreover, $H[k]$ is the complex channel gain of the k^{th} subcarrier and $w_l[n]$ is a sample of a complex additive white Gaussian noise (AWGN) process. We will assume that $w_l[n]$ is a circularly symmetric complex Gaussian random variable which has zero-mean and a variance of σ_w^2/N. Most of the existing standards which adopt OFDM modulation [2] [25] [26] allocate pilot symbols in the frequency domain. These pilot symbols are called pilot tones. Let $\mathbf{P}_a$, $a = 0, 1, \ldots A-1$, denote the sets of all possible pilot tone positions for the transmitted OFDM symbols. Assume that $\mathbf{P}_{\hat{a}}$ is the set of pilot tone positions of the l^{th} OFDM symbol and $X_l[k] = P_{\hat{a}}[k]$ for $k \in \mathbf{P}_{\hat{a}}$. Here, we should note that the pilot symbols $P_{\hat{a}}[k]$ are predefined and have the same amplitude. For most cases, $P_{\hat{a}}[k]$ is a fixed constant and in some cases they change sign. Assume that the l^{th} and m^{th} OFDM symbols have the same pilot tone positions and define

$$R(l, m) = \frac{1}{N} \sum_{n=0}^{N-1} x_l[n] x_m^*[n] \tag{3.2}$$

which is the Time-Domain Symbol Cross-Correlation (TDSC) function of two OFDM symbols. After some straightforward calculations, it can be shown that

$$\begin{aligned} R(l,m) &= e(l-m)\frac{1}{N^2}\sum_{k\in\mathbf{P}_{\hat{a}}}|H[k]P_{\hat{a}}[k]|^2 \\ &+ e(l-m)\frac{1}{N^2}\sum_{k\notin\mathbf{P}_{\hat{a}}}|H[k]|^2 X_l[k]X_m^*[k] \\ &+ \frac{1}{N^2}\sum_{k=0}^{N-1} H[k]X_l[k]W_m^*[k] \\ &+ \frac{1}{N^2}\sum_{k=0}^{N-1} H^*[k]X_m^*[k]W_l[k] \\ &+ \frac{1}{N}\sum_{n=0}^{N-1} w_l[n]w_m^*[n] \end{aligned} \tag{3.3}$$

where the function $e(\varphi) = e^{j2\pi\varphi M f_\Delta/N}$ represents a phase rotation caused by the carrier frequency offset and

$$W_l[k] = \sum_{n=0}^{N-1}(w_l[n]e^{j(2\pi f_\Delta n/N+\theta_l)})e^{-j2\pi kn/N} \tag{3.4}$$

is the discrete Fourier transform (DFT) of $w_l[n]$ multiplied by a phase rotation. Furthermore, $W_m[k]$ is defined in the same way. Then, by recognizing that $E(X_l[k]X_l^*[u]) = \sigma_s^2\delta(k-u)$ for $k,u \notin \mathbf{P}_a$ and that the received signal and noise are independent, it can be shown that the mean value of $R(l,m)$ is

$$E[R(l,m)] = e(l-m)\cdot\frac{\rho^2}{N^2}\sum_{k\in\mathbf{P}_a}|H[k]|^2 \tag{3.5}$$

and its variance is given by

$$\begin{aligned} &Var[R(l,m)] = \\ &\quad \frac{\sigma_s^4}{N^4}\sum_{k\notin\mathbf{P}_a}|H[k]|^4 + \frac{\sigma_w^2}{N^4}\sum_{k=0}^{N-1}|H[k]X_l[k]|^2 \\ &\quad + \frac{\sigma_w^2}{N^4}\sum_{k=0}^{N-1}|H[k]X_m[k]|^2 + \frac{\sigma_w^4}{N^3} \end{aligned} \tag{3.6}$$

where $\rho^2 = |P_a[k]|^2$. Here we can see that the second term in the right-hand side of (3.3) is the frequency-domain cross-correlation of two received OFDM symbols for non-pilot subcarriers. Its mean is zero and variance is given by the first term of the right-hand side of (3.6). Moreover, the third and fourth terms in the right-hand side of (3.3) are the frequency-domain cross-correlations of the received signal and noise. The means of these two terms are zero and their variances are given by the second and third terms in the right-hand side of (3.6). It can be easily seen that the variances of these three terms are relatively small compared to the last term in the right-hand side of (3.6) especially when the SNR is very small (less than -10 dB). Therefore, it is reasonable to ignore these three terms in (3.3). As a consequence,

$$\begin{aligned} R(l,m) &\cong e(l-m)\cdot\frac{\rho^2}{N^2}\sum_{k\in\mathbf{P}_a}|H[k]|^2 \\ &+ \frac{1}{N}\sum_{k=0}^{N-1} w_l[n]w_m^*[n]. \end{aligned} \tag{3.7}$$

Note that from (3.7), $R(l,m)$ simply consists of a constant term and a noise term. The fact that the mean value of $R(l,m)$ is not zero makes it different from noise, and we are able to exploit this property to perform spectrum sensing.

3.2 TDSC Based Spectrum Sensing Algorithm (TDSC Method)

Let $\nu = l - m$ be the symbol index difference of two OFDM symbols. Note that in all OFDM standards, two OFDM symbols which have their symbol index difference equal to ν have the same pilot tone positions. Further define $C(\nu)$ as the accumulated TDSC function

$$\begin{aligned} C(\nu) &= \frac{1}{S_\nu}\sum_{m-l=\nu} R(l,m) \\ &= e(\nu)\frac{\rho^2}{N^2}\cdot\frac{1}{A}\sum_{a=0}^{A-1}\sum_{k\in\mathbf{P}_a}|H[k]|^2 + \\ &\quad \frac{1}{NS_\nu}\sum_{m-l=\nu}\sum_{k=0}^{N-1} w_l[n]w_m^*[n] \end{aligned} \tag{3.8}$$

where S_ν is the number of $R(l,m)$ which are accumulated and added. Here S_ν is selected to be an integer multiple of A. We can see from (3.8) that the mean of $C(\nu)$ is unchanged no matter how many TDSC are accumulated. However, the variance of the noise term (second term) in $C(\nu)$ is inversely proportional to S_ν. Therefore, as long as the accumulated number of $R(l,m)$, denoted by S_ν, is large enough, the noise term in $C(\nu)$ will be significantly reduced. Due to this property, we are able to perform spectrum sensing in very low SNR environments. For the convenience of derivation and readability, we rewrite $C(\nu)$ as

$$C(\nu) = e(\nu)\Lambda + \xi(\nu) \tag{3.9}$$

where

$$\Lambda = \frac{\rho^2}{N^2} \cdot \frac{1}{A} \sum_{a=0}^{A-1} \sum_{k \in \mathbf{P}_a} |H[k]|^2 \tag{3.10}$$

is the average received signal power in the pilot tone positions divided by N^2 and

$$\xi(\nu) \sim CN(0, \frac{\sigma_w^4}{S_\nu N^3}) \tag{3.11}$$

is a circularly symmetric complex Gaussian random variable. Furthermore, $\xi(\nu)$ and $\xi(\mu)$ are independent for $\nu \neq \mu$. Note that because of the carrier frequency offset, there is a phase term $e(\nu)$ in (3.9) which is a function of $\nu = m - l$. As a result, we cannot linearly combine $C(\nu)$ for different ν. In order to solve this problem, let

$$\begin{aligned} Q(\nu, \nu+d) &= C(\nu)C^*(\nu+d) \\ &= e(-d)\Lambda^2 + \Lambda \cdot (\xi(\nu) + \xi^*(\nu+d)) \\ &\quad + \xi(\nu)\xi^*(\nu+d) \end{aligned} \tag{3.12}$$

which is the conjugate product of two accumulated TDSC functions. It is easily seen that

$$E[Q(\nu, \nu+d)] = e(-d)\Lambda^2 \tag{3.13}$$

and

$$\begin{aligned} &Var[Q(\nu, \nu+d)] = \\ &= \Lambda^2 \cdot (\frac{\sigma_w^4}{S_\nu N^3} + \frac{\sigma_w^4}{S_{\nu+d} N^3}) + \frac{\sigma_w^8}{S_\nu S_{\nu+d} N^6}. \end{aligned} \tag{3.14}$$

Then the phase term embedded in $Q(\nu, \nu+d)$ becomes a function of d, and hence, we can linearly combine $Q(\nu, \nu+d)$ for different ν. Therefore, let Γ be the linear combination of $Q(\nu, \nu+d)$

$$\Gamma = \sum_\nu a_\nu Q(\nu, \nu+d) \tag{3.15}$$

where a_ν is a combining ratio. The problem arises as to how the a_ν should be chosen so as to achieve the best detection performance for a fixed probability of false alarm. However, traditional detection theorems, e.g., Neyman-Pearson and Bayes Risk methods [8], are not suitable to use because the probability distribution functions for both Hypothesis one (H_1) and Hypothesis zero (H_0) are functions of the combining ratios a_ν. Here, we shall use an intuitive criterion. That is, we choose a_ν such that the Kullback-Leibler divergence is maximized. The Kullback-Leibler divergence of two densities f and g is defined by [29]

$$D(f||g) = \int f \log \frac{f}{g}. \tag{3.16}$$

According to the Central Limit Theorem, when the number of terms added in (3.15) is sufficiently large, the probability distribution of Γ for both hypotheses is given by

$$\begin{aligned} p_\Gamma(t;H_1) &\sim CN(\mu, \sigma_1^2) \\ p_\Gamma(t;H_0) &\sim CN(0, \sigma_0^2) \end{aligned} \tag{3.17}$$

where

$$\begin{aligned} \mu &= e(-d)\Lambda^2 \sum_\nu a_\nu \\ \sigma_1^2 &= \sum_\nu a_\nu^2 Var[Q(\nu, \nu+d)] \\ \sigma_0^2 &= \sum_\nu a_\nu^2 \frac{\sigma_w^8}{S_\nu S_{\nu+d} N^6}. \end{aligned} \tag{3.18}$$

For two complex Gaussian random variables, the Kullback-Leibler divergence is given by

$$D(H_1||H_0) = \ln \frac{\sigma_0^2}{\sigma_1^2} + \frac{|\mu - 0|^2}{\sigma_0^2} + \frac{\sigma_1^2}{\sigma_0^2} - 1. \tag{3.19}$$

Then, by computing

$$\frac{\partial D(H_1||H_0)}{\partial a_\nu} = 0 \tag{3.20}$$

for all ν, the optimal combining ratios are obtained. However, (3.20) is too complex to solve. As a result, we make an assumption that σ_0^2 and σ_1^2 are approximately equal in order to obtain suboptimal combining ratios. By substituting $\sigma_0^2 = \sigma_1^2$ into (3.20), we obtain

$$a_\nu = S_\nu S_{\nu+d}. \tag{3.21}$$

Note that this choice of the combining method is essentially that of Maximum Ratio Combining (MRC) [30] if we ignore two cross terms in (3.12). Before defining the decision statistic used for performing spectrum sensing, we should note that the lack of symbol timing information has not been considered in our derivation. When symbol timing is lacking, the usual approach is to try all possible symbol timing instances in order to compute (3.15). Then use the resulting maximum amplitude as the decision statistic. Due to the CP nature of the OFDM signal, our previous derivations are valid as long as the initial sample time instance is taken from any point within an intersymbol interference (ISI) free region [31]. Suppose that the maximum channel delay is D, then the length of the ISI free region is $L - D + 1$. Thus, if we search over $\lceil \frac{N+L}{L-D+1} \rceil$ points which are equally spaced by $L - D$ as the initial sample time instances, there must be one point in the ISI free region. The function $\lceil b \rceil$ is the smallest integer which is larger than or equal to b. Typically, we don't know the maximum channel delay D when we are performing spectrum sensing. Consequently, let $Z = \lceil \frac{N+L}{L} \rceil$, and then use the Z points which are separated by $L - 1$ as initial sample time instances. Although this suboptimal approach will introduce some ISI when none of the Z points are in the ISI free region, the detection performance will not be degraded too much since the ISI introduced is small when the CP length is much larger than the root mean-square (RMS) delay-spread of the wireless channel. Consequently, we use these Z points as initial sample time instances to compute (3.15) and use the maximum amplitude as the decision statistic. Hence, the decision statistic is defined as

$$T_{pt} = \max_{n_0} |\Gamma(n_0)| \tag{3.22}$$

where $\Gamma(n_0)$ is given by (3.15), and we use n_0 as the initial sample time instance.

The approach of performing spectrum sensing by computing time-domain correlation function $R(l, m)$ can be easily applied to any OFDM system employing pilot tones. However, the pilot tone patterns used in various standards are different. Thus, the actual spectrum sensing algorithms that are used might be slightly different. In the next section, we use the DVB-T Standard as an example and describe how to perform spectrum sensing for DVB-T OFDM systems. Through this example, the spectrum sensing algorithm for other OFDM systems which embed pilot tones can be easily developed.

3.3 Spectrum Sensing for DVB-T OFDM Systems

Every transmitted OFDM symbol contains two kinds of pilot tones [2]. One is continued pilot and the other is scattered pilot. The positions of continued pilots are the same for all transmitted OFDM symbols. The scattered pilots are inserted every twelve subcarriers and their positions are shifted by three subcarriers for the next OFDM symbol so that the positions of scattered pilots are repeated every four OFDM symbols, hence we have that

$$\mathbf{P}_{a,scatter} = \{k|k = 12l + 3(a+1)\} \tag{3.23}$$

for $l = 0, 1, \ldots$, and $a = 0, 1, 2, 3$. Therefore, there are four sets of pilot tone patterns for DVB-T OFDM. We should note that the number of scattered pilots is much larger than the number of continued pilots. For a $2K$-subcarrier mode, there are 45 continued pilot tones and 141 scattered pilot tones in an OFDM symbol. Therefore, we shall compute $C(\nu)$ for the case where ν is a multiple of four, except zero, because by doing so, the absolute mean value of $C(\nu)$ is maximized. The decision statistic is given by (3.22) where $\Gamma(n_0)$ is defined by

$$\Gamma = \sum_{k=1}^{K} S_{4k} S_{4k+4} Q(4k, 4k+4) \tag{3.24}$$

and n_0 is used as the initial sample time instance.

3.4 A Lower Bound on the Misdetection Probability for T_{pt}

The probability distribution function of random variables $|\Gamma(n_0)|$ for various n_0 is a joint Rayleigh distribution. The joint Rayleigh distribution for more than four random variables with arbitrary covariance matrix is still an open research problem [32]. Thus, we shall not try to derive the exact probability of misdetection for a specific probability of false alarm. It is obvious that the misdetection probability when using $|\Gamma(\hat{n}_0)|$ as the decision statistic, where $\hat{n}_0$ is a correct symbol timing, will be a lower bound on the misdetection probability for (3.22). The probability distribution of $|\Gamma(\hat{n}_0)|$ for both hypotheses is given by (3.17) and (3.18). For a specific probability of false alarm P_{FA}, the corresponding threshold γ is given by

$$\gamma = \sqrt{-\sigma_0^2 \ln P_{FA}} \tag{3.25}$$

and the corresponding probability of misdetection P_{MD}, which is a lower bound for (3.22), is given by

$$P_{MD} = 1 - Q_{\chi'^2_2(\lambda)}(\frac{\gamma^2}{\sigma_1^2}). \tag{3.26}$$

The function

$$Q_{\chi'^2_2(\lambda)}(x) = \int_x^\infty \frac{1}{2} \exp[\frac{-1}{2}(t+\lambda)] I_0(\sqrt{\lambda t})\, dt \tag{3.27}$$

is the right-tail probability of the non-central Chi-Squared distribution with two degrees of freedom and $\lambda = |\mu|^2/\sigma_1^2$. The function

$$I_0(u) = \int_0^{2\pi} \exp(u \cos\theta) \frac{d\theta}{2\pi} \tag{3.28}$$

is the modified Bessel function of the first-kind and order-zero.

3.5 Algorithms Based on the Cyclic Prefix Property (CP Method)

Due to the CP nature of the OFDM technique, it is straightforward to use the CP to perform coherent detection for spectrum sensing. We shall define the CP correlation function as

$$R_{cp}[n] = \frac{1}{SL} \sum_{u=0}^{S-1} \sum_{m=0}^{L-1} x[n+m+N+uM] x^*[n+m+uM] \tag{3.29}$$

where S is the number of OFDM symbols accumulated for CP correlation and $x[n]$ is the received signal. Noting that symbol timing information is lacking, and that it is expected the absolute value of $R_{cp}[n]$ is maximum for the correct symbol timing. Thus, the decision statistic for the CP method is given by

$$T_{cp} = \max_{0 \le n \le M-1} |R_{cp}[n]|. \tag{3.30}$$

3.6 Probability of False Alarm

3.6.1 TDSC Based Method

As mentioned in Section 3.4, the probability distribution of T_{pt} for hypothesis H_0 is still an open research problem. However, assuming that the random variables $\Gamma(n_0)$ are independent provides a good approximation. Thus for a specific P_{FA}, the corresponding threshold γ_{pt} is given by

$$\gamma_{pt} = \epsilon_{pt} \left(\sigma_0^2 \ln \frac{1}{1 - (1 - P_{FA})^{1/Z}} \right)^{1/2} \tag{3.31}$$

where ϵ_{pt} is an heuristic adjusting factor added artificially to account for the approximation of independence between random variables.

3.6.2 CP Method

For hypothesis H_0 and sufficiently large SL product, by the Central Limit Theorem, $R_{cp}[n]$ in (3.29) approaches a circularly symmetric complex Gaussian distribution, i.e.,

$$R_{cp}[n] \rightarrow CN(0, \frac{\sigma_w^4}{SL}). \tag{3.32}$$

Observing that the random variables $R_{cp}[n]$ are not necessarily independent, once again, we assume that they are independent in order to calculate an approximate threshold. Similarly, for a specific probability of false alarm P_{FA}, the threshold γ_{cp} can be given by

$$\gamma_{cp} = \epsilon_{cp} \left(\frac{\sigma_w^4}{SL} \ln \frac{1}{1 - (1 - P_{FA})^{1/M}} \right)^{1/2} \tag{3.33}$$

where ϵ_{cp} is an heuristic adjusting factor artificially added to account for the approximation mentioned above.

3.7 Simulation Results

The performance of the spectrum sensor for the OFDM signals employing frequency-domain pilot tones is demonstrated by computer simulation. The simulation environments are AWGN, multipath Rayleigh fading, and multipath Ricean channels specified in [2]. The performances on misdetection probability are evaluated for a false alarm probability equal to 0.01 and a sensing time of 50 ms. Both TDSC and CP methods are simulated for four CP ratios defined in [2] and compared to the theoretical lower bound of the TDSC method. From Fig.s' 3.1-3.4, we can see that the TDSC method can achieve a misdetection probability of 0.1 when SNR equals -20.5 dB for four CP ratios. The TDSC method outperforms the CP method in all cases. The TDSC method outperforms CP method for 2 dB and 6 dB when the CP ratio is 1/4 and 1/32, respectively. Furthermore, the TDSC method has approximately the same detection performance for different CP ratios while the detection performance of the CP method degrades dramatically when the CP ratio becomes small. Results also reveal that the simulated performance is very close to the theoretical lower bound indicating that the lower bound can be used as a good prediction of performance.

3.8 Conclusions

An OFDM spectrum sensor which makes use of the existence of the frequency-domain pilot tones was presented in this chapter. The proposed TDSC method requires that only correlations be computed and a small number of amplitude comparison operations are needed to perform spectrum sensing. Hence, it is very low complexity and easy to apply in practice. The simulation results show that the proposed spectrum sensor has excellent performance. The proposed spectrum sensor can achieve a misdetection probability of 0.1 with respect to a probability of false alarm set to 0.01 for a sensing time of 50 ms when the SNR is -20.5 dB. When the TDSC method is compared to the CP method, the TDSC method outperforms the CP methods for the four CP ratios in the range from 2 dB to 6 dB. The simulation results also show that the misdetection probability found by simulation is very close to the lower bound derived in this study. Thus, the lower bound on the misdetection probability given herein can be used as a good prediction of performance. Finally, and most important of all, in this study, we have shown that a simple and accurate spectrum sensing algorithm for OFDM signals does exist and can be easily applied in practical systems.

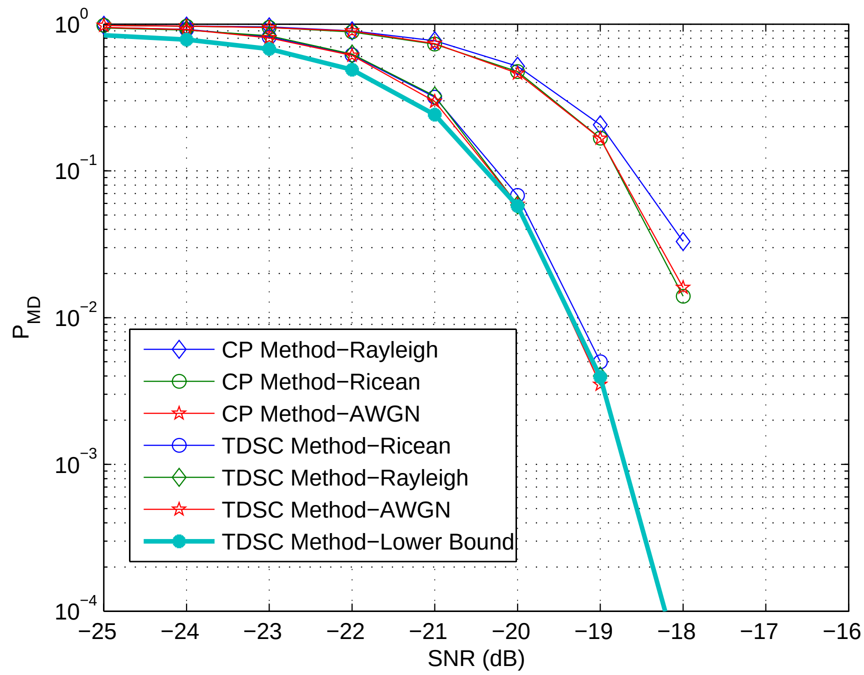

Figure 3.1: Performance comparison of the CP method, TDSC method and its lower bound for $P_{FA} = 0.01$, CP length $= 1/4$ and sensing time $= 50$ ms.

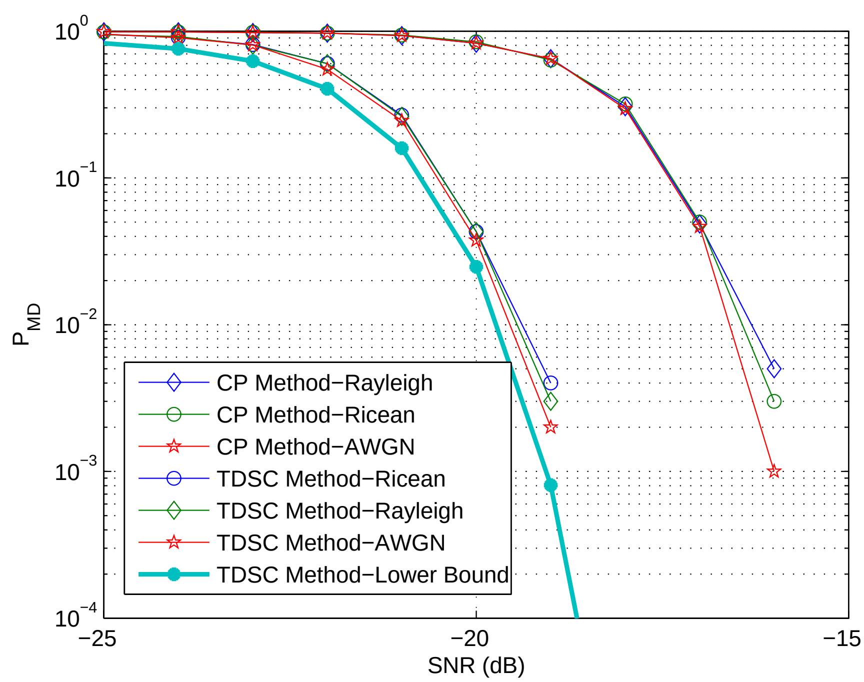

Figure 3.2: Performance comparison of the CP method, TDSC method and its lower bound for $P_{FA} = 0.01$, CP length $= 1/8$ and sensing time $= 50$ ms.

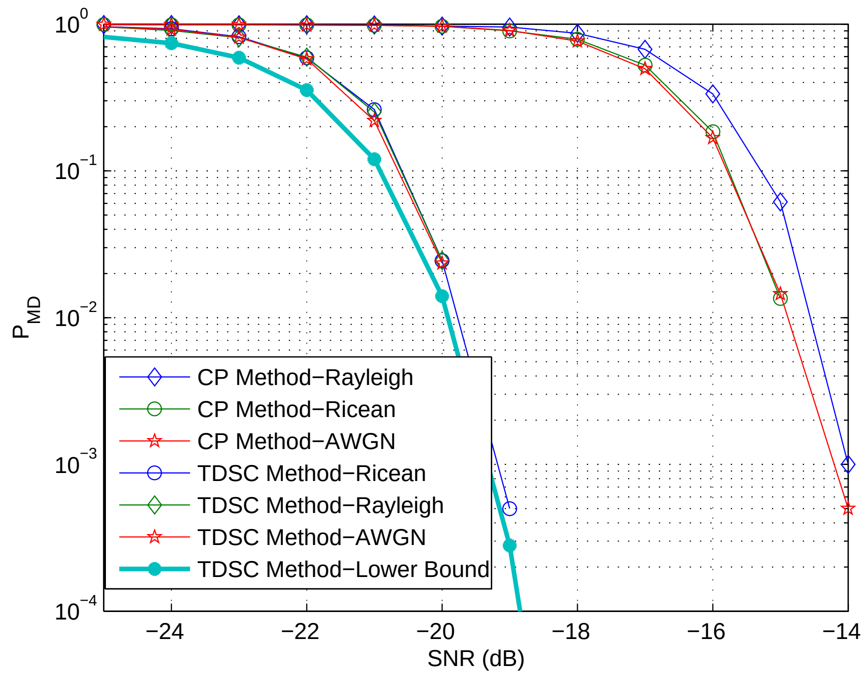

Figure 3.3: Performance comparison of the CP method, TDSC method and its lower bound for $P_{FA} = 0.01$, CP length $= 1/16$ and sensing time $= 50$ ms.

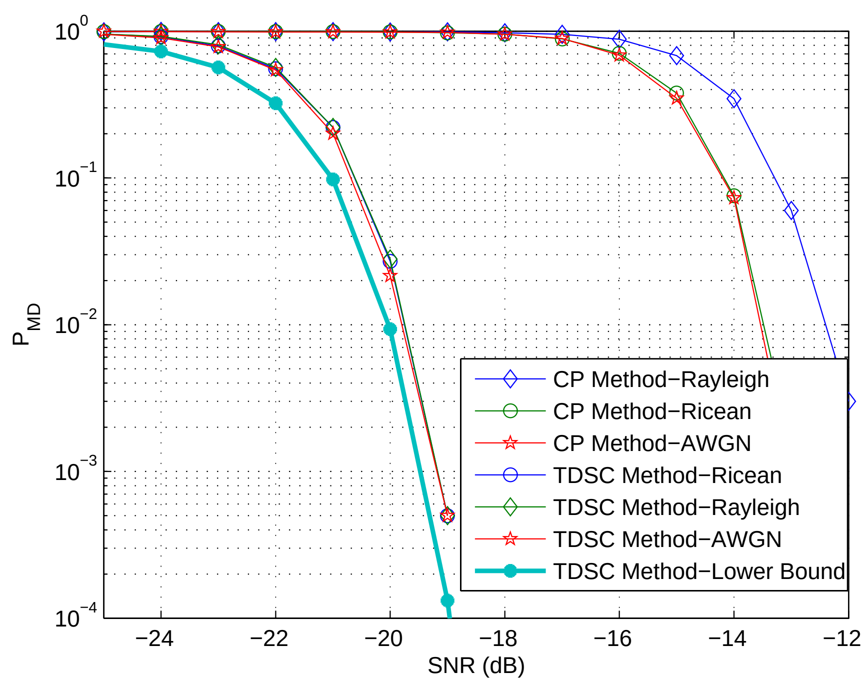

Figure 3.4: Performance comparison of the CP method, TDSC method and its lower bound for $P_{FA} = 0.01$, CP length $= 1/32$ and sensing time $= 50$ ms.

Chapter 4

Spectrum Sensing for NSPRC DMBT Systems

In China, the DTV signal structure is specified by the NSPRC Digital Multimedia Broadcasting-Terrestrial (DMB-T) Standard [3]. Therefore, spectrum sensing algorithms which are dedicated to DTV signals in China are needed. In DMB-T systems, a time-domain synchronous OFDM (TDS-OFDM) technique is adopted. Instead of cyclic prefixes, pseudonoise (PN) sequences are inserted as guard intervals. The DMB-T signals consist of signal frames. A signal frame consists of a frame header and a frame body. There are three frame header modes defined in the DMB-T Standard. Although the frame headers of different modes consist of PN sequences, the structures for the different modes are different. As a consequence, different spectrum sensing algorithms are designed for different frame header modes. A theoretical lower bound on the misdetection probability for each spectrum sensor is derived in this chapter. The performances of the spectrum sensing algorithms presented in this study are demonstrated by computer simulations and compared to corresponding lower bounds on the misdetection probability. The spectrum sensing algorithms described in this chapter has also been made available in the literature [34].

4.1 Frame Structure of the DMB-T System

First, we briefly describe the signal frame structure of the DMB-T system [3]. As shown in Fig. 4.1, a signal frame consists of two parts. The first part is that of a frame header which contains a PN sequence serving as pilot symbols. The second part is the frame body which contains information symbols. Three signal frame structures are defined in [3] according to the length of the frame header. The frame header may contain 420, 595, or 945 symbols within the PN sequence. These three frame structures have the same frame body length and a frame body contains $N = 3780$ information symbols. For Frame Header Mode 1, as shown in Fig. 4.2, the frame header contains $L_1 = 420$ symbols (PN420) which consist of one front synchronization, one PN255 sequence and one rear synchronization. The front and rear synchronizations are cyclic extensions of the PN255 sequence. The length of the front synchronization is 82 symbols and the length of the rear synchronization is 83 symbols. For Frame Header Mode 1, a group of 225 signal frames form a superframe and these 225 frames use PN sequences generated by the same 8th-order linear shift register but have different initial phases. For Frame Header Mode 2, the frame header contains $L_2 = 595$ symbols (PN595) which is truncated from a 10th-order maximum length sequence. For Frame Header Mode 2, a group of 216 signal frames form a superframe. Unlike Frame Header Mode 1, all frame headers contain the same PN595 sequence. The structure of Frame Header Mode 3 is similar to the structure of frame mode 1 as shown in Fig. 4.2. The frame header contains $L_3 = 945$ symbols (PN945). The front and rear synchronizations are cyclic extensions of the PN511 sequence. The lengths of both the front and rear synchronizations are 217 symbols. For Frame Header Mode 3, a group of 200 signal frames form a superframe and these 200 frames use PN sequences generated by the same 9th-order linear shift register having different initial phases.

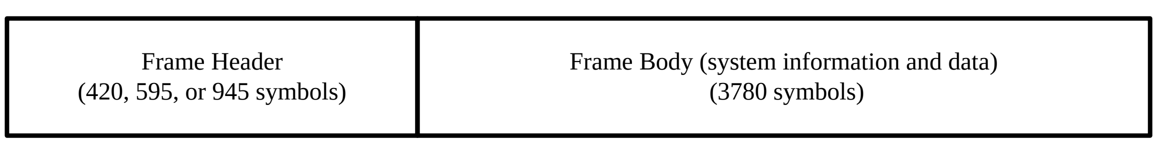

Figure 4.1: Signal frame structure used in the DMB-T system.

Front Synchronization 82 (217) symbols	PN 255 (511)	Rear Synchronization 83 (217) symbols

Figure 4.2: Frame header structure, PN420 (PN945), of the DMB-T system.

4.2 Spectrum Sensing for Frame Header Mode 2

4.2.1 The PN Correlation (PNC) Method

For Frame Header Mode 2, all frame headers contain the same PN595 sequence. Because the PN595 sequence is only a part of the whole PN sequence, it is difficult to use any property related to PN sequences to perform spectrum sensing. As a result, we simply utilize the correlation of PN595 in two consecutive frame headers as the basic approach to perform spectrum sensing for Frame Header Mode 2. Let

$$r[n] = y[n] + w[n] \tag{4.1}$$

where $y[n]$ is the received signal and $w[n]$ is an additive white Gaussian noise (AWGN). We will assume that $w[n]$ is a complex circularly symmetric Gaussian random variable which has zero-mean and a variance of σ_w^2. Because every frame header contains the same PN595 sequence, it can be expected that the correlation of two consecutive frame headers will generate a peak amplitude. Following this approach, we define the decision statistic of the PN Correlation (PNC) method for Frame Header Mode 2 as

$$T_{pnc,2} = \max_{0 \le m \le M_2 - 1} |t_{pnc,2}(m)| \tag{4.2}$$

where

$$\begin{aligned} t_{pnc,2}(m) = \frac{1}{S_2 L_2} \sum_{n=0}^{S_2-1} \sum_{k=0}^{L_2-1} & r[m + k + nM_2] \\ & \cdot r^*[m + k + (n+1)M_2] \end{aligned} \tag{4.3}$$

The parameter $M_2 = N + L_2$ is the length of a signal frame for Frame Header Mode 2 and S_2 is the number of signal frames used to perform spectrum sensing.

4.2.2 A Lower Bound on the Misdetection Probability for T_{pnc2}

Note that in (4.2), because the timing information is lacking, M_2 possible initial frame sampling instances were tried. We use the maximum amplitude over all trials as the decision statistic. The detector defined in (4.2) is suboptimal compared to the detector with perfect timing information. The performance of the operating detector defined in (4.2) will be bounded by the performance of the detector with perfect timing information [8]. We will use this idea to derive a lower bound on the misdetection probability for all detectors considered in this study. Therefore we give a general description and derivation here.

Let $t(n_0)$ be a decision statistic of a detector which uses n_0 as initial frame sample time instance and assume that $t(n_0)$ is a complex random variable. Let $\hat{T} = |t(\hat{n}_0)|$ where $\hat{n}_0$ is the correct initial frame sample time instance. Therefore $\hat{T}$ is the decision statistic of the detector with perfect timing information. Let $\tilde{T}$ be decision statistic of the detector that lacks precise timing information. Then, without the use of special conditions, an exhaustive search for all possible initial frame sample time instances is usually used. Thus, a detector having the decision statistic $\tilde{T} = \max_{n_0} |t(n_0)|$ is the general detector structure when we use $t(n_0)$ as decision statistic and timing information is unavailable. The detection performance of $\tilde{T}$ is bounded by the detection performance of $\hat{T}$. If the probability distribution functions for both hypothesis H_1 (signal plus noise) and H_0 (noise only) for $t(\hat{n}_0)$ are given as

$$\begin{aligned} p_{t(\hat{n}_0)}(t; H_1) &\sim CN(\mu, \sigma_1^2) \\ p_{t(\hat{n}_0)}(t; H_0) &\sim CN(0, \sigma_0^2) \end{aligned} \tag{4.4}$$

where $CN(\mu, \sigma^2)$ denotes a complex Gaussian distribution with mean μ and variance σ^2. Then, the random variable $\hat{T}$ is Rayleigh distributed for hypothesis H_0 and is Rician distributed for hypothesis H_1. For a specific probability of false alarm P_{FA}, the corresponding threshold $\gamma_{\hat{T}}$ is given by

$$\gamma_{\hat{T}} = \sqrt{-\sigma_0^2 \ln P_{FA}} \tag{4.5}$$

and the corresponding probability of misdetection probability $P_{MD,\hat{T}}$ is given by

$$P_{MD,\hat{T}} = 1 - Q_{\chi'^2_2(\lambda)}(\frac{\gamma^2_{\hat{T}}}{\sigma^2_1}) \tag{4.6}$$

where the function

$$Q_{\chi'^2_2(\lambda)}(x) = \int_x^\infty \frac{1}{2}\exp[\frac{-1}{2}(t+\lambda)]I_0(\sqrt{\lambda t})\ dt \tag{4.7}$$

is the right-tail probability of the non-central Chi-Squared distribution with two degrees of freedom and $\lambda = |\mu|^2/\sigma_1^2$. The function

$$I_0(u) = \int_0^{2\pi} \exp(u\cos\theta)\frac{d\theta}{2\pi} \tag{4.8}$$

is the modified Bessel function of the first-kind and order-zero. Then, the misdetection probability calculated according to (4.6) is a performance lower bound on the misdetection probability for the detector which uses $\tilde{T}$ as a decision statistic.

Let $\hat{T}_{pnc,2} = |t_{pnc,2}(\hat{m}_0)|$ where $\hat{m}_0$ is the correct initial frame sample time instance. Then, from the Central Limit Theorem, for sufficiently large S_2L_2, the probability distribution functions of $t_{pnc,2}(\hat{m}_0)$ for both hypothesis H_1 (signal plus noise) and H_0 (noise only) will approach circularly symmetric complex Gaussian distributions

$$\begin{aligned} p_{t_{pnc,2}(\hat{m}_0)}(t;H_1) &\sim CN(\sigma_p^2, \frac{2\sigma_p^2\sigma_w^2+\sigma_w^4}{S_2L_2}) \\ p_{t_{pnc,2}(\hat{m}_0)}(t;H_0) &\sim CN(0, \frac{\sigma_w^4}{S_2L_2}) \end{aligned} \tag{4.9}$$

where the parameter σ_p^2 is the average energy of the received signal frame header. Then by substituting the parameters of (4.9) into (4.5) and (4.6), we can obtain a lower bound for the misdetection probability of the PNC detector for Frame Header Mode 2.

4.3 Spectrum Sensing for Frame Header Mode 1 and Mode 3

4.3.1 The Cyclic Extension Correlation (CEC) Method

As shown in Fig. 4.2, for Frame Header Modes 1 and 3, a frame header consists of a PN sequence and its cyclic extension. Thus, the first 165 (434) symbols of the frame header are a repetition of the last 165 (434) symbols of the frame header for Frame

Header Mode 1 (mode 3). It is intuitive to use the correlation of these two components to perform spectrum sensing. Define the decision statistic of the CEC method as

$$T_{cec,i} = \max_{0 \le m \le M_i} |t_{cec,i}(m)|, \quad i = 1, 3 \tag{4.10}$$

with

$$\begin{aligned} t_{cec,i}(m) = \frac{1}{S_i C_i} \sum_{n=0}^{S_i-1} \sum_{k=0}^{C_i-1} r[m + k + nM_i] \\ \cdot r^*[m + k + G_i + nM_i], \quad i = 1, 3 \end{aligned} \tag{4.11}$$

where $C_1 = 165$ ($C_3 = 434$) is the number of the cyclic extended symbols and $G_1 = 255$ ($G_3 = 511$) is the length of the PN sequence for Frame Header Mode 1 (mode 3). The parameter $M_i = N + L_i$ is the length of a signal frame for Frame Header Mode i, and $i = 1, 3$.

4.3.2 A Lower Bound on the Misdetection Probability for $T_{cec,i}$

Similarly, let $\hat{T}_{cec,i} = |t_{cec,i}(\hat{m}_0)|$ where $\hat{m}_0$ is the correct initial frame sample time instance. Then, from the Central Limit Theorem, for sufficiently large $S_i C_i$, the probability distribution functions of $t_{cec,i}(\hat{m}_0)$ for both hypothesis H_1 and H_0 will approach complex Gaussian distributions

$$\begin{aligned} p_{t_{cec,i}(\hat{m}_0)}(t; H_1) &\sim CN(\sigma_p^2, \frac{2\sigma_p^2 \sigma_w^2 + \sigma_w^4}{S_i C_i}) \\ p_{t_{cec,i}(\hat{m}_0)}(t; H_0) &\sim CN(0, \frac{\sigma_w^4}{S_i C_i}). \end{aligned} \tag{4.12}$$

Again, by substituting the parameters of (4.12) into (4.5) and (4.6), we can obtain a lower bound on the misdetection probability for the CEC detector for Frame Header Mode 1 and mode 3.

4.3.3 The PN Correlation Method

For Frame Header Modes 1 and 3, the signal frame headers in a superframe use PN sequences which are generated by the same linear shift register having different initial phases. These PN sequences are cyclic shifts of each other. The initial phases of the PN sequences for each signal frame of a superframe are listed in [3]. After computer verification, we found that the PN sequences have the following structure. Let the PN sequence in the first signal frame be a reference PN sequence and, let $P_i(l)$ be the PN sequence which is cyclically right shifted by l places relative to the reference PN sequence for Frame Header Mode i. Then

$$F_1(l) = \begin{cases} P_1(l/2), & l = 0, 2, \ldots, 112 \\ P_1(254 - (l-1)/2), & l = 1, 3 \ldots, 111 \\ F_1(224 - 1 - l), & l = 113, \ldots, 224 \end{cases} \tag{4.13}$$

and for Frame Header Mode 3, we have that

$$F_3(l) = \begin{cases} P_3(l/2), \quad l = 0, 2, 4, \ldots, 100 \\ P_3(510 - (l-1)/2), \quad l = 1, 3, 5, \ldots, 99 \\ F_3(200 - l), \quad l = 101, 102, \ldots, 199 \end{cases} \tag{4.14}$$

where $F_1(l)$ ($F_3(l)$) is the PN sequence which is used in the l^{th} signal frame for Frame Header Mode 1 (mode 3). Although the PN sequences used in signal frames of a superframe follow the rules given in (4.13) and (4.14), it is still not easy to utilize the properties associated with PN sequence and the rules to perform spectrum sensing because the PN sequence in every other signal frame is not always cyclically right-shifted or left-shifted. However, except for the two signal frames in the middle, the cyclic shift of the PN sequence for every other signal frame is either one place to the right or one place to the left. Therefore, we define the decision statistic associated with the PNC method for Frame Header Mode 1 and Mode 3 as

$$T_{pnc,i} = \max_{0 \le m \le \lceil M_i/C_i \rceil - 1} |t_{pnc,i}(m)| \tag{4.15}$$

where

$$\begin{aligned} t_{pnc,i}(m) = \frac{1}{2S_iG_i} \sum_{n=0}^{S_i-1} \sum_{a=0}^{1} \sum_{k=0}^{G_i-1} r[mC_i + k + nM_i] \\ \cdot r^*[mC_i + k + (n+2)M_i + (-1)^a] \quad i = 1, 3 \end{aligned} \tag{4.16}$$

Note that because of the cyclic extension of the PN sequence in the frame header, as long as the initial sample is taken from the first 165 (434) symbols for Frame Header

Mode 1 (Mode 3), we can obtain the entire PN255 (PN511) sequence. Thus, instead of searching over M_i possible initial frame sampling time instances, we only need to try $\lceil M_i/C_i \rceil$ points which are uniformly separated by $C_i - 1$. The function $\lceil b \rceil$ is the smallest integer which is larger than or equal to b. It is easily seen that one of these points will fall within the first 165 (434) symbols. For the multipath channels, this approach is not completely correct. However, the performance will not degrade too much as long as the length of the cyclic extension is much larger than the root mean-square (RMS) delay-spread of the wireless channel.

4.3.4 A Lower Bound on the Misdetection Probability for $T_{pnc,1}$ and $T_{pnc,3}$

Again, let $\hat{T}_{pnc,i} = |t_{pnc,i}(\hat{m}_0)|, i = 1, 3$ where $\hat{m}_0$ is the correct initial frame sample time instance. Then, from the Central Limit Theorem, for sufficiently large $S_i C_i$, the probability distribution functions of $t_{cec,i}(\hat{m}_0)$ for both hypothesis H_1 and H_0 will approach circularly symmetric complex Gaussian distributions

$$\begin{aligned} p_{t_{pnc,i}(\hat{m}_0)}(t; H_1) &\sim CN(\frac{\sigma_p^2}{2}, \frac{\sigma_p^4 + 4\sigma_p^2\sigma_w^2 + 2\sigma_w^4}{4S_iG_i}) \\ p_{t_{pnc,i}(\hat{m}_0)}(t; H_0) &\sim CN(0, \frac{\sigma_w^4}{2S_iG_i}). \end{aligned} \tag{4.17}$$

Then, by substituting the parameters of (4.17) into (4.6), we can obtain a lower bound on the misdetection probability for the PNC detector for Frame Header Mode 1 and Mode 3.

4.4 Probability of False Alarm

Following the terminology that was used in deriving a lower bound on misdetection probability in Section 4.2.2, let $t(n_0)$ be a decision statistic of a detector which uses n_0 as an initial frame sample time instance. For hypothesis H_0, which corresponds to the presence of noise only, the random variable $t(n_0)$ is a circularly symmetric Gaussian random variable. The random variables $t(n_0)$ for a period of time instances are identical, but not necessarily, independently distributed. Therefore the random variable $\tilde{T} =$

$\max_{n_0} |t(n_0)|$ is jointly Rayleigh distributed and the joint Rayleigh distribution for more than four random variables with arbitrary covariance matrix is still an open research problem [32]. However, assuming that the random variables $t(n_0)$ are independent provides a good approximation. Thus for a specific P_{FA}, the corresponding threshold $\gamma_{\tilde{T}}$ is given by

$$\gamma_{\tilde{T}} = \epsilon_{\tilde{T}} \left(\sigma_0^2 \ln \frac{1}{1 - (1 - P_{FA})^{1/W}} \right)^{1/2} \tag{4.18}$$

where $\epsilon_{\tilde{T}}$ is an heuristic adjusting factor added artificially to account for the approximation of independence between the random variables, and W is the number of time instances that were considered.

4.5 Simulation Results

The performances of the proposed spectrum sensing methods are demonstrated via computer simulations. The probability of false alarm and sensing time are set to 0.01 and 50 ms, respectively. The simulated channel environments are the steady state multipath Rayleigh channel and multipath Rayleigh fading channel with root mean square (RMS) delay spread equal to 1.24 μs (9.37 samples). Here, each path of the steady state multipath Rayleigh fading channel is multiplied by a constant path gain. Thus, for each single path, its envelope is a constant and the Rayleigh fading occurs due to the sum of these paths. For the multipath Rayleigh fading channel, the envelope of each single path is Rayleigh distributed and the channel gains of each path are generated in accordance with Jakes fading model [33]. For Frame Header Mode 2, as shown in Fig. 4.3, the probability of misdetection (P_{MD}) equal to 0.1 is achieved when the SNR is -18.8 dB for the multipath Rayleigh fading channel and -19.8 dB for the steady state channel. For Frame Header Mode 1, as shown in Fig.s 4.4 and 4.5, the performances of the CEC and PNC methods are approximately the same. A P_{MD} equal to 0.1 is achieved when the SNR is -16 dB for a multipath Rayleigh fading channel and -17.2 dB for the steady state channel. For Frame Header Mode 3, as shown in Fig.s 4.6 and 4.7, the CEC method outperforms the PNC method. A P_{MD} equal to 0.1 is achieved when the SNR is -18.5 dB for the multipath Rayleigh fading channel and -18 dB for the steady state channel. In all figures, the performance of the steady state channel is close to the theoretical lower bound indicating that the lower bound can be used as a good of performance predictor for the spectrum sensing algorithm.

4.6 Conclusions

Spectrum sensing for DMB-T systems using PN frame headers has been considered in this chapter. Spectrum sensing algorithms which make use of the cyclic extension of the PN sequence in frame headers and PN structures associated with frame headers in a superframe are described in detail. The statistical analysis of all the detectors considered in this study has been provided and a corresponding lower bound of misdetection probability has been given. The performances of the proposed spectrum sensing algorithms are demonstrated by computer simulation for the multipath Rayleigh fading and steady state multipath Rayleigh fading channels. Simulation results show that the misdetection probability evaluated by computer simulations is close to the lower bound on the misdetection probability for a steady state multipath Rayleigh channel. When the probability of false alarm is 0.01 and a 50 ms of sensing time is used, a misdetection probability equal to 0.1 is achieved when the signal to noise power ratio is -16 dB, -18.8 dB, and -18 dB for Frame Header Modes 1, 2, and 3 in the multipath Rayleigh fading channel, respectively. Furthermore, the lower bound on the misdetection probability developed in this study yields a good prediction of the spectrum sensing performance.

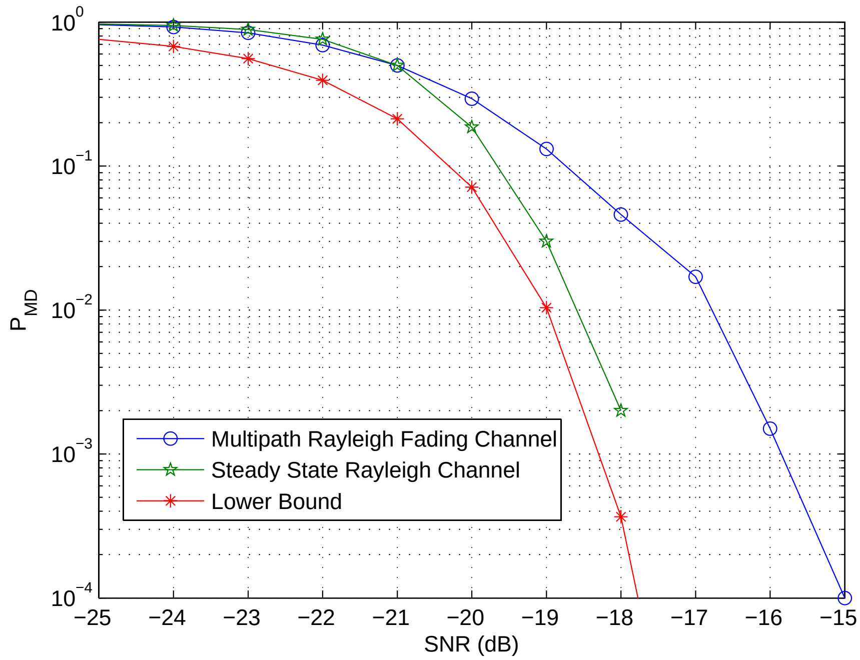

Figure 4.3: Spectrum sensing performance of the PNC method for Frame Header Mode 2 and its lower bound for $P_{FA} = 0.01$ and sensing time = 50 ms.

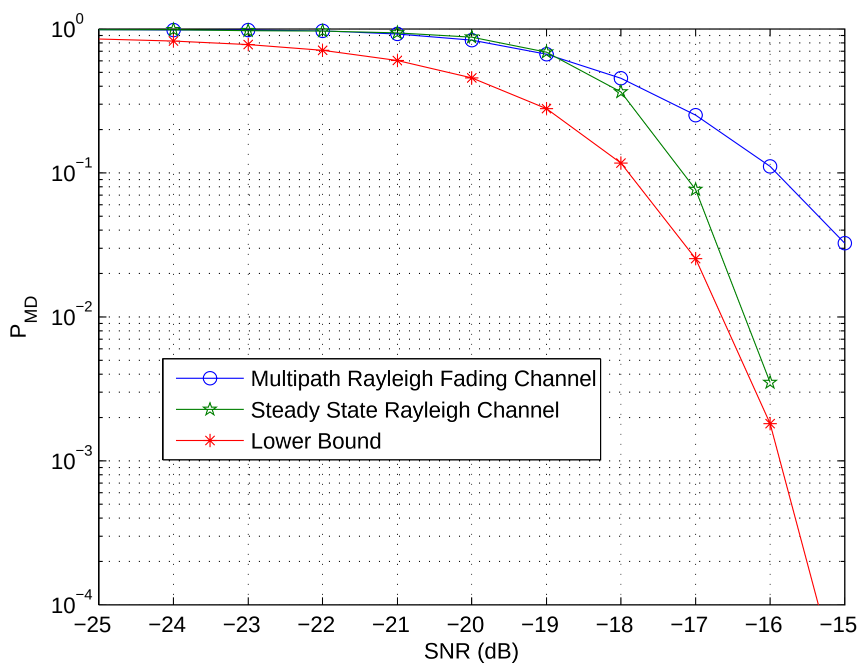

Figure 4.4: Spectrum sensing performance of the CEC method for Frame Header Mode 1 and its lower bound for $P_{FA} = 0.01$ and sensing time = 50 ms.

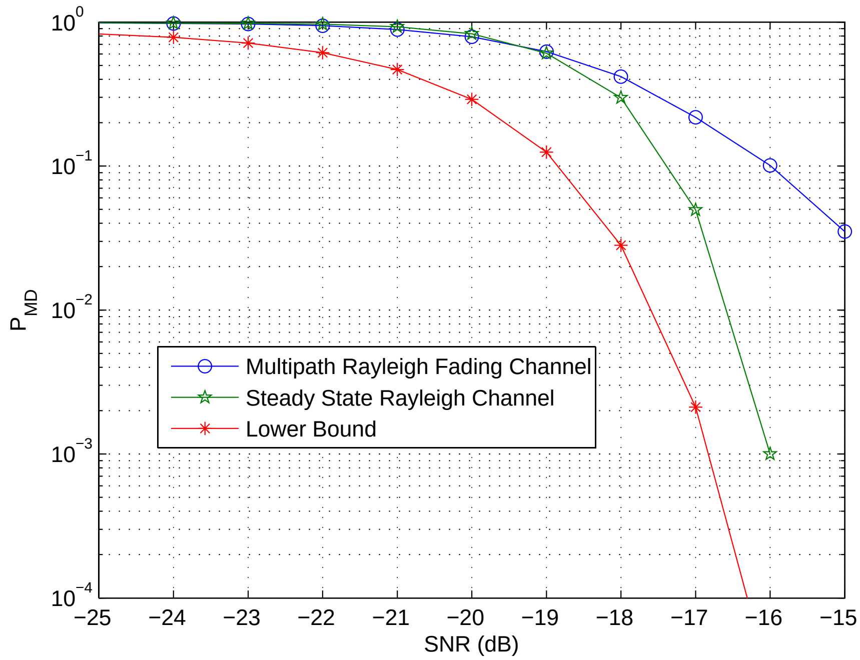

Figure 4.5: Spectrum sensing performance of the PNC method for Frame Header Mode 3 and its lower bound for $P_{FA} = 0.01$ and sensing time = 50 ms.

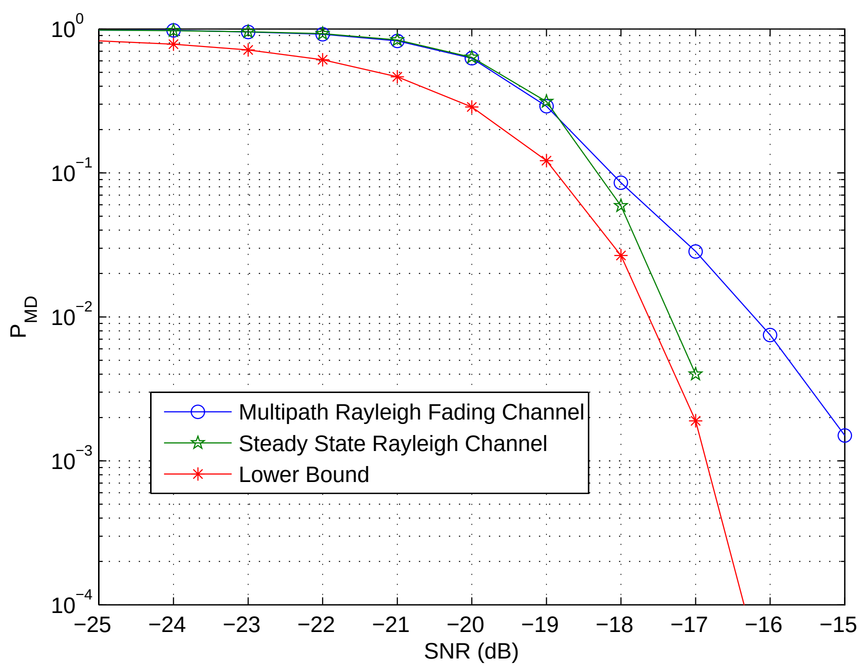

Figure 4.6: Spectrum sensing performance of the CEC method for Frame Header Mode 1 and its lower bound for $P_{FA} = 0.01$ and sensing time = 50 ms.

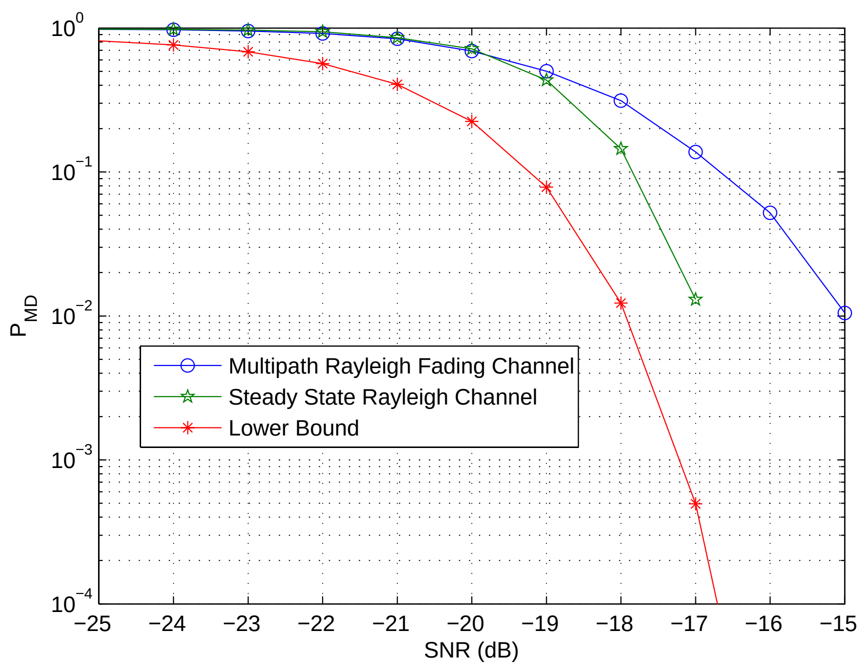

Figure 4.7: Spectrum sensing performance of the PNC method for Frame Header Mode 3 and its lower bound for $P_{FA} = 0.01$ and sensing time $= 50$ ms.

Chapter 5

Spectrum Sensing for Wireless Microphone Signals

Wireless microphones are low-power secondary licensed signals operated in the locally unused DTV bands. Therefore, the main task in spectrum sensing for IEEE 802.22 WRAN also includes the detection of the existence of a wireless microphone signal. From various signal models of the wireless microphone [38] [40], it is found that the power of the WM signal is highly concentrated in the frequency domain. Due to this property, spectrum sensing can be performed by simply detecting the maximum peak of the estimated PSD of the received signal. The probability of false alarm is analytically derived for the WM detector presented in this chapter. The performance of the WM detector is demonstrated by computer simulations using WM signal models provided in [38] [40]. The spectrum sensing algorithms described in this chapter have also been made available in the literature [35].

5.1 Characteristics of Wireless Microphone Signals

Most of the wireless microphone devices use analog frequency modulation (FM) and the signal bandwidth is less than 200 kHz [36]. Let $m(t)$ be the voice signal, then the transmitted FM signal $s(t)$ can be generated by

$$s(t) = A_c \cos\left[2\pi f_c t + 2\pi k_f \int_0^t m(\tau)d\tau\right] \tag{5.1}$$

where A_c is the carrier amplitude [37]. The term f_c is the carrier frequency, and the constant k_f is the frequency sensitivity of the modulator. In [38], three wireless microphone operating situations and two environment conditions are suggested to test spectrum sensing algorithms for wireless microphone signals. As a consequence, there are six wireless microphone signal models. The three system operating situations are:

1. Silent:

   The system user is silent. In this situation, $m(t)$ is a 32 kHz sinusoid signal and the FM deviation factor is ± 5 kHz.

2. Soft Speaker:

   The system user is a soft speaker. In this situation, $m(t)$ is modeled as a 3.9 kHz sinusoid signal with the FM deviation factor being ± 15 kHz.

3. Loud Speaker:

   The system user is a loud speaker. In this situation, $m(t)$ is modeled as a 13.4 kHz sinusoid signal with the FM deviation factor being ± 32.6 kHz.

The two environmental conditions are:

1. Outdoor, LOS:

   In this case, the wireless microphone system is used in an outdoor environment where a line of sight (LOS) transmission path between transmitter and receiver exists. Therefore, it is an AWGN channel model.

2. Indoor, Rayleigh Faded:

   In this case, the wireless microphone system is used indoors. Because the distance

> between transmitter and receiver is short, a single-path Rayleigh fading channel is good enough to model the indoor channel. Therefore, a flat fading channel is used. Moreover, the speed of the user is assumed to be 0.6 m/s. At this speed, and a possible maximum carrier frequency of 806 MHz, the maximum Doppler shift is computed to be 1.612 Hz. Because the maximum Doppler shift is very small, the Doppler effect can be ignored. Hence, this channel is a single-path time-invariant channel.

Furthermore, a more accurate model of voice signals is used in [39] [40]. The audio signal $m(t)$ is simulated using colored noise generated by passing white noise through the circuit described in the ETSI document [40]. Then, the audio signal is passed through a pre-emphasis filter prior to FM modulation. Figures 5.1 to 5.8 show the PSDs of the various noise-free WM signal models and their corresponding PSDs when the SNR is -20 dB. We can see from these figures that the power of the WM signal concentrates within a small frequency band which is less than 200 kHz. Moreover, there are apparent peaks contained in the PSDs of the various WM signal models. Also, from these figures, it can be seen that for the same operating mode, the PSDs of the WM signal look almost the same as the PSDs of the WM signal passed through a fading channel. This is because the channel is a flat fading channel. A flat fading channel does not change the shape of the PSD of a signal [41]. As a result, we can perform spectrum sensing of the WM signal by detecting peaks of the estimated PSD corresponding to a 6 MHz DTV channel. For simplicity, we use the maximum peak of the estimated PSD as the decision statistic.

5.2 Wireless Microphone Detector

Let the received sampled signal $y[n]$ be described according to

$$y[n] = s[n] \otimes h[n] + w[n] \tag{5.2}$$

where $s[n]$ is the transmitted WM signal, $h[n]$ is channel impulse response and $w[n]$ is additive white Gaussian noise (AWGN) noise. We will further assume that $w[n]$ is zero-mean and has a variance of σ^2. The PSD of the signal $y[n]$ is estimated by [42]

$$S_y[l] = \frac{1}{(N-1)T_s}\frac{1}{M}\sum_{u=0}^{M-1}|Y[u,l]|^2 \tag{5.3}$$

where T_s is the sampling period, and

$$Y[u,l] = \sum_{k=0}^{N-1} y[u \cdot N + k]e^{-j2\pi lk/N} \tag{5.4}$$

which is the DFT of the non-overlapping sliding sampled signal [42]. The parameter N is the size of the DFT. Then, the test statistic to be used is given by

$$T = \max_{l} |S_y[l]|. \tag{5.5}$$

5.3 Probability of False Alarm

For hypothesis H_0, which corresponds to the presence of noise only, i.e., $y[n] = w[n]$. We know that $w[n]$ are independently and identically distributed (i.i.d.) Gaussian random variables with zero-mean and variance σ^2. It can be easily shown that $W[u,l],\ \ l = 0, 1, \ldots, N-1$ computed by (5.4) are circularly symmetric i.i.d. complex Gaussian random variables with zero-mean and variance $N\sigma^2$. Therefore, $|W[u,l]|,\ \ l = 0, 1, \ldots, N-1$ are i.i.d. Rayleigh distributed. Then, $S_w[l]$ computed by (5.3) are i.i.d. Gamma distributed random variables

$$S_w[l] \sim \Gamma(M, \frac{N\sigma^2}{(N-1)T_s}\frac{1}{M}). \tag{5.6}$$

From the Central Limit Theorem, when M is sufficiently large, $S_w[l]$ approaches that of a Gaussian distribution

$$\lim_{M\to\infty} S_w[l] \to N(M\theta, M\theta^2) \tag{5.7}$$

where $\theta = \frac{N\sigma^2}{(N-1)T_s}\frac{1}{M}$. Therefore, the cumulative distribution function of the test statistic for hypothesis H_0 is given by

$$F_T(x : H_0) = \left(\int_{-\infty}^{x} \frac{1}{\sqrt{2\pi M\theta^2}} e^{-\frac{(u-M\theta)^2}{2M\theta^2}} du\right)^N. \tag{5.8}$$

Then, for a particular P_{FA}, the corresponding threshold λ can be found by

$$P_{FA} = 1 - F_T(\lambda : H_0). \tag{5.9}$$

Finally, after some straightforward calculation, we have

$$\lambda = M\theta + \sqrt{M}\theta \cdot Q^{-1}(1 - (1 - P_{FA})^{1/N}) \tag{5.10}$$

where $Q^{-1}(\cdot)$ is the inverse function of the function

$$Q(x) = \int_x^{\infty} \frac{1}{\sqrt{2\pi}} e^{-\frac{1}{2}u^2} du. \tag{5.11}$$

5.4 Simulation Results

We use the WM signal models described in Section 5.1 to test the proposed spectrum sensing algorithm. Figures 5.9 and 5.11 show the operational curves of the six WM signal models provided in [38] when $P_{FA} = 0.1$ and $P_{FA} = 0.01$, respectively, and a sensing of 10 ms is used. For the worse case, the required SNR for WM detector to achieve 0.1 of P_{MD} is about -24.8 dB and -23.8 dB for $P_{FA} = 0.1$ and $P_{FA} = 0.01$, respectively. We can see that the detection performance is better when the FM deviation factor is smaller. It is because the smaller the FM deviation factor, the more concentrated is the signal power in the frequency domain. We can also see that the single-path Rayleigh fading channel does not have a significant effect on the detection performance. Figures 5.10 and 5.12 show the performance curves for the WM device when operated in the Soft Speaker and the Loud Speaker Modes as described in [38]. However, here colored noise has been used as a voice source [40] instead of tone signals. We can see that when we use colored noise as a voice source, the detection performances are similar for the four cases. The required SNR for WM detector to achieve a $P_{MD} = 0.1$ is about -27 dB and -26 dB for $P_{FA} = 0.1$ and $P_{FA} = 0.01$, respectively. Compared with the eigenvalue-based detector described in [9], the required SNR for an eigenvalue-based detector to achieve $P_{MD} = 0.1$ with respect to $P_{FA} = 0.1$ using a sensing time of 9.3 ms is -20 dB. Therefore, the proposed WM detector developed in this study provides a significant performance improvement. Furthermore, the complexity of the proposed WM detector is much smaller than the complexity of the eigenvalue-based detector.

5.5 Conclusions

A simple spectrum sensor for wireless microphone has been described in this chapter. The presented WM spectrum sensor uses the maximum peak of the estimated PSD of the received signal. Computer simulations show that the the required SNR for the proposed spectrum sensor to achieve $P_{MD} = 0.1$ with respect to $P_{FA} = 0.1$ using a sensing time of 10 ms is -24.8 dB. Thus the WM spectrum sensor performs very well and has a very low complexity making it attractive for use in a variety of practical applications.

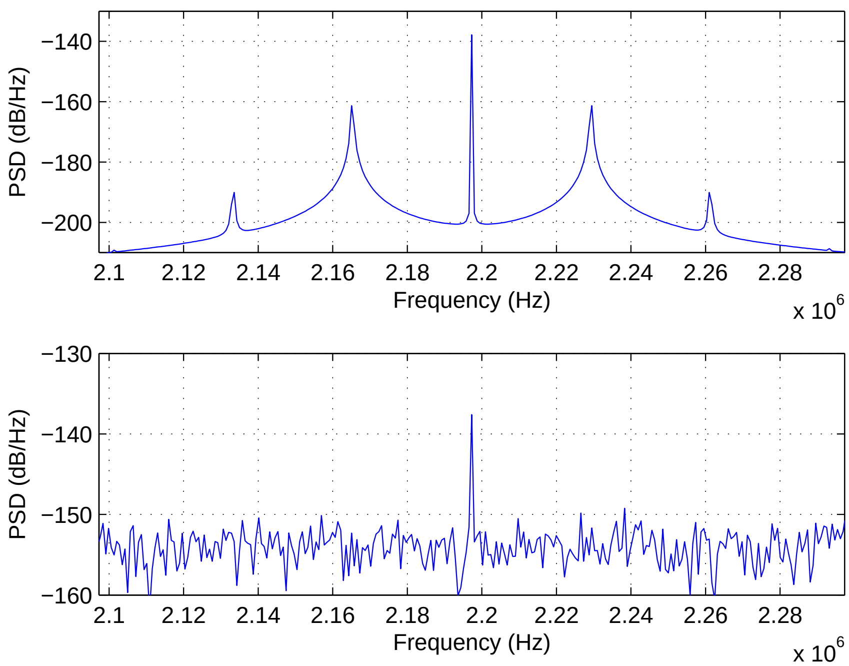

Figure 5.1: PSD of the WM signal and PSD of the WM signal plus AWGN (SNR=-20 dB), Outdoor, LOS, Silence.

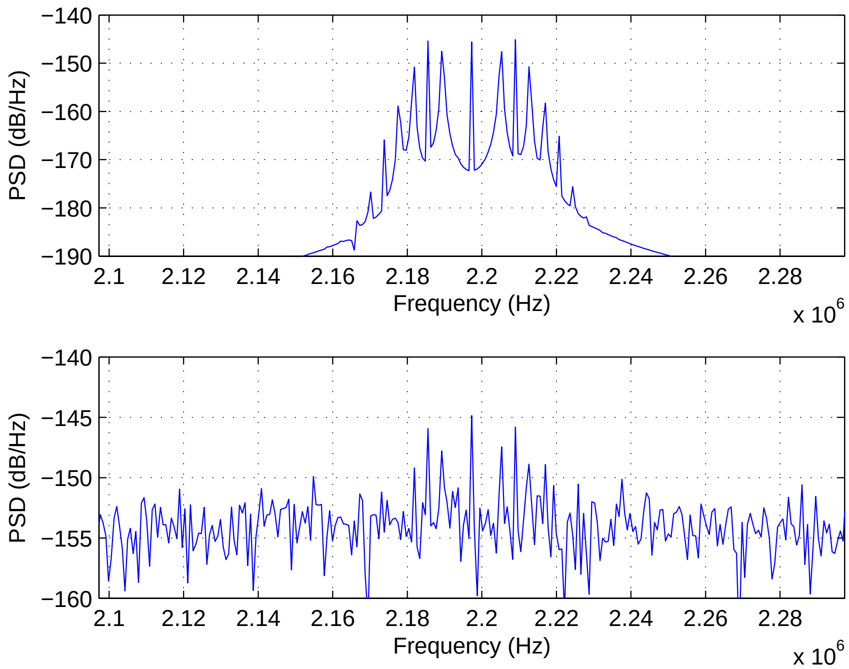

Figure 5.2: PSD of the WM signal and PSD of the WM signal plus AWGN (SNR=-20 dB), Outdoor, LOS, Soft Speaker.

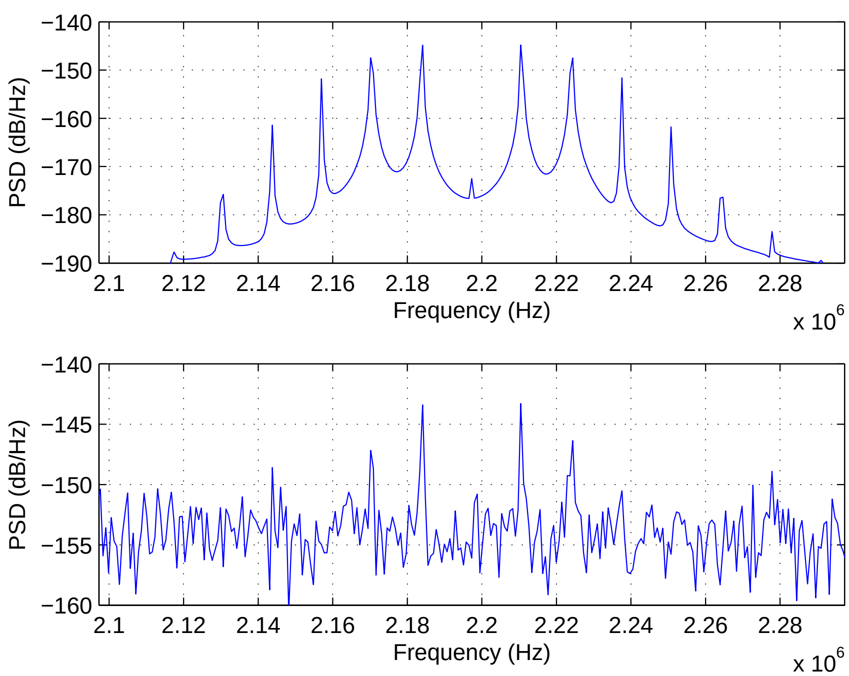

Figure 5.3: PSD of the WM signal and PSD of the WM signal plus AWGN (SNR=-20 dB), Outdoor, LOS, Loud Speaker.

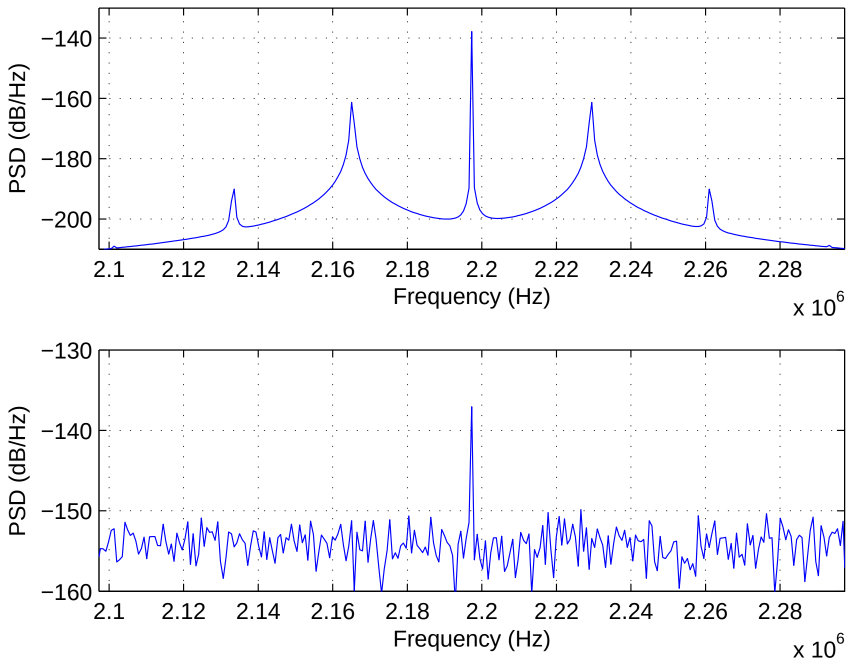

Figure 5.4: PSD of the WM signal and PSD of the WM signal plus AWGN (SNR=-20 dB), Indoor, Rayleigh Faded, Silence.

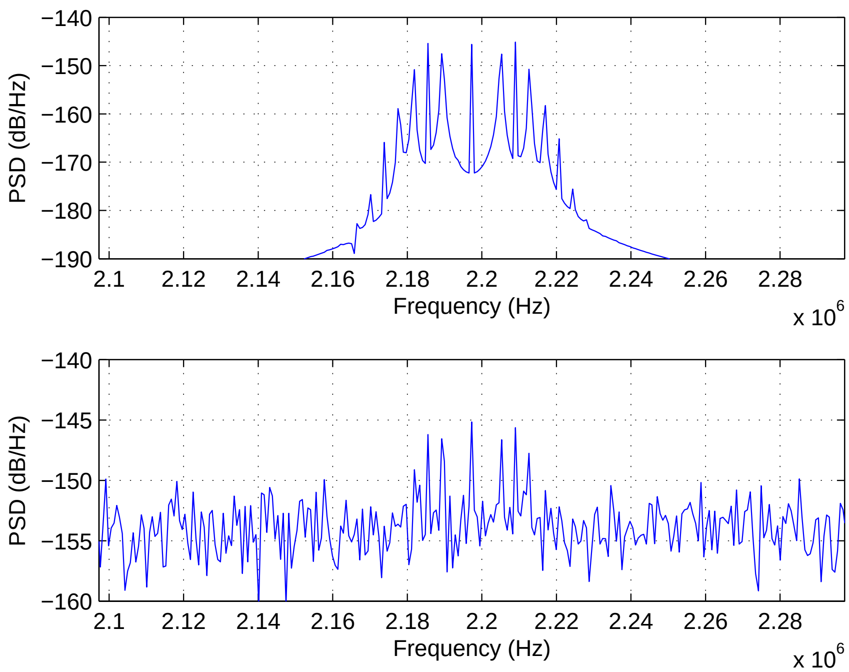

Figure 5.5: PSD of the WM signal and PSD of the WM signal plus AWGN (SNR=-20 dB), Indoor, Rayleigh Faded, Soft Speaker.

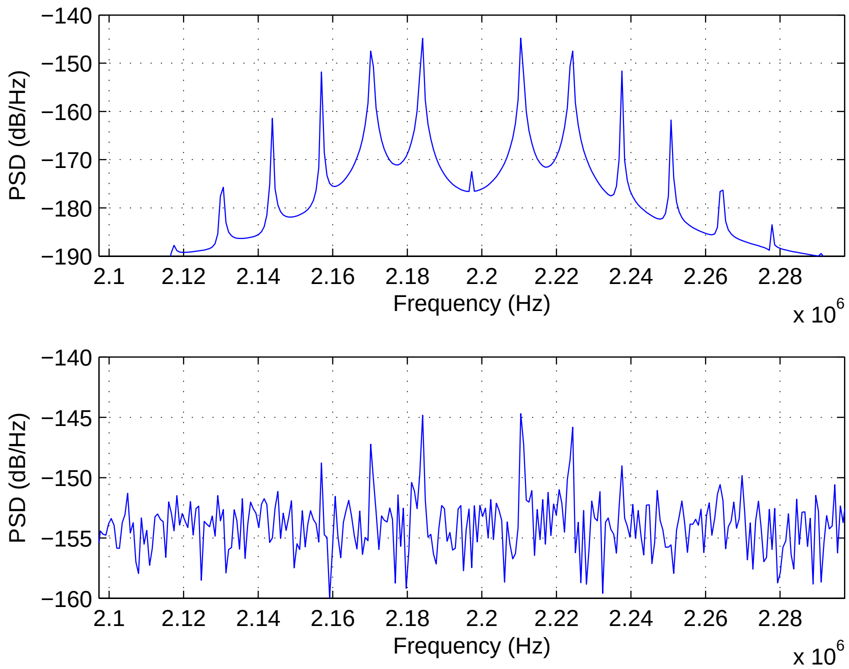

Figure 5.6: PSD of the WM signal and PSD of the WM signal plus AWGN (SNR=-20 dB), Indoor, Rayleigh Faded, Loud Speaker.

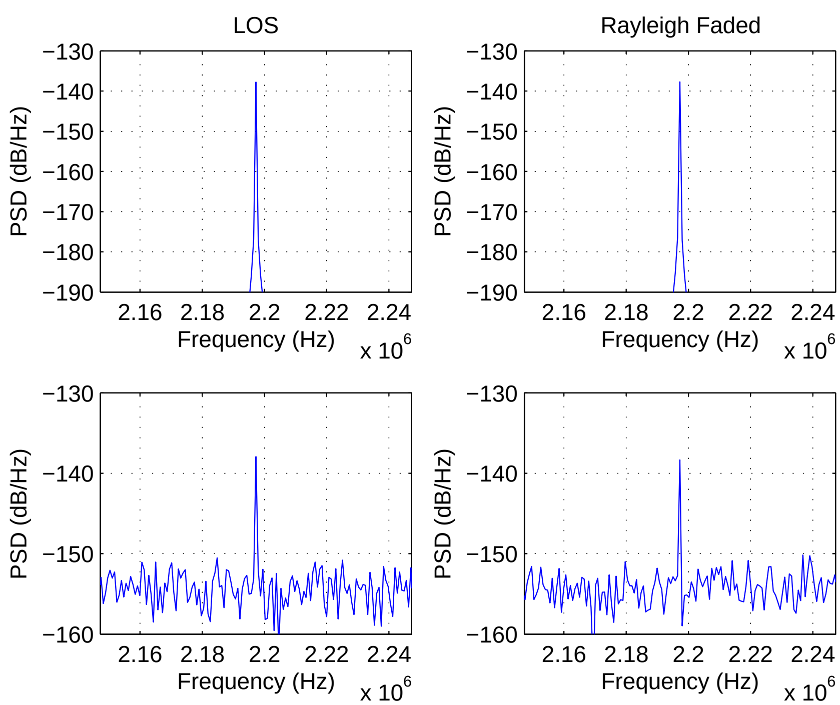

Figure 5.7: PSD of the WM signal and PSD of the WM signal plus AWGN (SNR=-20 dB) using colored noise as voice source, Soft Speaker.

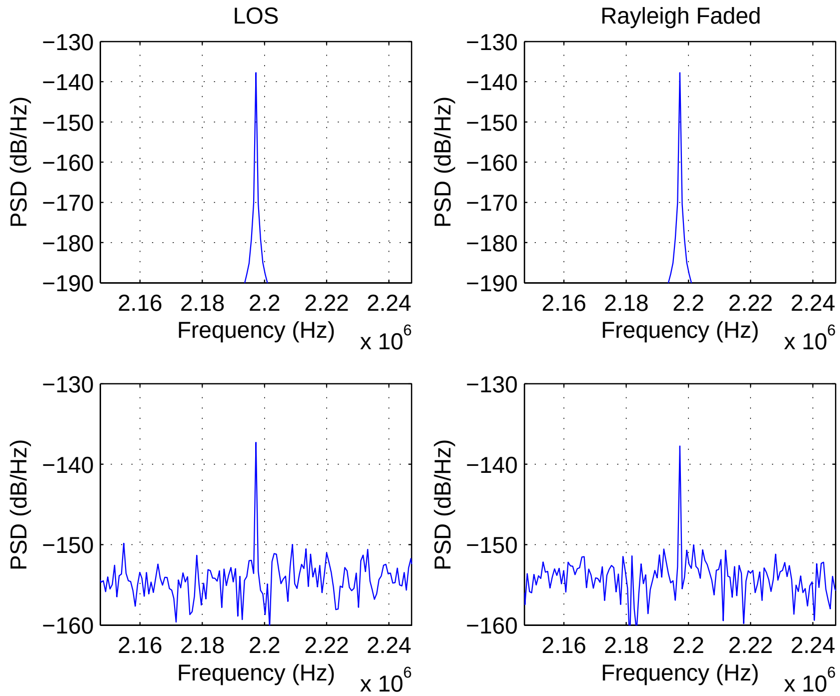

Figure 5.8: PSDs of the WM signal and the WM signal plus AWGN (SNR=-20 dB)using colored noise as the voice source, Loud Speaker.

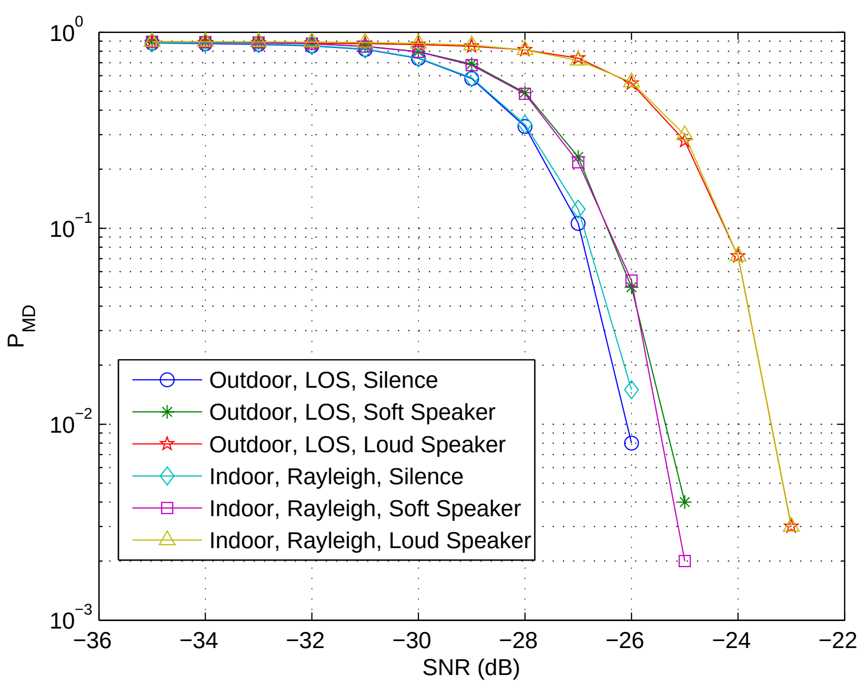

Figure 5.9: Spectrum sensing performance of the WM detector using a tone signal as the voice source, $P_{FA} = 0.1$ and sensing time=10 ms.

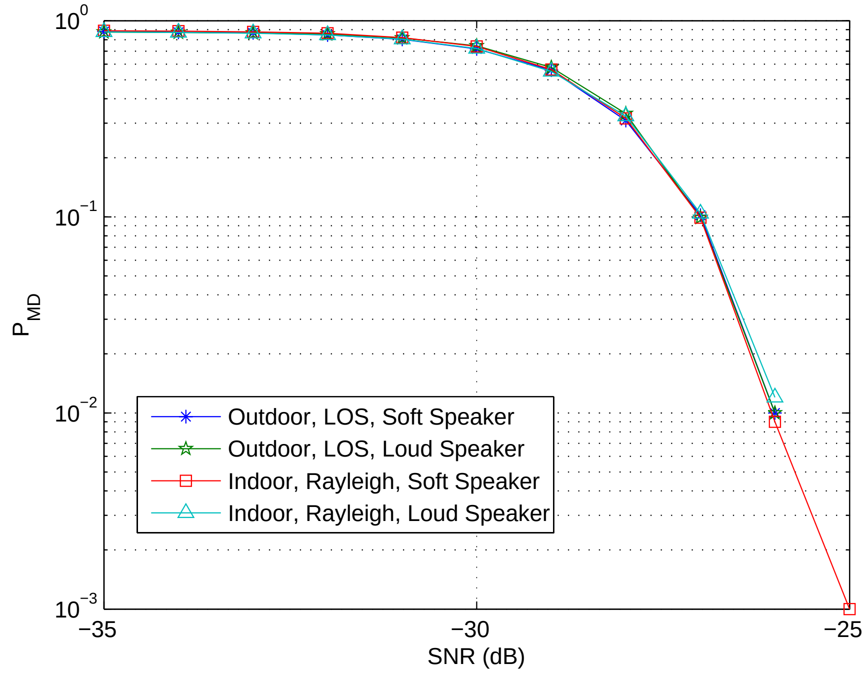

Figure 5.10: Spectrum sensing performance of the WM detector using colored noise as the voice source, $P_{FA} = 0.1$ and sensing time=10 ms.

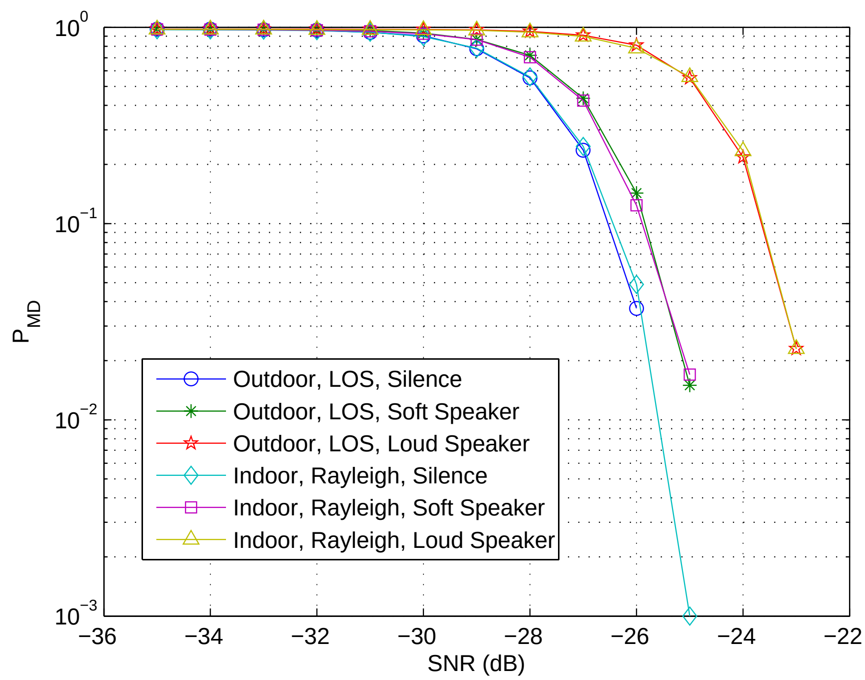

Figure 5.11: Spectrum sensing performance of the WM detector using a tone signal as the voice source, $P_{FA} = 0.01$ and sensing time=10 ms.

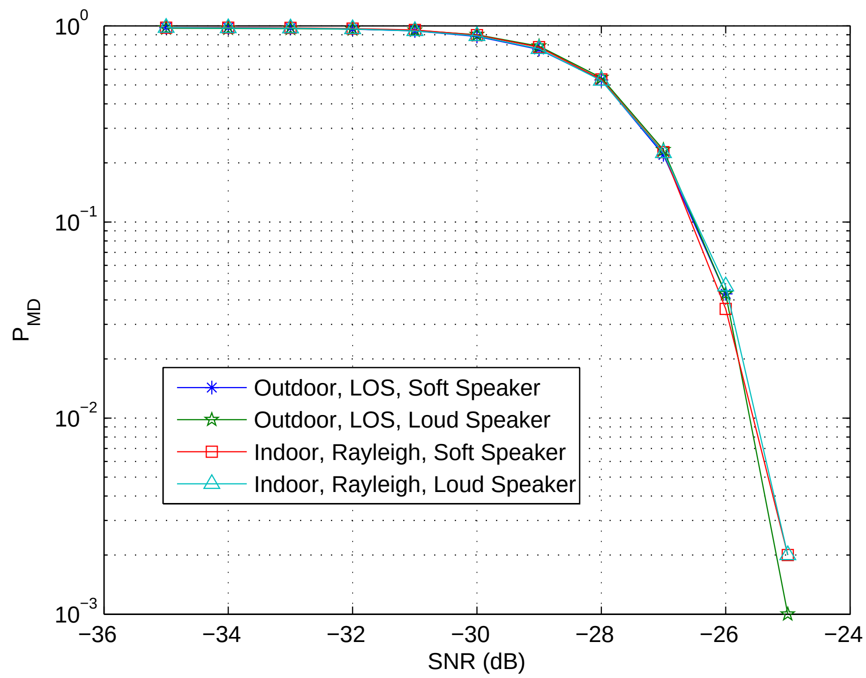

Figure 5.12: Spectrum sensing performance of the WM detector using colored noise as the voice source, $P_{FA} = 0.01$ and sensing time=10 ms.

Chapter 6

Hardware Implementation

In this chapter, we describe the hardware implementation of the cyclostationarity-based spectrum sensing algorithm for the ATSC DTV signals presented in Chapter 2. We utilize two software packages, AccelDSP and System Generator, which are products of Xilinx, Inc. The AccelDSP software can transfer high level Matlab language code to low level Register Transfer Language (RTL) code including VHDL and Verilog languages. The transferred RTL languages can either be implemented directly in a Field Programmable Gate Array (FPGA), or be converted into a block structure which can be used in the System Generator software package. Therefore, the AccelDSP software package is used to generate the required blocks for the cyclostationarity-based spectrum sensing algorithm. Then, the blocks provided by the System Generator, as well as the blocks generated by the AccelDSP, are used to construct the spectrum sensor. Once the spectrum sensor has been properly constructed, a hardware co-simulation block is then generated by the System Generator. The hardware co-simulation block is used to implement the spectrum sensor within the FPGA platform. Details of the AccelDSP software can be found in [43].

6.1 Introduction to the Xilinx AccelDSP and System Generator Software

As mentioned before, AccelDSP can generate a block having a specific function, and this block can subsequently be used in the System Generator. It is intuitive to think of this block as being a user-defined Matlab function. Moreover, a function call in Matlab corresponds to a clock cycle in the circuit, and indeed, this is the case in AccelDSP. Therefore, in order to begin the implementation of hardware operations, one needs to create a function m-file and a script m-file which calls the m-function. In the script m-file, any Matlab function can be used. Typically, data curves are plotted to determine if the designed function works correctly. However, in the function m-file, only limited Matlab functions are supported by AccelDSP. In this chapter, we will use a narrow bandpass IIR filter design to illustrate how to use the AccelDSP software. After we complete development of both the script m-file and the function m-file in the Matlab programming environment, we can launch the AccelDSP software as shown in Fig. 6.1.

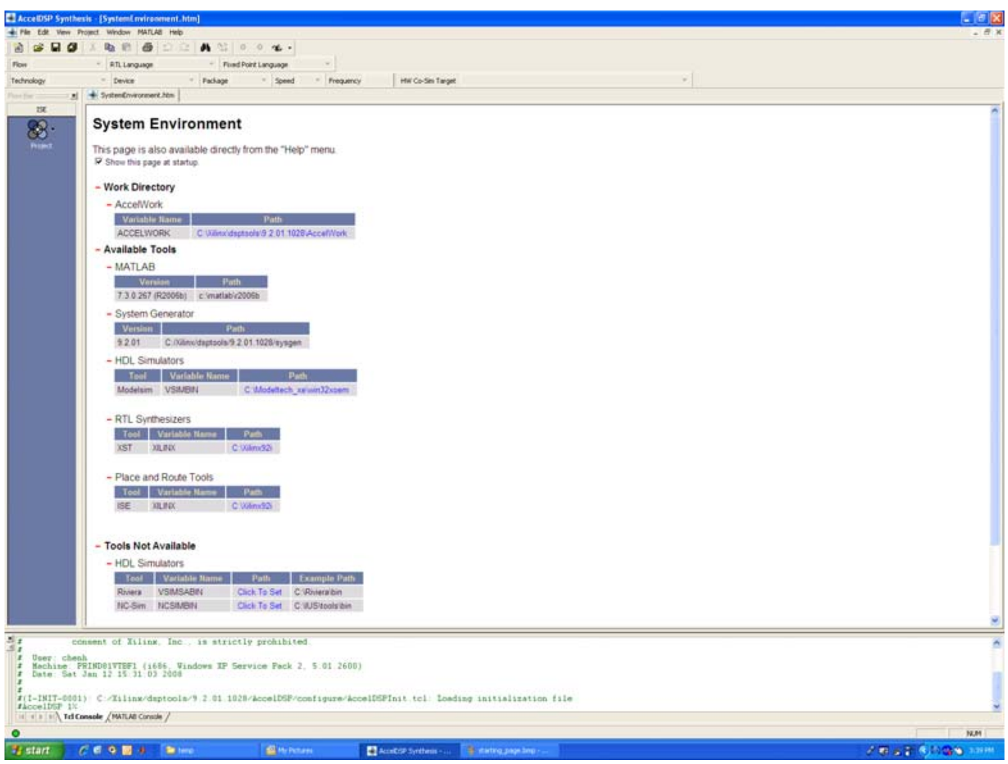

Figure 6.1: Starting page of the AccelDSP software.

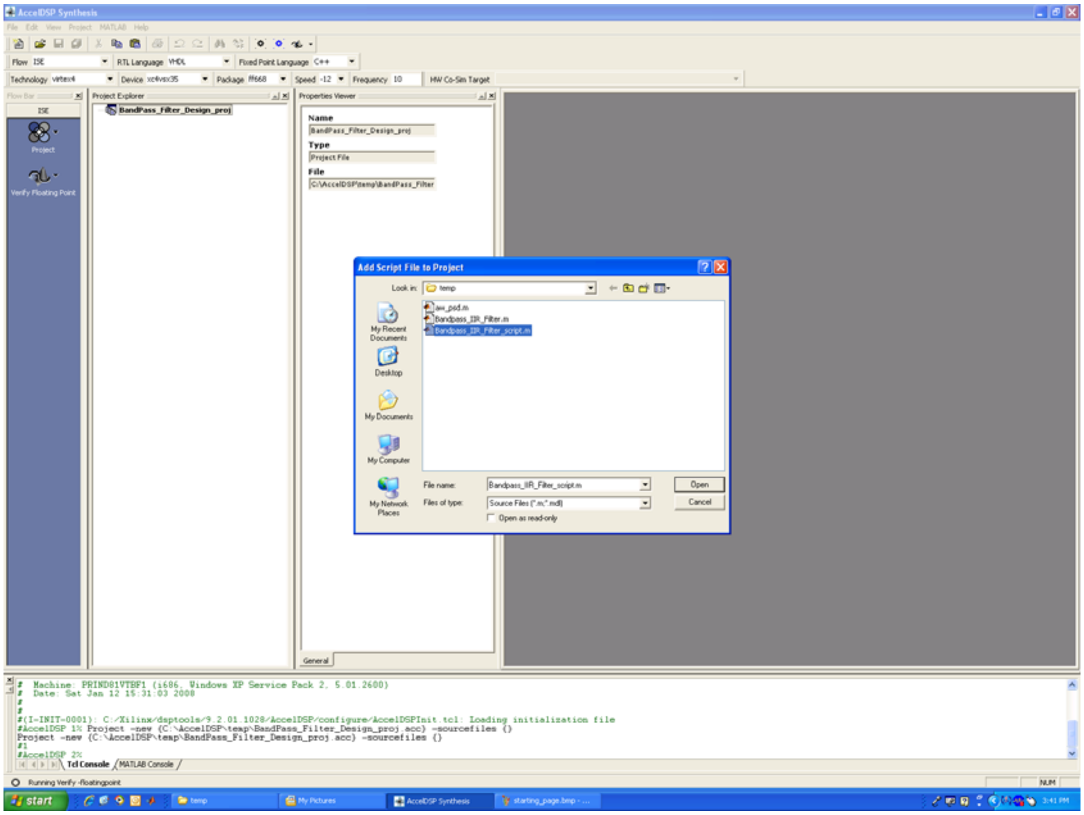

Figure 6.2: Verification of floating-point simulation result for the designed filter.

By clicking the **Project** icon in the top left side, we can create a new AccelDSP project called Bandpass_Filter_Design_proj. Then, click the **Verify Floating Point** bottom and select the script m-file to simulate the filter design by using floating point variables as shown in Fig. 6.2. In this step, AccelDSP will call the Matlab software package to verify the consistency of the program, and then perform the floating point simulation.

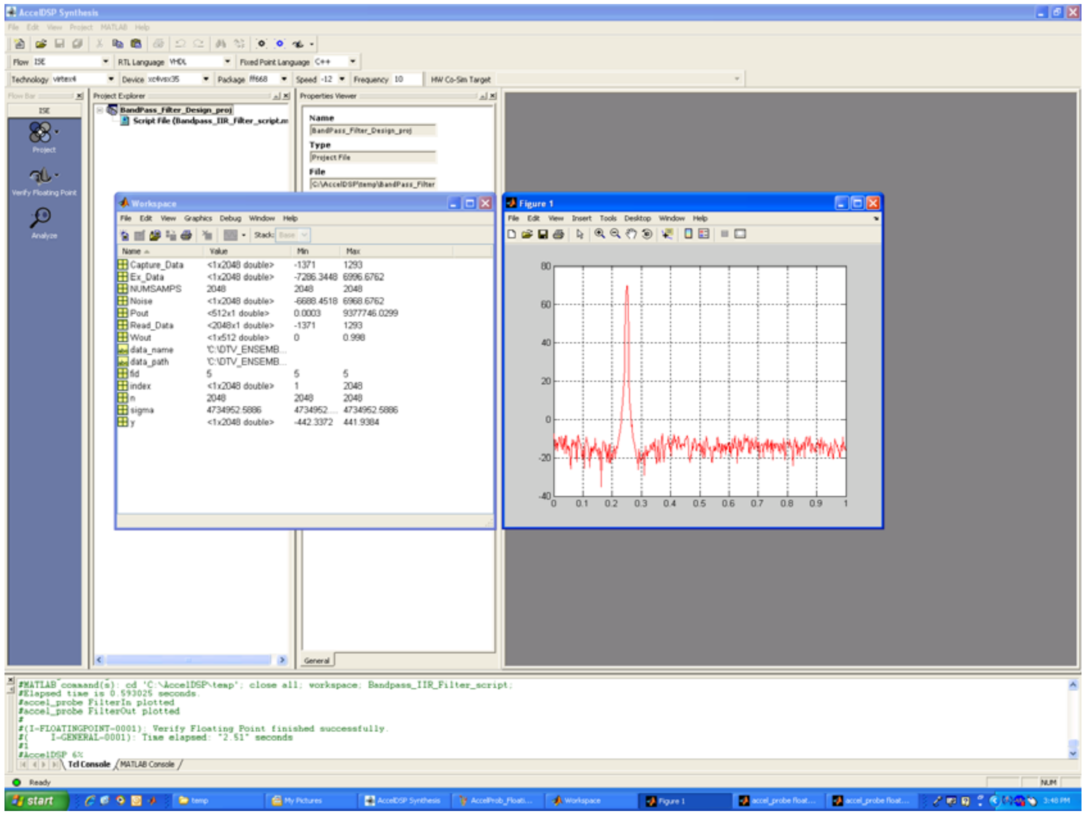

Figure 6.3: Spectrum of the designed filter using floating-point arithmetic.

After the **Verify Floating Point** step is finished, a Matlab workspace and various curves plotted in response to the script m-file will appear as depicted in Fig. 6.3. In the Matlab workspace, the dimension, maximum and minimum values of each variable are listed, as shown in Fig. 6.3. This information is very useful in deciding the word lengths and fractional lengths of the variables that will be used in the fixed-point design. From the figures illustrating the bandpass filter behavior, it can be determined if the designed filter posseses the required properties.

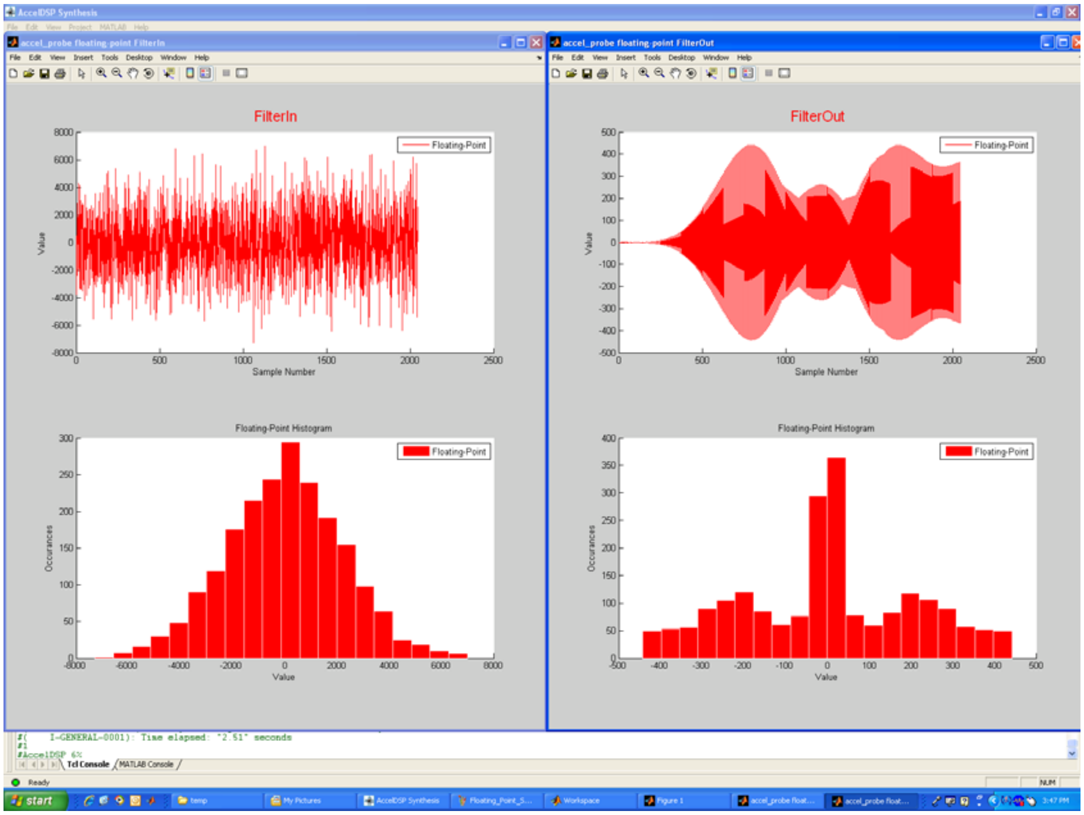

Figure 6.4: Statistics of the floating-point input and output data.

AccelDSP provides a very useful function, or tool, called Accel Prob that displays the statistics of any variable involved in the designed Matlab function for both floating-point and fixed-point results. In particular, the displayed statistics are the histograms of the original signal values, and their floating representations are shown in Fig. 6.4. This function provides guidance as to how to assign required word lengths and fractional lengths of the variables that are to be used in the fixed-point design. Take our bandpass filter design for example, we would like to know the statistics of the data fed into the filter and the data outputted from the filter. By examining the statistics of these two variables, we can determine if the word lengths and fractional lengths are set correctly, i.e., the quantization error is tolerable and the complexity is acceptable.

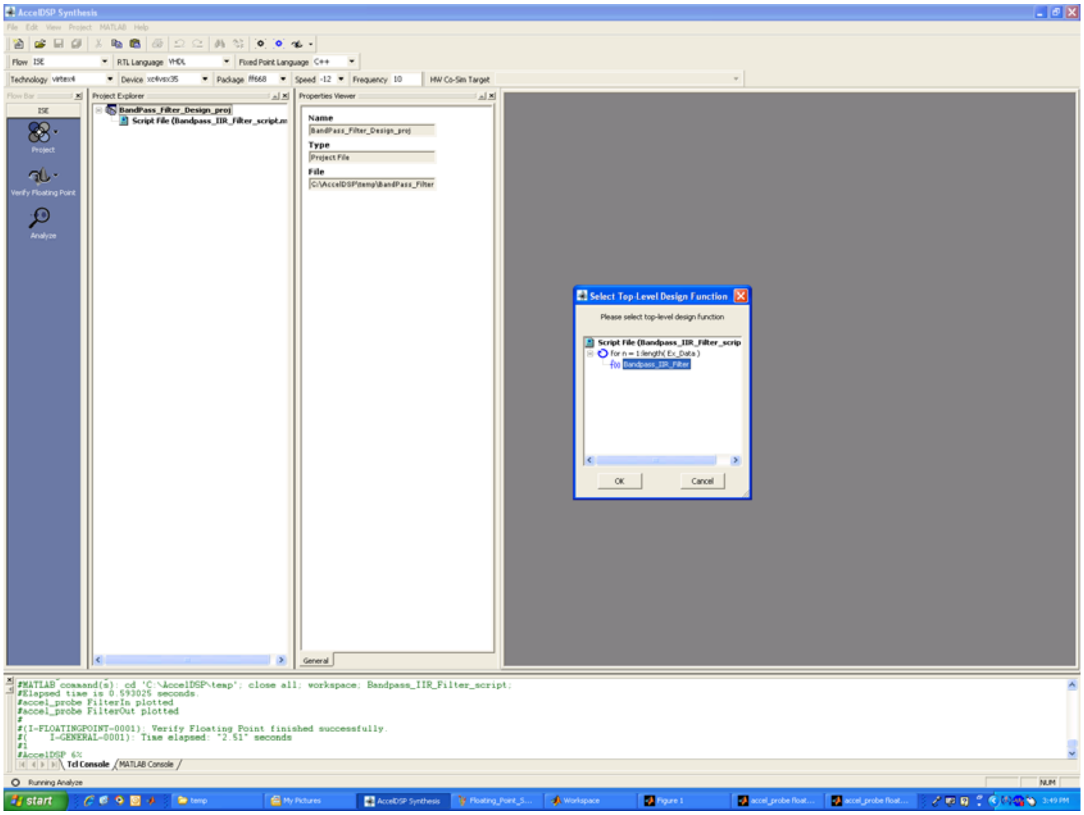

Figure 6.5: Analysis of Matlab code and creation of an in-memory model.

After the **Verify Floating Point** step is complete. An **Analyze** icon is displayed as illustrated in Fig. 6.5. In this step, AccelDSP will create an in-memory model of the design. In later steps, design directives may be added as needed to this in-memory model to guide AccelDSP toward finding the best hardware architecture for the designed filter, i.e., function.

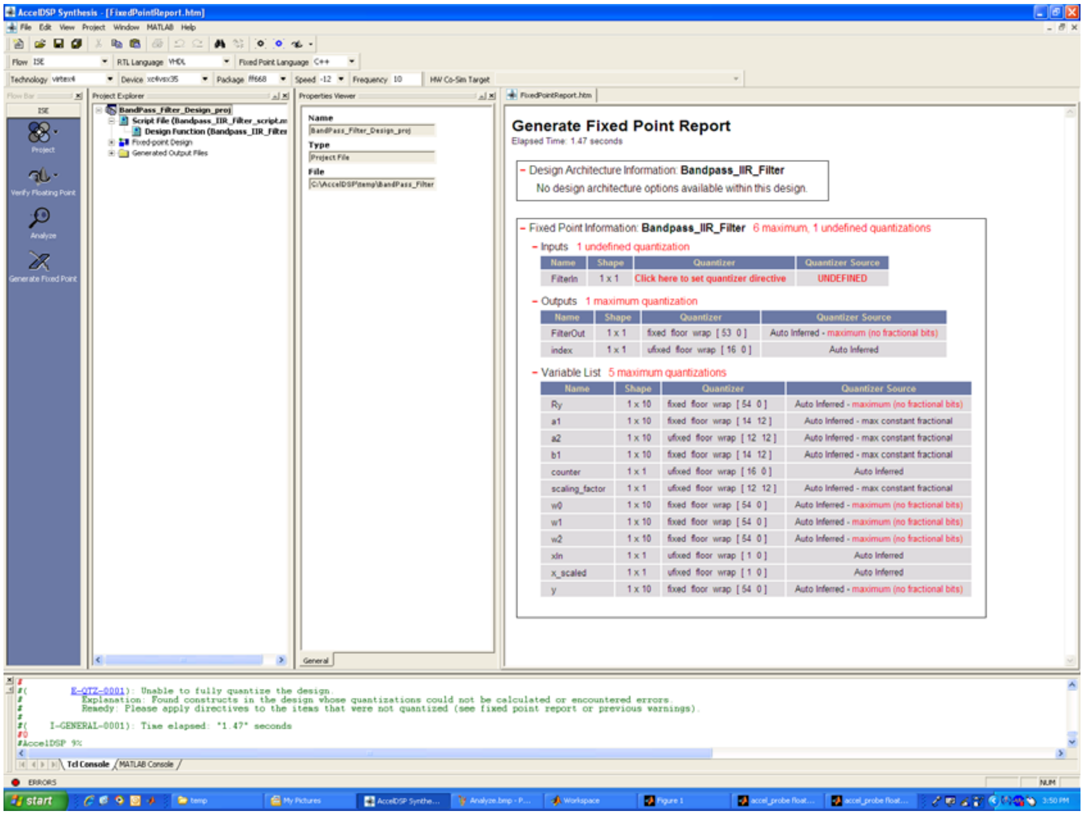

Figure 6.6: Determination of the fixed-point number of bits for the variables used by AccelDSP.

Then, by clicking the **Generate Fixed Point**, AccelDSP will assign word lengths and fractional lengths for each variable. Figure 6.6 illustrates the fixed-point report. Sometimes, the AccelDSP cannot determine the word lengths of some variables, and occasionally, the word lengths and fractional lengths assigned by the AccelDSP software package are not suitable. Therefore, it is more often the case wherein the word lengths and fractional lengths must be provided manually by the designer.

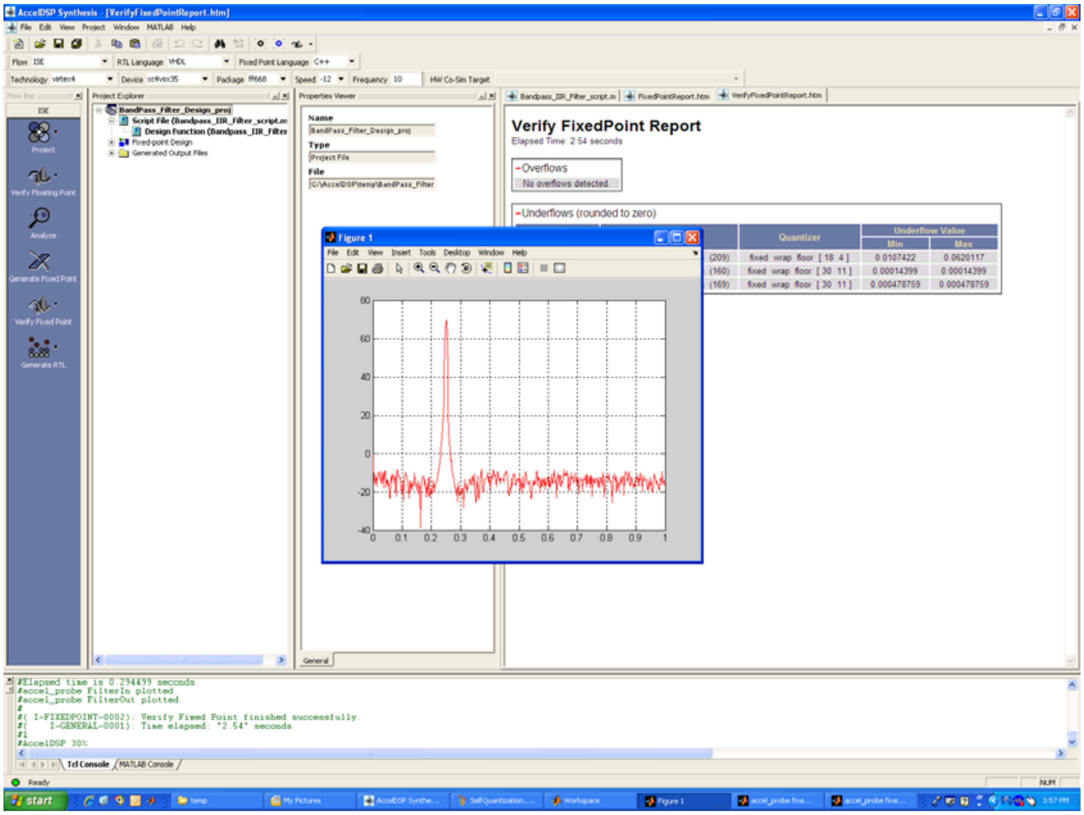

Figure 6.7: Resulting fixed-point spectrum of the designed bandpass filter.

After the word lengths and fractional lengths of all variables have been adjusted, the **Verify Fixed Point** step is to be executed. After this step is complete, the results of the fixed-point simulation are displayed, as shown in Fig. 6.7. By comparing the figures of floating-point and fixed-point simulation results, the designer can roughly identify if the word lengths and fractional lengths have been properly assigned.

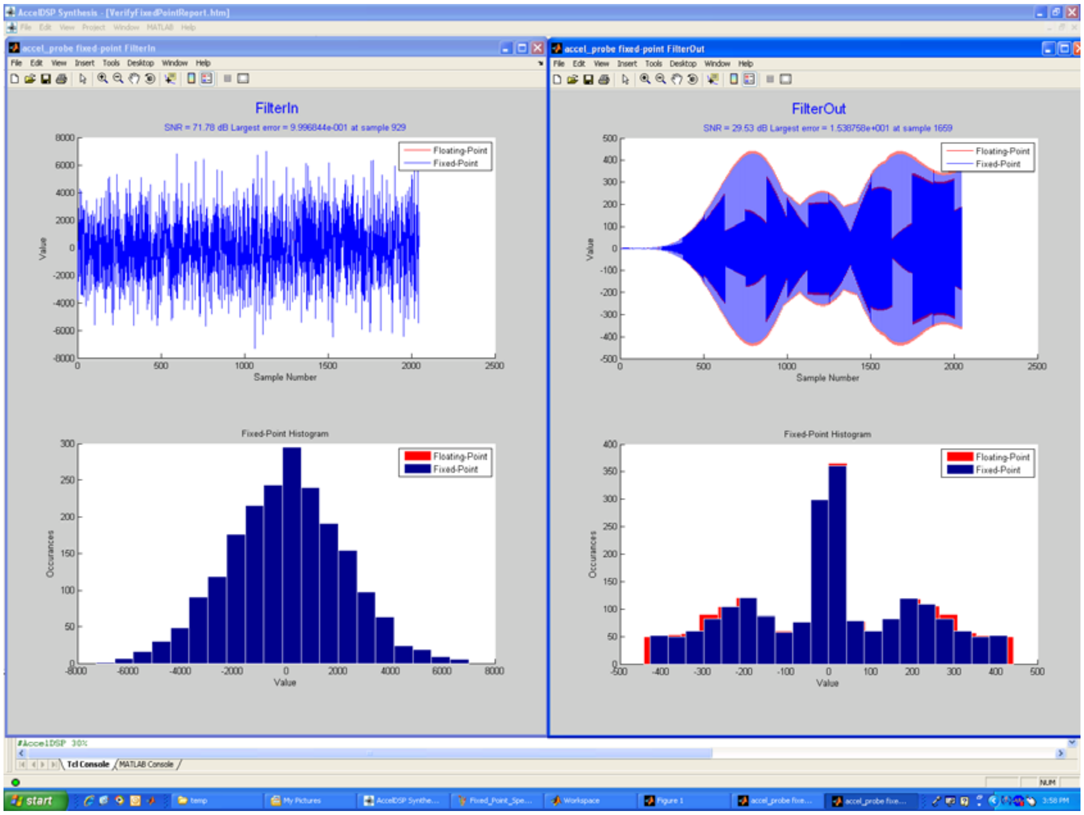

Figure 6.8: Statistics of the fixed-point input and output data.

In order to know precisely if the assigned word lengths and fractional lengths are proper, the fixed-point statistics of the selected data need to be determined and evaluated. As shown in Fig. 6.8, the upper two plots show the exact values of the original input and output samples for both floating-point and fixed-point. In these plots the floating-point and fixed-point results are superimposed on top of each other. The lower two plots show the histograms of the input and output samples for both the floating-point and the fixed-point realizations. In addition, a signal-to-quantization-noise ratio is calculated. Based on these statistics, we can adjust the word length and fractional length of each variable on an iterative basis, until the fixed-point result is as close to the floating-point result as desired, and the overall computational complexity is affordable in the context of the target implementation.

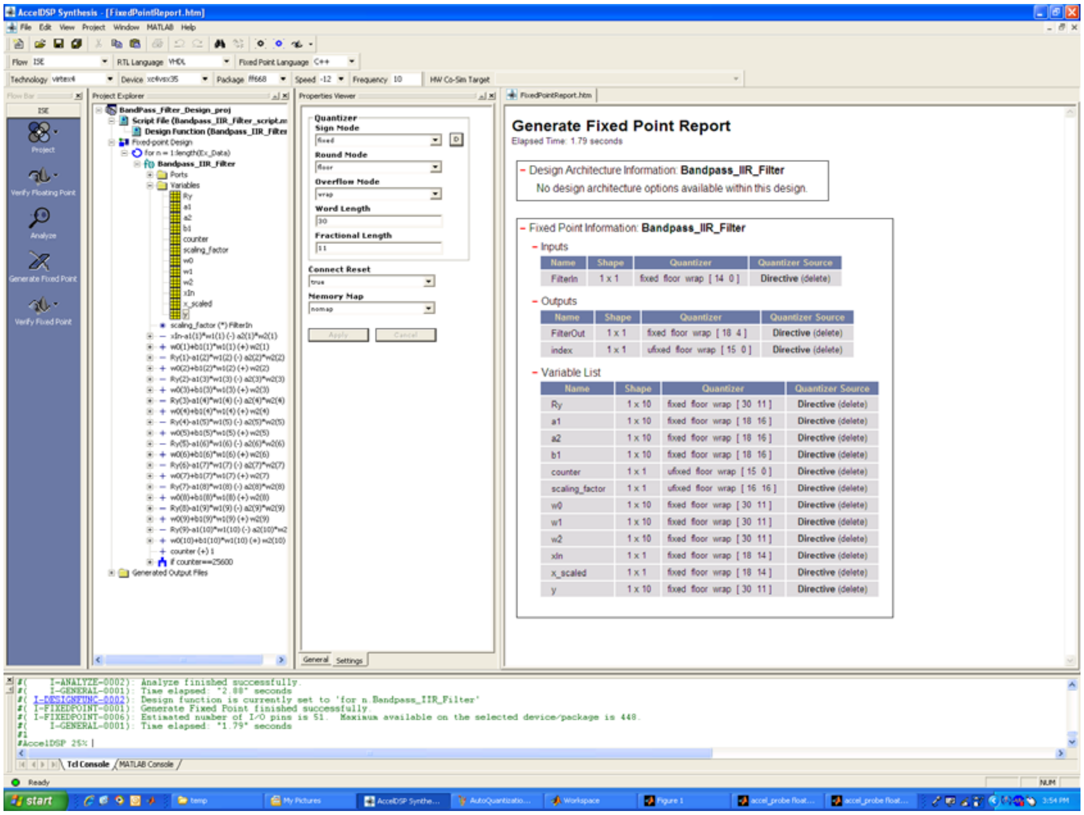

Figure 6.9: Final adjustment of the number of bits used for fixed-point quantities.

Figure 6.9 shows the word lengths and fractional lengths of the variables after adjustment.

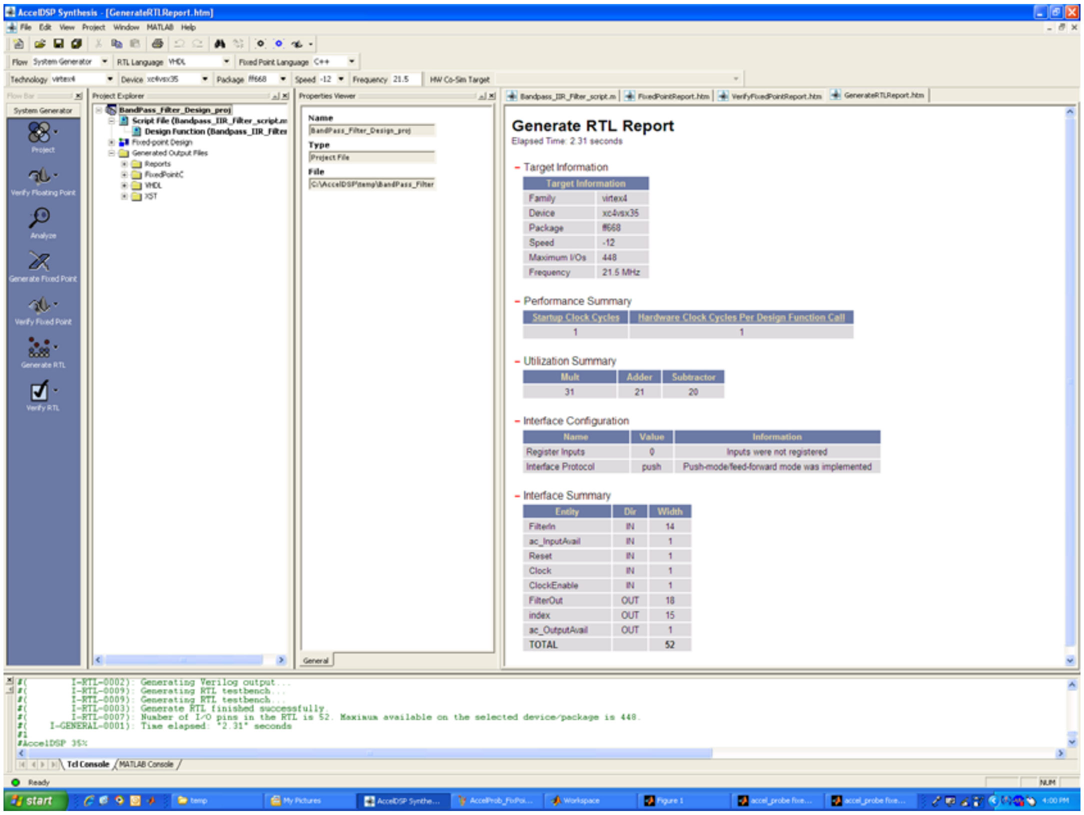

Figure 6.10: Generation of Register Transfer Language constructs.

After the **Verify Fixed Point** step is finished, by clicking the **Generate RTL** icon, the AccelDSP software package will generate both VHDL and Verilog codes. After the **Generate RTL** step is complete, a Generate RTL report is shown. In this report, the number of multipliers, adders, and subtractors used are listed. In the Performance Summary section, the item Startup Clock Cycles is set equal to one indicating that there is one hardware clock cycle delay for this particular design. When the Hardware Clock Cycles Per Design Function Call is set equal to one, this indicates that the design requires one hardware clock cycle for every function call. In AccelSDP, the designer must be sure to adjust the program code so that the Hardware Clock Cycles Per Design Function Call equals one. This is necessary because for every function call there must be some data fed into the function and some data outputted from the function.

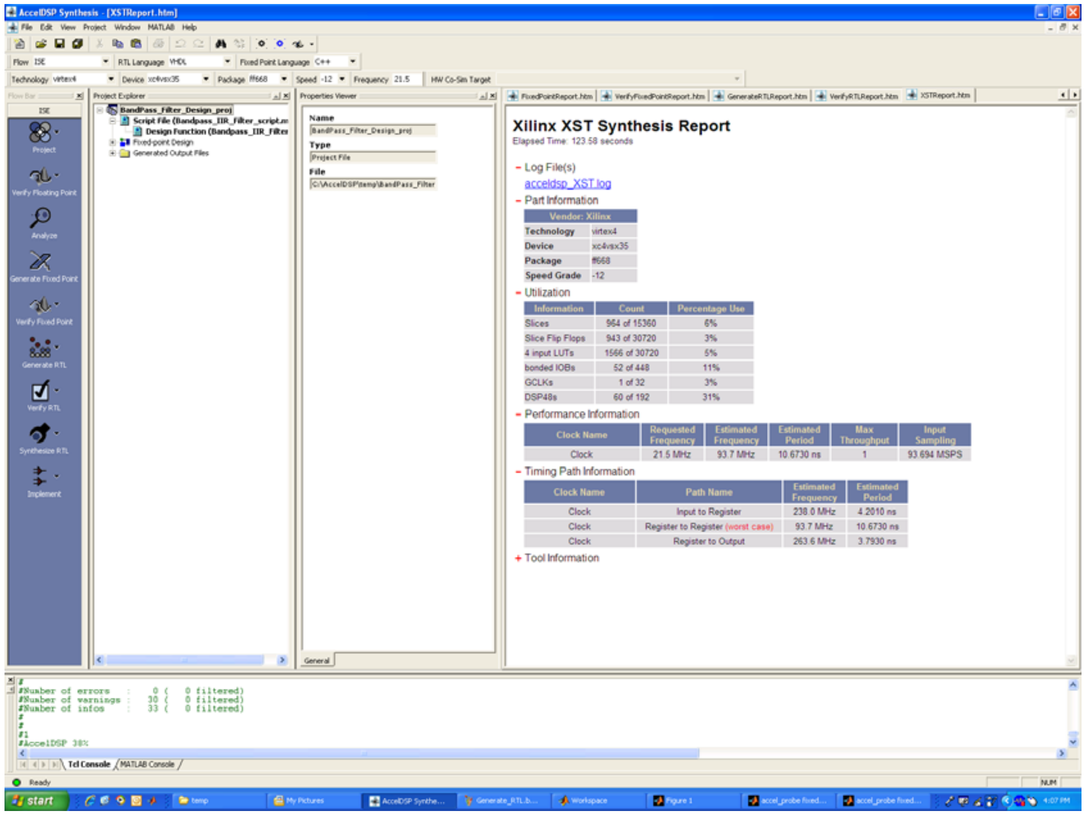

Figure 6.11: Synthesis of the Register Transfer Language constructs.

After the **Generate RTL** step, the designer has two choices. There is a Flow selection in the top left side. If the designer chooses ISE, a **Synthesize RTL** icon will appear. By performing this step, a Synthesis Report is generated. This report provides information about the resource utilization of this design, as well as a performance summary including the maximum operating frequency and the timing path summary.

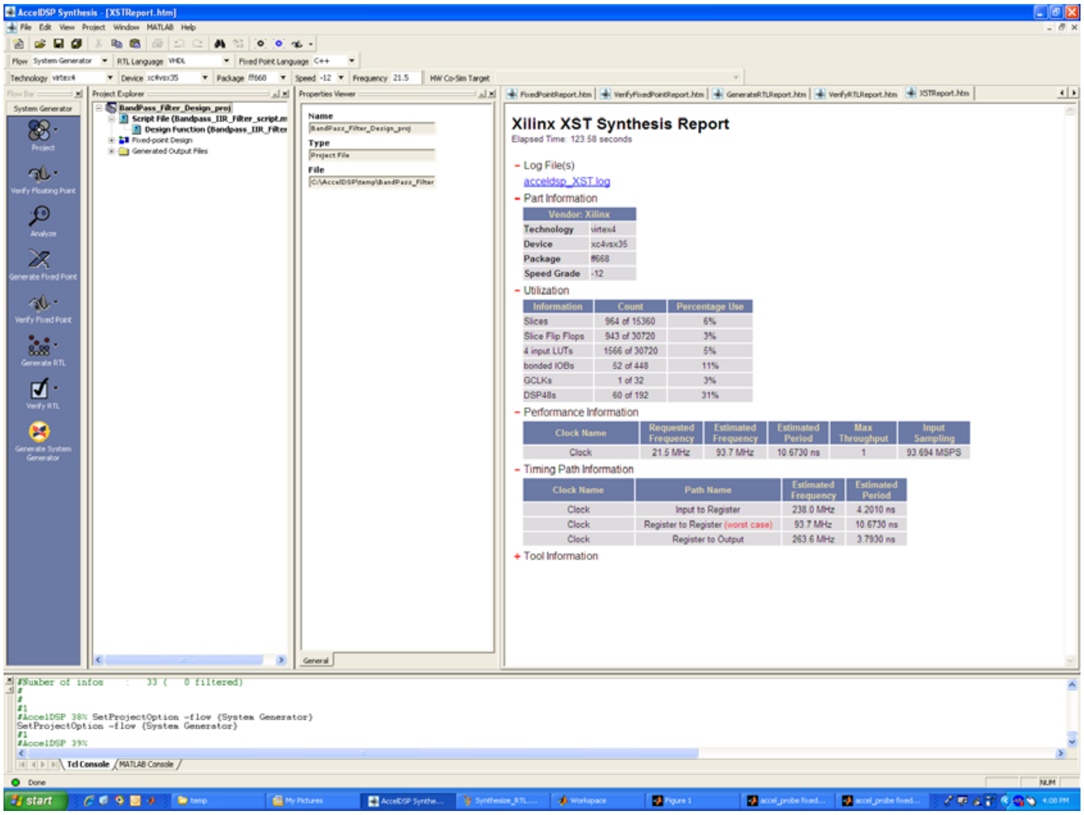

Figure 6.12: Creation of the system generator block.

If the designer chooses the Flow selection to be the System Generator, a **Generate System Generator** icon will be shown. By performing this step, AccelDSP will create a system generator block corresponding to the designed bandpass filter function which can be used in conjunction with the System Generator software.

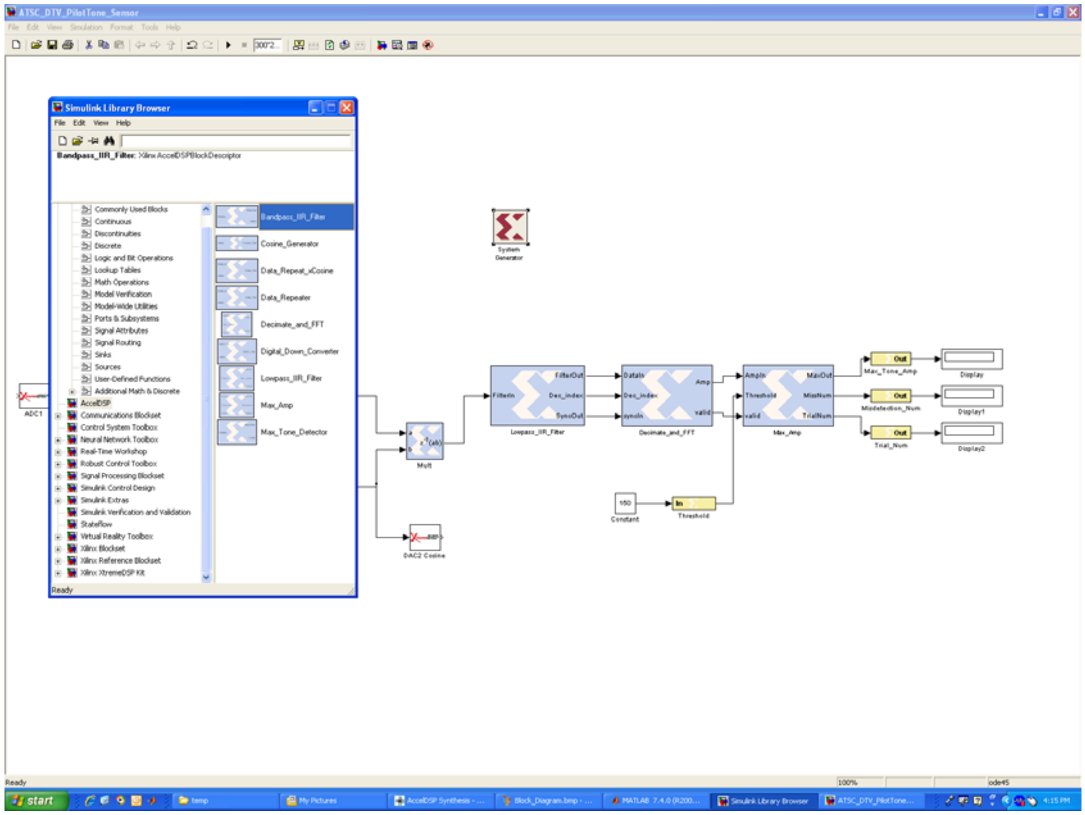

Figure 6.13: Simulink Library Browser.

After the **Generate System Generator** step is complete, a system generator block called BandPass_IIR_Filter will appear in the Simulink Library Browser as shown in Fig. 6.13.

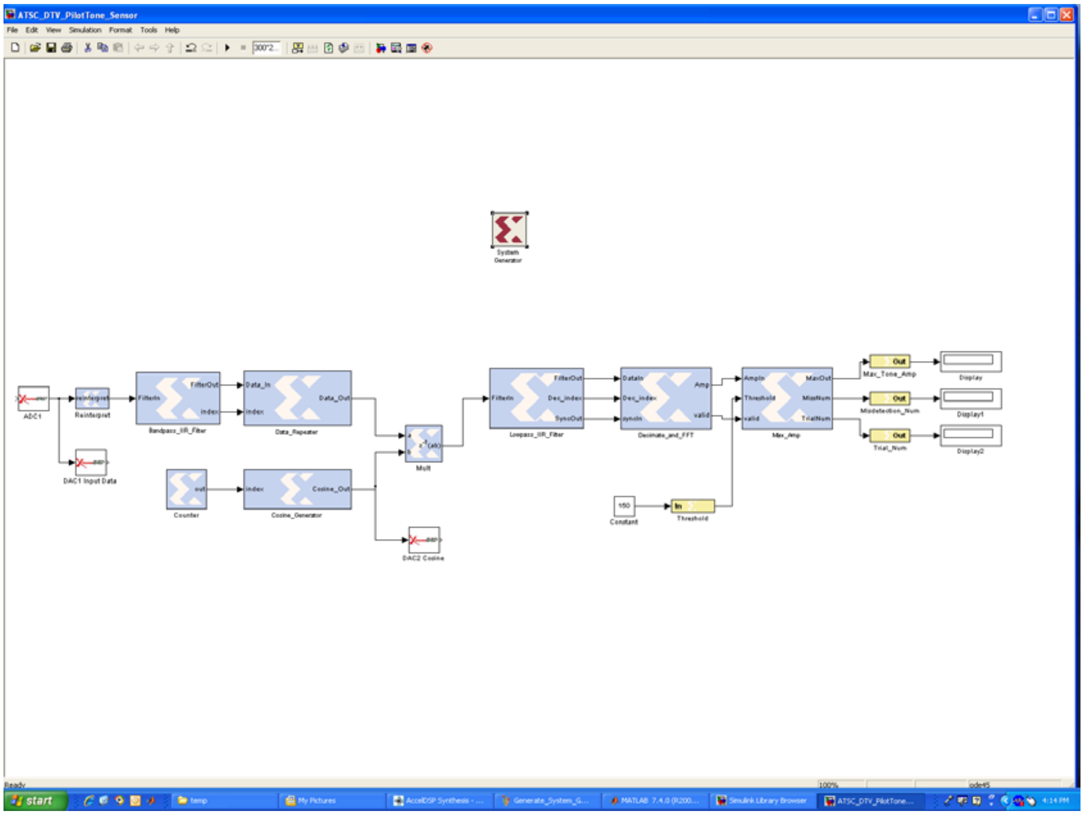

Figure 6.14: Block diagram of the designed spectrum sensor algorithm.

The overall block diagram of the cyclostationarity-based spectrum sensor for ATSC DTV signals is shown in Fig. 6.14. The blocks in Fig. 6.14 had been either generated by the AccelDSP software package, or provided by the System Generator software package.

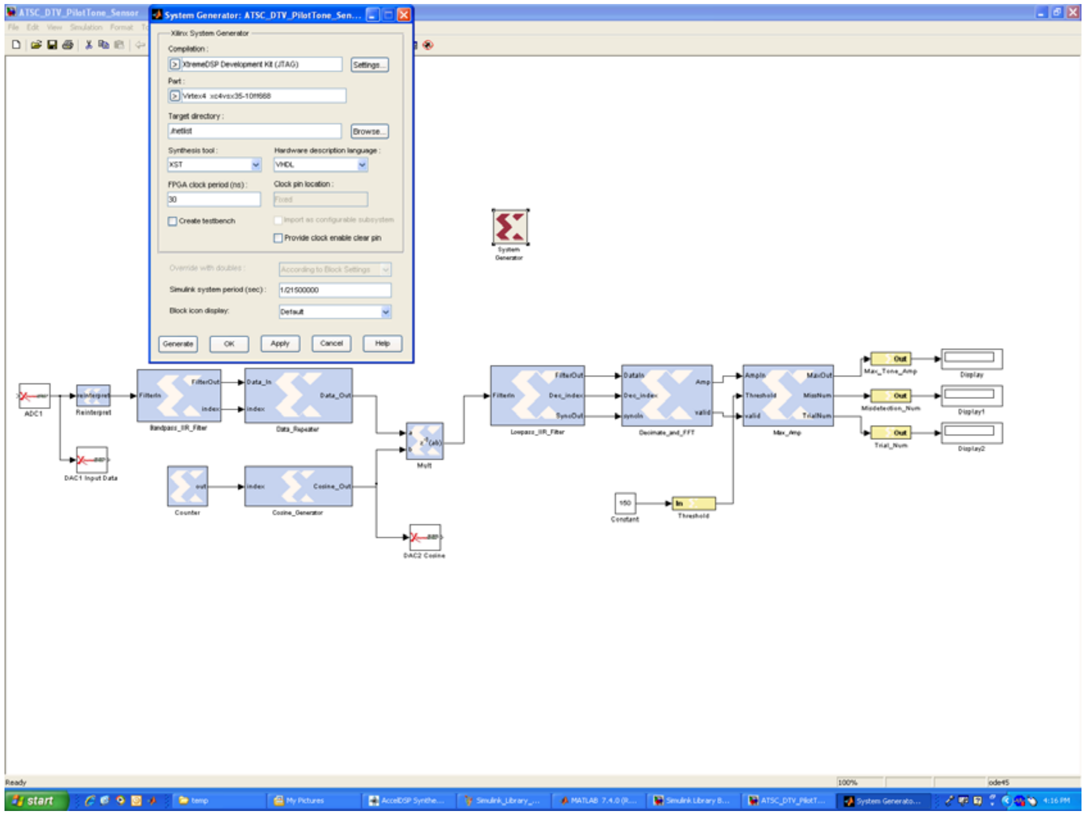

Figure 6.15: System Generator blocks.

By clicking the System Generator icon located at the top of the block diagram, the designer can set up the required parameters. Subsequently, a hardware co-simulation block will be generated as shown in Fig. 6.16.

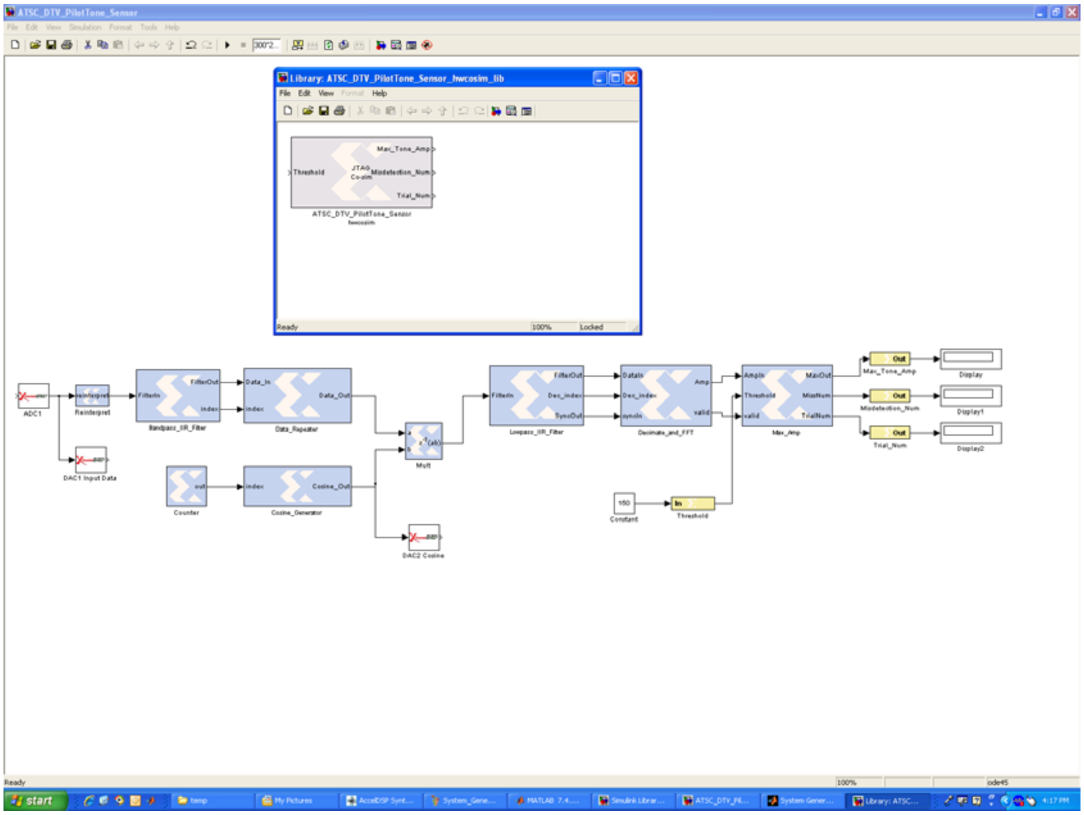

Figure 6.16: Generation of the hardware co-simulation block.

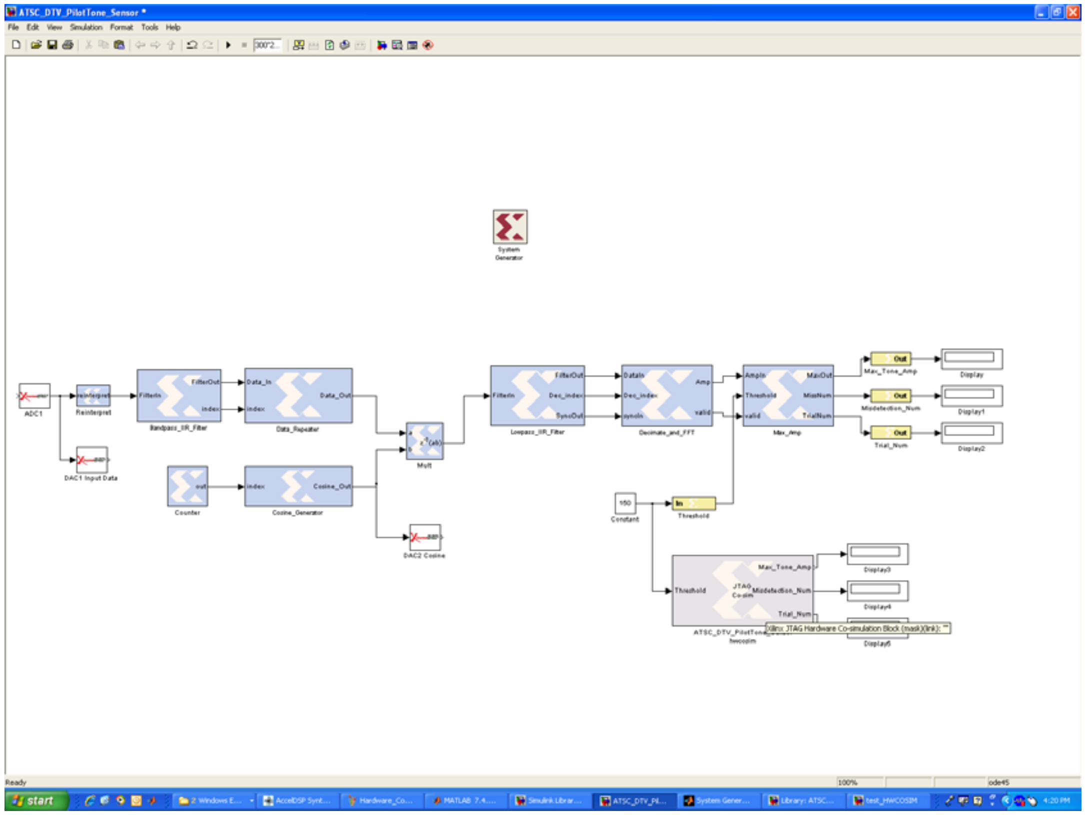

Figure 6.17: Hardware co-simulation structure of the spectrum snesor.

As shown in Fig. 6.17, the generated hardware co-simulation block is configured such that the hardware co-simulation can be executed. The output of this block is the result from the FPGA-based hardware implementation.

6.2 FPGA Implementation Results

The cyclostationarity-based spectrum sensing algorithm for ATSC DTV signals was selected for implementation in a FPGA-based hardware platform. The details of this algorithm were described in Section 2.2 of Chapter 2. The overall system block diagram is shown in Fig. 6.14. However, due to hardware resource limitations of the FPGA board, the algorithm based on a 2048-point FFT operation could not be implemented. In this spectrum sensor, two narrow band IIR filters are needed in the design. The filter coefficients of these two IIR filters need to have word lengths which are larger than 20. Hence, several tens of long-length multipliers are required. As such, these two IIR filters consume sixty percent of the available FPGA resource. On the other hand, in order to calculate the cyclic spectrum, a large amount of data must be buffered and the AccelDSP does not allow for such a large data buffering operation. The Xilinx support team is currently working to fix this software-related problem. As a result, it was decided to reduce the size of the FFT employed in the spectrum sensor to that of 256 points. The same ATSC A/74 DTV real field captured data used in Chapter 2 is taken as the FPGA input data source. These data are used to compare with the software simulation results. As shown in Fig.s' 6.18 to 6.20, the performance of the spectrum sensor is degraded due to the reduction of the FFT size. This is because the cyclostationarity-based spectrum sensor relies on the pilot tones that appear in the cyclic spectrum. Thus, the sensing performance will depend on the spectral resolution. Since an FFT operation with a larger size provides higher spectral resolution, the spectrum sensor with larger FFT size will provide better performance. Furthermore, it can be seen that the hardware implementation results are very close to the software simulation results. Hence, the cyclostationarity-based spectrum sensing algorithm can be conveniently and efficiently implemented in hardware with performance similar to that predicted by the software simulation results.

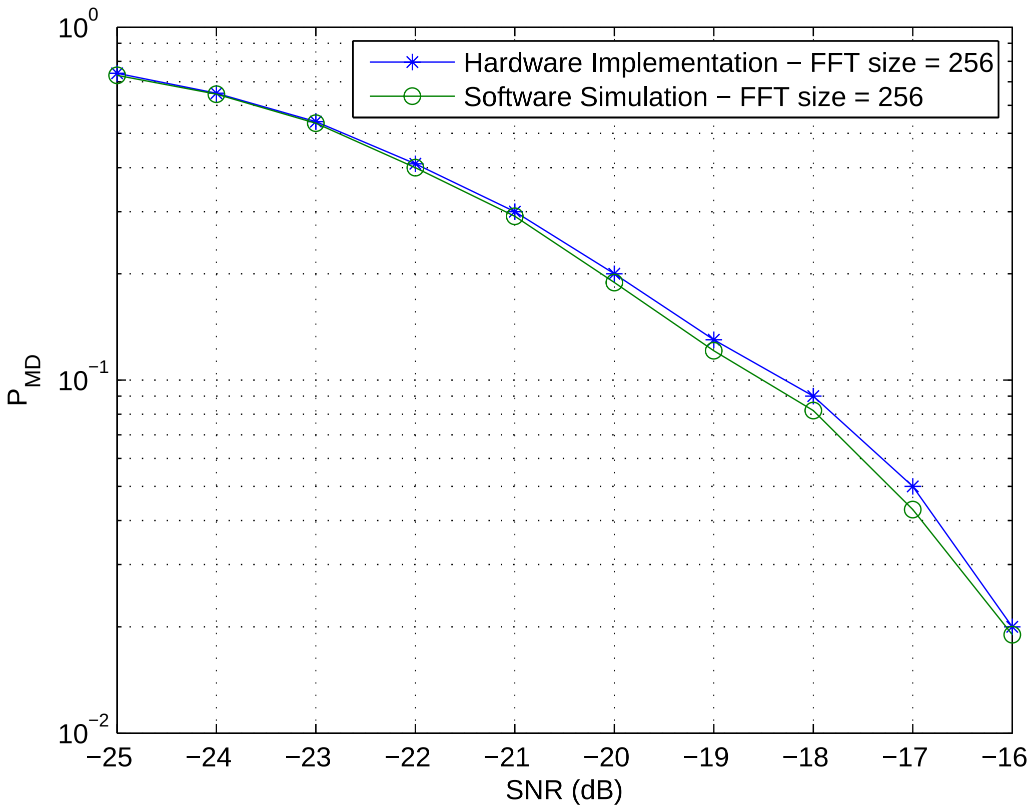

Figure 6.18: Comparison of the hardware implementation and software simulation results for capture data file: WAS_3_27_06022000_REF.

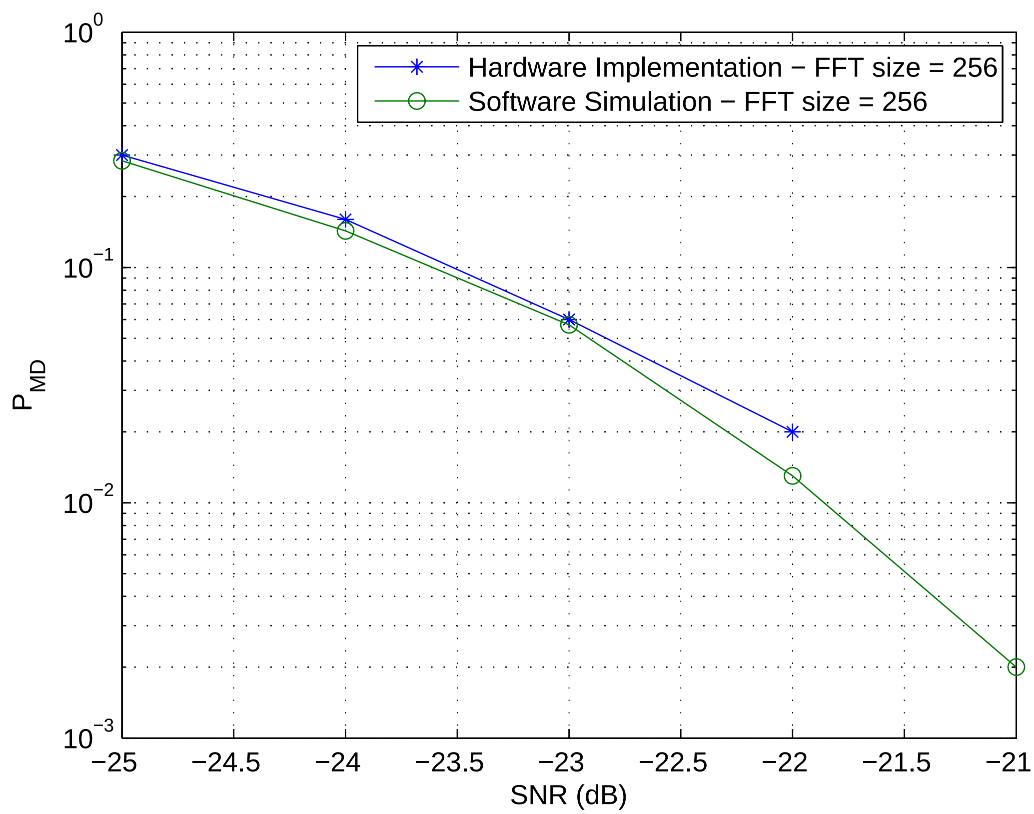

Figure 6.19: Comparison of the hardware implementation and software simulation results for capture data file: WAS_311_36_06052000_REF.

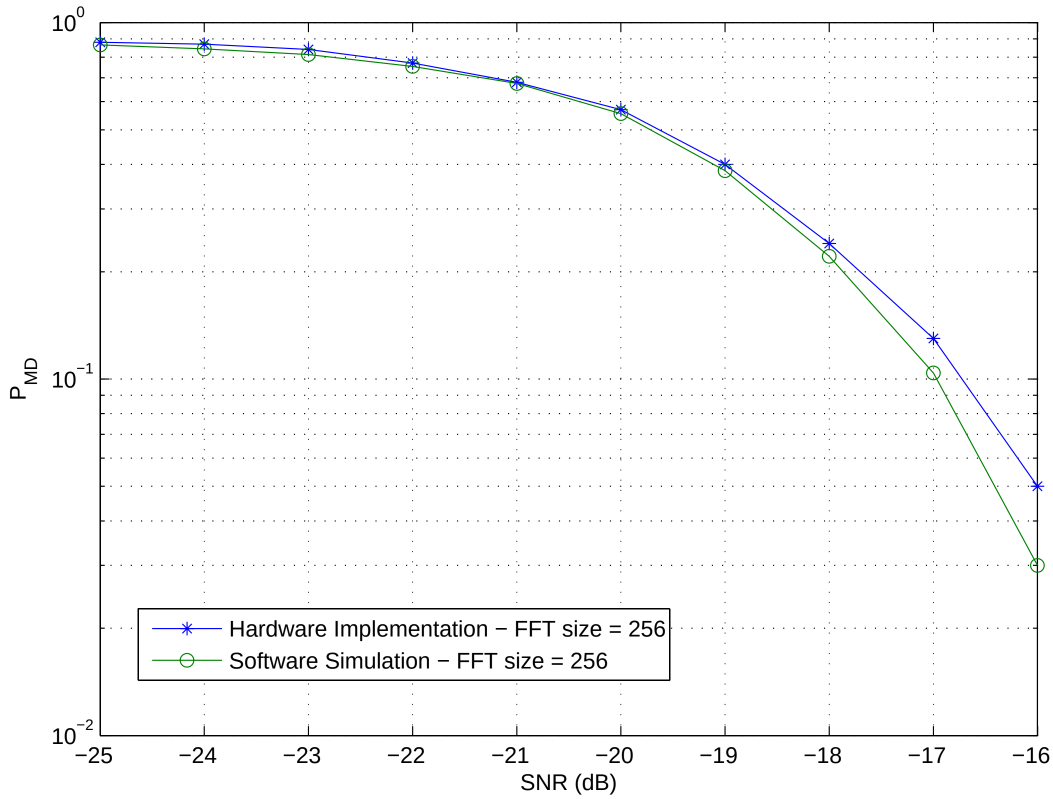

Figure 6.20: Comparison of the hardware implementation and software simulation results for capture data file: WAS_32_48_06012000_OPT.

Chapter 7

Summary and Conclusions

In this thesis, various spectrum sensing algorithms have been developed for different kinds of licensed signals. These signals include three DTV broadcast signals [1] [2] [3], and wireless microphone signals. The spectrum sensing algorithms developed in this thesis are the best known results available to date, and they can efficiently detect the presence of primary licensed signals when the SNR is as low as -20 dB. Theoretical analyses of the probability of false alarm and probability of misdetection for various spectrum sensing algorithms have also been explicitly derived. A hardware implementation of the cyclostationarity-based spectrum sensing algorithm for ATSC DTV signals is described in this thesis. Future extensions of the work reported in this thesis are primarily related to the hardware implementation of spectrum sensing algorithms. In particular, spectrum sensing algorithms for the OFDM and wireless microphone signals are to be implemented in an FPGA-based hardware platform. A real-time spectrum sensor that includes an RF antenna, an analog to digital converter (ADC), and an FPGA board will be built as a prototype for potential use in Cognitive Radio systems.

References

[1] ATSC, "Digital Television Standard, Revision E with Amendments No. 1 and No. 2, ANNEX D," ATSC, September 2006.

[2] ETSI, "Digital Video Broadcasting: Framing Structure, Channel Coding, and Modulation for Digital Terrestrial Television," European Telecommunication Standard EN300744, August 1997.

[3] NSPRC, "Framing Structure, Channel Coding and Modulation for Digital Television Terrestrial Broadcasting System," NSPRC, August 2007.

[4] FCC, *Spectrum Policy Task Force Report*, ET Docket No. 02-155, November 2002.

[5] J. Mitola III, "Cognitive Radio: An Integrated Agent Architecture for Software Defined Radio," Ph.D. Thesis, Royal Institute of Technology, Sweden, May 2000.

[6] S. Shellhammer, "Performance of the Power Detector," *IEEE* 802.22-06/0075r0, May 2006.

[7] S. Shellhammer and R. Tandra, "Performance of the Power Detector with Noise Uncertainty," *IEEE* 802.22-06/0134r0, July 2006.

[8] S. M. Kay, *Fundamentals of Statistical Signal Processing, Detection Theory*, Prentice Hall, Upper Saddle River, NJ, 1993.

[9] Y. Zeng and Y. Liang, "Performance of Eigenvalue Based Sensing Algorithms for Detection of DTV and Wireless Microphone Signals," *IEEE* 802.22-06/186r0, September 2006.

[10] H. Chen, W. Gao, and D. G. Daut, "Signature Based Spectrum Sensing Algorithms for IEEE 802.22 WRAN," *IEEE ICC CogNets Workshop*, Glasgow, Scotland, June 2007.

[11] H. Chen, W. Gao, and D. G. Daut, "Spectrum Sensing Using Cyclostationary Properties and Application to IEEE 802.22 WRAN," *IEEE Globecom* 2007, Washington D.C., December 2007.

[12] S. Shellhammer, V. Tawil, G. Chouinard, M. Muterspaugh, and M. Ghosh, "Spectrum Sensing Simulation Model," *IEEE* 802.22-06/0028r10, September 2006.

[13] V. Tawil, "DTV Signal Captures," *IEEE* 802.22-06/0038r0, March 2006.

[14] V. Tawil, "DTV Signal Captures Database," *IEEE* 802.22-06/0081r0, May 2006.

[15] S. Mathur, R. Tandra, S. Shellhammer, and M. Ghosh, "Initial Signal Processing of Captured DTV Signals for Evaluation of Detection Algorithms,"*IEEE* 802.22-06/0158r4, September 2006.

[16] A. Papoulis, *Probability, Random Variables, and Stochastic Processes*, Third Edition, McGraw Hill, New York, NY, 1991.

[17] W. A. Gardner, "Exploitation of Spectral Redundancy in Cyclostationary Signals," *IEEE Signal Processing Magazine*, Vol. 8, No. 2, pp. 14-36, April 1991.

[18] W. A. Gardner, "Measurement of Spectral Correlation," *IEEE Transactions on Acoustics, Speech, and Signal Processing*, Vol. ASSP-34, No. 5, pp. 1111-1123, October 1986.

[19] W. A. Gardner, *Statistical Spectral Analysis: A Nonprobabilistic Theory*, Englewood Cliffs, NJ: Prentice-Hall, 1987.

[20] S. Shellhammer, "An ATSC Detector Using Peak Combining," *IEEE* 802.22-06/243r5, March 2007.

[21] L. Lv, S. Chang, and Z. Wu, "Sensing Schemes for DVB-T," *IEEE* 802.22-06/0127r2, July 2006.

[22] T. Pollet, P. Spruyt, and M. Moeneclaey, "The BER Performance of OFDM Systems Using Non-Synchronized Sampling," *Proc. IEEE Globecom*, pp. 253-257, San Francisco, CA, 1994.

[23] H. Bölcskei, "Blind Estimation of Symbol Timing and Carrier Frequency Offset in Wireless OFDM Systems," *IEEE Trans. Commun.*, Vol. 49, No. 6, pp. 988-999, June 2001.

[24] M. Ghosh, V. Gaddam, and G. Turkenich, "DTV Signal Sensing Using Pilot Detection," *IEEE* 802.22-07/xxxx-00-0000, March 2007.

[25] ETSI, "Digital Video Broadcasting (DVB); Transmission System for Handheld Terminals (DVB-H)," European Telecommunication Standard EN302304 1.1.1, November 2004.

[26] IEEE Standard, "IEEE Standard for Information Technology-Telecommunications and Information Exchange Between Systems-Local and Metropolitan Area Networks-Specific Requirements - Part 11: Wireless LAN Medium Access Control (MAC) and Physical Layer (PHY) Specifications," IEEE, New York, NY, June 2007.

[27] H. Chen, W. Gao, and D. G. Daut, "Spectrum Sensing for OFDM Systems Employing Pilot Tones and Application to DVB-T OFDM," *Proc. IEEE ICC* 2008, Beijing, China, June 2008.

[28] H. Chen, W. Gao, and D. G. Daut, "Spectrum Sensing and Transmission Mode Detection Algorithms for DVB-T OFDM," *ACM CWNets 2007*, Vancouver, Canada, August 2007.

[29] T. M. Cover and J. A. Thomas, *Elements of Information Theory*, Wiley Series in Telecommunications, John Wiley & Sons, Inc., New York, NY, 1991.

[30] D. G. Brennan, "Linear Diversity Combining Techniques," *Proceedings of the IEEE*, Vol. 91, No. 2, pp. 331-356, February 2003.

[31] C. Sheu and C. Huang, "A Novel Guard Interval Based ISI-Free Sampling Region Detection Method for OFDM Systems," *Proc. IEEE VTC*, Vol. 1, pp. 515-519, September 2004.

[32] Y. Chen and C. Tellambura, "Infinite Series Representations of the Trivariate and Quadrivariate Rayleigh Distribution and Their Applications," *IEEE Trans. on Comm.*, Vol. 53, No. 12, pp. 2092 - 2101, December 2005.

[33] P. Dent, E. G.. Bottomley, and T. Croft, "Jakes Fading Model Revisited," *Electronics Letters*, Vol. 29, No. 13, pp. 1162-1163, June 1993.

[34] H. Chen, W. Gao, and D. G. Daut, "Spectrum Sensing for DMB-T Systems Using PN Frame Headers," *Proc. IEEE ICC* 2008, Beijing, China, June 2008.

[35] H. Chen, W. Gao, and D. G. Daut, "Spectrum Sensing for Wireless Microphone Signals," submitted to *IEEE Workshop on Networking Technologies for Software Defined Radio (SDR) Networks*, San Francisco, CA, June 2008.

[36] E. Reihl, "Wireless Microphone Characteristics," *IEEE* 802.22-06/0070r0, May 2006.

[37] S. Haykin, *Communication Systems*, Fourth Edition, John Wiley & Sons, Inc., New York, NY, 2001.

[38] C. Clanton, M. Kenkel and Y. Tang, "Wireless Microphone Signal Simulation Method," *IEEE* 802.22-07/0124r0, March 2007.

[39] J. Unnikrishnan and S. Shellhammer, "Simulation of Eigenvalue Based Sensing of Wireless Microphone," *IEEE* 802.22-07/0357r0, July 2007.

[40] ETSI, "Electromagnetic Compatibility and Radio Spectrum Matters (ERM); Wireless Microphones in the 25 MHz to 3 GHz Frequency Range; Part 1: Technical Characteristics and Methods of Measurement," European Telecommunication Standard, Draft EN 300 422-1 V1.3.1, April 2007.

[41] T. S. Rappaport, *Wireless Communications, Principles and Practice*, Second Edition, Prentice Hall, Upper Saddle River, NJ, 2002.

[42] P. Stoica and R. Moses, *Spectral Analysis of Signals*, Prentice Hall, Upper Saddle River, NJ, 2005.

[43] Xilinx Inc., "AccelDSP Synthesis Tool, User Guide," Release 9.2.00, August 2007.

Curriculum Vita

HOU-SHIN CHEN

Education

09/04 – 05/08	**Rutgers, The State University Of New Jersey, New Jersey, USA** Department of Electrical and Computer Engineering Advisor: Dr. David G. Daut	Ph.D. GPA: 3.94/4.00
09/02 – 06/04	**National Taiwan University, Taipei, Taiwan** Graduate Institute of Communication Engineering Advisor: Dr. Yumin Lee	MS GPA: 4.00/4.00
09/98 – 06/02	**National Taiwan University, Taipei, Taiwan** Department of Electrical Engineering	BS GPA: 3.71/4.00

Expertise

Spectrum Sensing for DTV Broadcast Systems: Spectrum sensing for digital television broadcast systems include ATSC DTV Standard, ETSI DVB-T Standard and NSPRC DMB-T Standard.
Receiver Design for Multi-User OFDM systems: Timing synchronization, frequency offset estimation, sampling clock offset estimation and channel estimation for multi-user OFDM systems.
Receiver Design for GPRS Systems: Design and analysis for receiver with space-time diversity for GPRS system.

Honors and Awards

2005 Graduate Fellowship, ECE Department, Rutgers University
2002 National Taiwan University Science and Technology Thesis Competition Award
2002 Chinese Engineering Association Student Thesis Competition Award
2001 National Science Council Undergraduate Student Specific Project Scholarship

Experiences

03/03/2008 ~ 02/28/2010 R&D Engineer – Thomson

Development and proposal for next generation digital TV broadcast in cable.

09/25/2006 ~ 01/16/2008 Intern – Thomson

Develop various spectrum sensing algorithms for different signals including ATSC DTV, DVB-T, DMB-T and wireless microphone signals. Implement various spectrum sensing algorithms by FPGA and perform real world test.

Patents (being filed with the US Patent and Trademark Office)

- 60995782: Time and frequency synchronization and frame number detection for DMB-T systems.
- 60995781: Spectrum sensing for DMB-T systems using PN frame headers.
- 60959372: Spectrum sensing for OFDM signals by utilizing pilot tones.
- 60934715: Detection of signals containing sine-wave components through measurement of power spectral density (PSD) and cyclic spectrum.
- 60927815: Spectrum sensing and transmission mode detection algorithms for DVB-T OFDM.
- 60919807: Spectrum sensing using cyclostationary properties and application for IEEE 802.22 WRAN.

- 60905691: Apparatus and method for sensing a signal using cyclostationarity.
- 60899055: Apparatus and method for sensing an ATSC signal in low signal-to-noise ratio.
- 60880081: Apparatus and method for sensing an ATSC signal in low signal-to-noise ratio.
- 10436138: Method of processing an OFDM signal and OFDM receiver using the same method.

Publications

- Hou-Shin Chen, Wen Gao, and David G. Daut, "Spectrum Sensing for OFDM Systems Employing Pilot Tones," submitted to *IEEE Trans*. *on Wireless Communications.*
- Hou-Shin Chen, Wen Gao, and David G. Daut, "Spectrum Sensing for Wireless Microphone Signals," submitted to *IEEE SECON* 2008.
- Hou-Shin Chen, Wen Gao, and David G. Daut, "Spectrum Sensing for OFDM Systems Employing Pilot Tones and Application to DVB-T OFDM," *IEEE ICC 2008*, June 2008.
- Hou-Shin Chen, Wen Gao, and David G. Daut, "Spectrum Sensing for DMB-T Systems Using PN Frame Headers," *IEEE ICC 2008*, June 2008.
- Hou-Shin Chen, Wen Gao, and David G. Daut, "Spectrum Sensing Using Cyclostationary Properties and Application to IEEE 802.22 WRAN," *IEEE Globecom* 2007, December 2007.
- Hou-Shin Chen, Wen Gao, and David G. Daut, "Spectrum Sensing and Transmission Mode Detection Algorithms for DVB-T OFDM," *ACM CWNets 2007*, August 2007.
- Hou-Shin Chen, Wen Gao, and David G. Daut, "Signature Based Spectrum Sensing Algorithms for IEEE 802.22 WRAN," *IEEE ICC CogNets Workshop*, June 2007.
- Hou-Shin Chen, Yumin Lee and David G. Daut, "Robust Timing Synchronization for Uplink Multi-Carrier Spread-Spectrum Systems, " *IEEE Globecom*, 2005.
- Hou-Shin Chen, Yumin Lee and David G. Daut, " “Robust Multi-User Frequency Offset Estimation for Uplink Systems Using OFDM Technique," *IEEE VTC*, Fall 2005.
- Shiou-Hong Chen, Way-Hong He, Hou-Shin Chen and Yumin Lee, "Mode Detection, Synchronization, and Channel Estimation for DVB-T OFDM," *IEEE Globecom*, 2003.
- Hou-Shin Chen and Yumin Lee, "Novel Sampling Clock Offset Estimation for DVB-T OFDM," *IEEE VTC*, Fall 2003.